# School of Science Department of Physics and Astronomy Master Degree Programme in Astrophysics and Cosmology

# JWST observations of the stellar system Terzan 5 in the Galactic Bulge

#### **Graduation Thesis**

Presented by:

**Supervisor:** 

Giorgia Zullo

Chiar.mo Prof.

Francesco R. Ferraro

Co-Supervisors:

Prof.ssa Cristina Pallanca Prof.ssa Barbara Lanzoni

Academic year 2024/2025 Graduation date 26/09/2025

Puro e disposto a salire a le stelle.Dante Alighieri, Purgatorio XXXIII, 145

Considerate la vostra semenza: fatti non foste a viver come bruti, ma per seguir virtute e canoscenza.

Dante Alighieri, Inferno XXVI, 119–120

# Contents

1	Intr	oducti	ion	1			
	1.1	The M	filky Way Bulge: a laboratory for galaxy formation	1			
	1.2	Globu	lar Clusters	2			
	1.3	The C	Color-Magnitude Diagram	4			
	1.4	The d	iscovery of Bulge Fossil Fragments	10			
		1.4.1	Terzan 5	10			
		1.4.2	Liller 1	15			
2	The	e dataset 18					
	2.1	The Ja	ames Webb Space Telescope	18			
		2.1.1	JWST insights into Terzan 5	18			
		2.1.2	The instrument	19			
	2.2	NIRC	am	21			
		2.2.1	NIRCam Readout Patterns	22			
		2.2.2	Frame 0	25			
		2.2.3	The dataset	26			
		2.2.4	Stage 1 Pipeline	26			
		2.2.5	Stage 2 Pipeline	32			
		2.2.6	Calibrated data products	33			
		Comp	leting the dataset: HST observations	34			
		2.3.1	The Hubble Space Telescope	34			
		2.3.2	The HST dataset	36			
		2.3.3	The final dataset	38			
3	Pho	$\mathbf{tomet}$	ric reduction	39			
3.1 Photometric techniques: PSF fitting		metric techniques: PSF fitting	39				
	3.2	Daoph	not II photometric reduction	41			
		3.2.1	JWST dataset	41			
		3.2.2	HST dataset	45			
		3.2.3	Combined catalogue	45			

6	Cor	nclusions	82
	5.2	Age determination with the MS-TO	74
	5.1	Distance modulus and color excess	
5	Res	sults	71
	4.3	Final corrected CMD	69
		4.2.2 Differential reddening correction	64
		4.2.1 Extinction and reddening	61
	4.2	Differential reddening	61
	4.1	Proper motions	
4	Pro	per motions and differential reddening	55
	3.4	Astrometry	53
		3.3.1 Calibration	53
	3.3	jwst1pass photometric reduction	51
		3.2.4 Calibration	47

# Abstract

Among the stellar systems in the Milky Way, Terzan 5 stands out as one of the most intriguing. Hidden in one of the most heavily obscured regions of the bulge, it holds traces of the Galaxy's earliest formation history. Despite its morphological appearance, it is far from a conventional globular cluster: extensive studies have revealed over the years the coexistence of stellar populations with strikingly different ages and chemical compositions (Ferraro et al., 2009; Ferraro et al., 2016; Origlia et al., 2025). These findings demonstrate that its true nature is that of a "Bulge Fossil Fragment" (Ferraro et al., 2021): the surviving relic of a primordial building block of the bulge. This interpretation naturally connects Terzan 5 to high redshift stellar clumps observed in star forming galaxies (Elmegreen et al., 2009) and fits within the broader cosmological framework of hierarchical galactic assembly. In this context, Terzan 5 could be the fossil remnant of an early massive clump formed through disk instabilities during the initial phases of the Milky Way evolution (Immeli et al., 2004).

In this thesis I exploit the unprecedented resolution and near-infrared photometric capabilities of the JWST NIRCam instrument, together with archival HST optical observations, to further investigate the nature of Terzan 5's stellar populations. This combination allows us to overcome the problems caused by severe extinction along the line of sight and to obtain the deepest and most accurate color-magnitude diagram to date. Proper motion selections and differential reddening corrections were applied to isolate members and reveal the intrinsic features of the evolutionary sequences. In particular, thanks to significantly increased samples of stars in a much larger field of view with respect to previous works, this study has revealed with an unprecedented level of accuracy the complex structure of the main-sequence turnoff, which is the most reliable stellar clock. The comparison with isochrones, revealed an old metal-poor component with an age of  $12.7 \pm 0.5$  Gyr, and a younger metal-rich component of  $4.6 \pm 0.5$  Gyr. In addition, this work has provided the first photometric evidence of the existence of an even younger population, which could extend the period of recent star formation activity down to less than  $\sim 3.8$  Gyr ago. Combined with previous findings on the system, the results of this thesis work confirm the composite nature of Terzan 5 and support its identification as a Bulge Fossil Fragment. As a natural consequence, these results also reinforce the picture of bulge assembly by mergers of massive clumps in the early Universe.

This thesis is organized as follows.

**Chapter 1** introduces the astrophysical context for the Galactic bulge with focus on the peculiar case of Terzan 5 and its connection to galaxy formation models.

Chapter 2 describes the JWST and HST instrumental setups and datasets, along with the pre-reduction steps for the JWST images.

**Chapter 3** presents the photometric analysis for both datasets.

Chapter 4 describes the derivation of relative proper motions and differential reddening corrections and maps.

Chapter 5 is devoted to the isochrone fitting procedures, with the main goal of determining the ages of the detected sub-populations of Terzan 5.

Chapter 6 summarizes the main results of this study, and provides a few future perspectives of the work.

# Chapter 1

# Introduction

# 1.1 The Milky Way Bulge: a laboratory for galaxy formation

The Milky Way is a barred spiral galaxy whose complex structure and proximity offer a unique opportunity to study the processes of galaxy formation and evolution. Its main stellar content is typically described as being composed by a thin and thick disk, a central bulge and bar structure, and an extended halo. Among these, the bulge stands out as a particularly dense region of high surface brightness, likely preserving crucial evidence of the earliest phases of the Galaxy's physical history.

The bulge contributes to roughly one quarter of the total stellar mass, corresponding to  $\simeq 2.0 \times 10^{10} \, M_{\odot}$  (Valenti et al., 2016) and extends out to a radius of approximately 2 kpc from the Galactic center. It is generally described as being dominated by an old stellar population ( $\geq 10$  Gyr) with near–solar metallicity, although growing evidence points to the presence of a younger component (Clarkson et al., 2008; Clarkson et al., 2011; Bernard et al., 2018). In the broader context of galaxy formation and evolution, bulges play a central role, as their kinematics, structure, and stellar populations harbor signatures of the physical processes that shaped them. Despite their importance, their origin is still actively debated. Theoretical models for bulge formation typically fall into three broad categories: (i) monolithic, dissipative collapse during the early stages of galaxy formation (Eggen et al., 1962); (ii) secular evolution of the disk driven by the dynamical influence of a central bar (Kormendy and Kennicutt, 2004); and (iii) mergers or accretion of smaller systems, including primordial galaxies and massive clumps arising from early disk instabilities (Immeli et al., 2004).

Given these open questions, identifying observational constraints that can distinguish between these scenarios is of fundamental importance. The proximity of the Milky Way bulge makes it an ideal laboratory for such investigations, as it enables

deeper, higher resolution observations than those possible for any other galaxy. In particular, objects like bulge globular clusters, whose ages are comparable to those of the earliest Galactic structures, serve as exceptionally valuable probes of the primordial phases of bulge assembly.

Historically, studies of the bulge have been complicated by the severe and spatially variable extinction caused by interstellar gas and dust along the line of sight. However, the advent of modern observational facilities, most notably the James Webb Space Telescope, now allows us to overcome many of these limitations, enabling unprecedentedly detailed studies of resolved stellar populations even in the most crowded and obscured regions of the Galactic bulge.

#### 1.2 Globular Clusters

Stellar astrophysics has laid the groundwork for many fields in modern astronomy, providing fundamental benchmarks for the study of a wide range of systems. Among resolved stellar populations, meaning those in which individual stars can be observationally distinguished, Globular Clusters (GCs) are of particular interest.

Traditionally, GCs were viewed as single-age, single-metallicity systems formed in one burst of star formation (SF) from a common molecular cloud. However, this classic paradigm has been revised in light of growing observational evidence: nearly all GCs exhibit signatures of Multiple Stellar Populations, showing variations in light elements such as C, N, O, Na, Al, He, and Mg, while preserving uniformity in iron content [Fe/H] (see review by Gratton et al., 2004). Among these abundance patterns, the most well known and ubiquitous is the O-Na anticorrelation. Such chemical signatures are believed to originate from successive star formation episodes within a few  $10^8$ years after the cluster's formation. They are the result of high-temperature protoncapture nucleosynthesis occurring in the short-lived, massive first generation stars. In particular, the O-Na and Mg-Al anticorrelations are explained by the operation of the Ne–Na and Mg–Al thermonuclear cycles, which are activated under temperature conditions exceeding  $\sim 50-70$  MK. The processed material, released through stellar winds or mass loss, likely polluted the intracluster medium from which the second generation of stars subsequently formed. Since iron-peak elements are instead produced by Supernovae, which release high-velocity ejecta that easily exceed the escape velocity of a cluster, GCs do not exhibit significant [Fe/H] spreads and the notion that they are homogeneous in iron remains valid today.

Despite this added complexity, GCs still represent the closest natural approximation to a Simple Stellar Population (SSP), a theoretical construct of stars formed simultaneously, from the same cloud, and with identical chemical composition. SSPs have



Figure 1.1: The globular cluster NGC362 as captured by the Hubble Space Telescope, displaying the characteristic visual appearance of such systems. Image credit: NASA/ESA (2016)

been the basis of much of stellar evolution theory and serve as fundamental building blocks for models of galaxies and composite stellar populations. Typical GCs contain between  $10^4$  and  $10^6$  stars and are quite compact systems, with effective radii of the order of 1–10 pc, yielding exceptionally high central stellar densities. This makes them ideal natural laboratories for studying multi-body dynamics in dense, collisional stellar environments.

The Milky Way hosts approximately 150–170 known GCs. One of their most compelling attributes is their age: as some of the oldest structures in the Universe, with formation epochs estimated between 10 and 13 Gyr, they provide valuable insights into the early history of the Milky Way. Within it, GCs reside primarily in the halo and bulge, and have historically been associated with Population II: old and metal-poor stars. Bulge GCs typically have [Fe/H] values ranging from  $\approx -1.5$  to  $\approx 0$ . Their large stellar populations, combined with their relative proximity, enable studies with exceptionally high statistical significance. The high stellar densities in GCs also promote frequent dynamical interactions, leading to the formation of exotic objects and phenomena such as Blue Straggler Stars (BSS), Cataclysmic Variables and Millisecond Pulsars (MSPs).

## 1.3 The Color-Magnitude Diagram

In the study of resolved stellar populations, one of the most powerful observational tools is the Color–Magnitude Diagram (CMD). For a given set of magnitudes measured in two distinct photometric bands, the CMD displays the magnitude in one band as a function of the color index, defined as the difference between the two magnitudes. The color index is directly related to the star's effective temperature through its spectral energy distribution: hotter stars emit more strongly at shorter wavelengths, yielding bluer colors, while cooler stars emit relatively more at longer wavelengths, appearing redder. The CMD thus provides the observational analogue of the theoretical Hertzsprung–Russell (HR) diagram, which plots stellar luminosity against temperature.

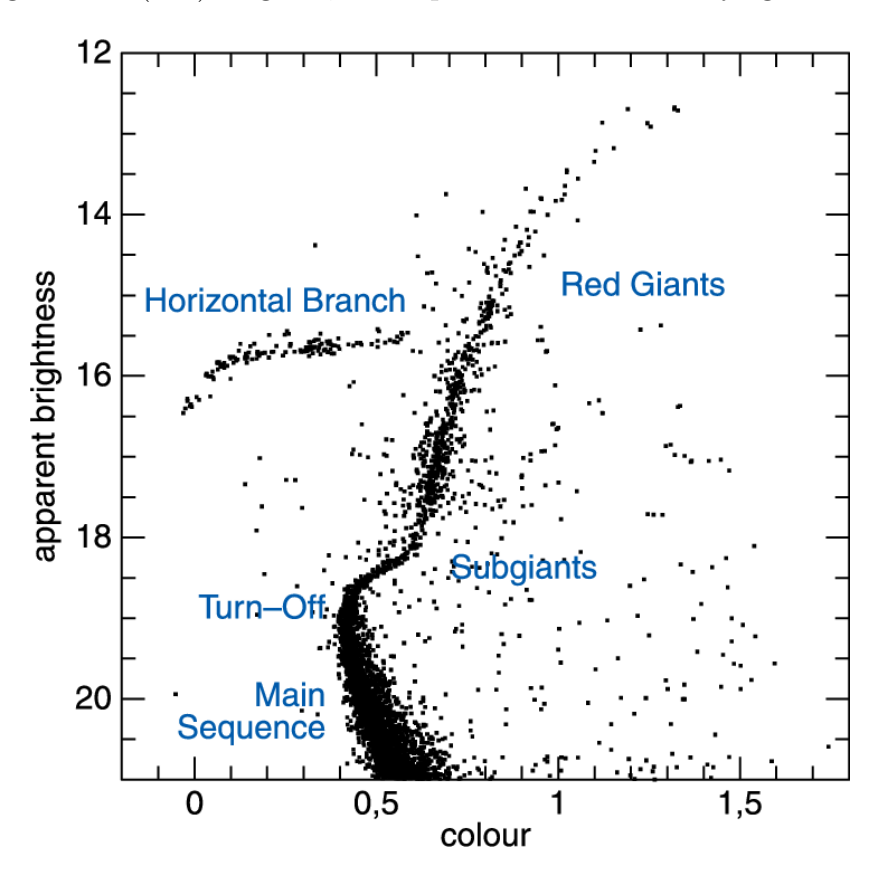


Figure 1.2: Example of a typical CMD of a Globular Cluster, with the main evolutionary sequences labeled.

The great value of the CMD lies in the fact that the fundamental stellar properties, such as mass, radius, effective temperature and luminosity, are all physically interconnected. This interdependence enables us to construct evolutionary models and to predict stellar behaviour within this plane. Indeed, at any given epoch, a star occupies a specific position in the CMD determined by its magnitude and color, both measurable from photometry in two filters. As a star evolves, changes in its internal structure, driven mainly by nuclear burning in the core, cause it to continuously change position

in the diagram. For a star of fixed mass and chemical composition, this path is called its evolutionary track.

In the case of an SSP, the distribution of stars across the CMD is determined by the Initial Mass Function (IMF), which describes the relative number of stars born at different masses. Stellar models and observations have established an approximate relation between stellar mass and luminosity during the phase of core hydrogen burning, expressed as  $L \sim M^{\alpha}$  ( $\alpha \sim 3-4$ ) for low- and intermediate-mass stars. This stage, known as the Main Sequence (MS), is the longest lasting phase in a star's life and appears as a characteristic diagonal sequence in the CMD.

The theoretical model that describes the location of stars in the CMD at a fixed time, meaning stars of the same age but different masses, is called an isochrone. Besides stellar mass and age, the chemical composition (metallicity) also plays a key role in determining the position of an isochrone in the CMD: higher metallicity increases atmospheric opacity making stars appear redder and fainter at a given mass compared to their metal poor counterparts of the same age.

As stars evolve beyond the MS, entering the so called Post–Main-Sequence evolution, they undergo phases of expansion and contraction, accompanied by changes in temperature and the ignition of progressively heavier elements. Given the mass–luminosity relation, more massive stars are more luminous and consume their nuclear fuel more rapidly. This results in a significantly shorter MS lifetime for high-mass stars, a key fact exploited when determining the age of stellar populations.

The main-sequence turn-off (MS-TO) is a fundamental feature in the CMD of a stellar population, marking, from a theoretical point of view, the stage at which stars exhaust the hydrogen in their cores and begin to leave the main sequence. Observationally, this point typically corresponds to the bluest location in the CMD, or the hottest point along the isochrone. Although the stellar mass at the TO is the most accurate age indicator, it cannot be measured directly; therefore, the luminosity at the TO is commonly used as an observable proxy for estimating the age of the population.

Furthermore, the shape of the TO region in the CMD carries valuable information about the internal stellar physics, particularly the dominant hydrogen-burning process. Stars undergoing the CNO cycle  $(M_{MS} > 1.2 M_{\odot})$  often display a characteristic hook-like morphology at the TO, due to a brief phase of core contraction that precedes the onset of hydrogen shell burning. In contrast, stars that rely primarily on the pp-chain  $(M_{MS} < 1.2 M_{\odot})$  tend to exhibit a rounder and smoother TO shape (see Fig. 1.3).

The MS-TO is considered the best age diagnostic given that its morphology and location in the CMD depends almost exclusively on the population's age, with only a minor dependence on metallicity, making it the best "stellar clock" available to date systems. Other features corresponding to following evolutionary phases are strongly influenced by additional factors like helium content, mass loss, convection efficiency

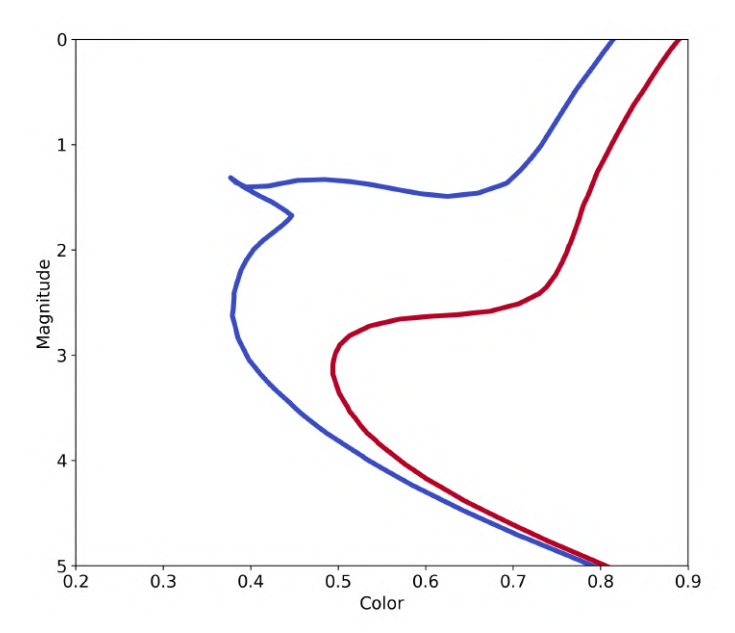


Figure 1.3: Examples of isochrone models highlighting different MS-TO morphologies: rounder (red) and hook-like (blue), as expected for stars dominated by pp-chain and CNO-cycle burning, respectively (Bressan et al., 2012).

and the value of the mixing length parameter, which introduce larger systematic uncertainties (Salaris and Cassisi, 2005).

In the context of this work, the MS-TO is of particular importance: given its high sensitivity to stellar age, its careful analysis in the CMD of Terzan 5 provides one of the most robust constraints on the formation epochs of its distinct stellar populations.

Beyond the MS-TO, several distinct evolutionary phases become apparent in the CMD:

- Subgiant Branch (SGB): It is the phase following the turn-off, when stars have just exhausted their core hydrogen. The main energetic process is hydrogen burning in a thick shell. During this phase, the stellar envelope expands and cools, causing a nearly horizontal feature on the CMD. For younger stellar populations, where the stars undergoing this process are quite massive, this phase is very short-lived and almost no stars appear in that region of the CMD. In this case, the sequence is known as the Hertzsprung Gap.
- Red Giant Branch (RGB): As stars move closer to their Hayashi track, the locus of fully convective stellar models that marks the limit of stable hydrostatic equilibrium, they enter the RGB. In this phase, luminosity rises steeply, producing the nearly vertical "giant" (due to increase of radius) sequence at red colors, roughly parallel to the Hayashi track. The RGB's precise slope and width depend on metallicity and on mixing processes in the envelope. The RGB is typically

well-developed in older stellar populations. For stars with  $M < 2.2 M_{\odot}$ , the RGB is characterized by an endpoint, called the RGB tip, of nearly fixed luminosity. This corresponds to the event of violent helium ignition in the degenerate core (the Helium Flash) and can be used as a standard candle.

Observationally, a fundamental feature of the RGB is the RGB "bump". Physically, it occurs when the outward moving hydrogen-burning shell encounters the chemical discontinuity left behind by the deepest penetration of the convective envelope. As the shell crosses this discontinuity, the energy output temporarily decreases, causing a brief reduction in luminosity. Consequently, the star's evolutionary track crosses the same region of the CMD three times, producing a visible over-density of stars at that magnitude and color.

- Horizontal Branch (HB): Following the helium flash at the tip of the RGB, low-mass stars settle into core helium burning on the Horizontal Branch (or Helium/Red Clump). On the CMD, this appears as a roughly horizontal sequence (depending on the photometric filters) spanning a range of colors at nearly constant luminosity. The color distribution along the HB is governed primarily by the envelope mass, since the core mass is set by the helium flash's physical process. A star with a smaller envelope will thus have bluer colors, while one with a more massive envelope will have a cooler surface and appear redder. At a given epoch, the envelope mass (and consequently the star's HB location) depends on mass loss, initial helium abundance, metallicity, and age. In particular, because the TO mass decreases with increasing age, older populations tend to exhibit bluer horizontal branches.
- Asymptotic Giant Branch (AGB): After core helium exhaustion, stars enter the Asymptotic Giant Branch phase. First, they traverse the Early-AGB phase, during which the helium-burning shell drives convection and expansion of the envelope. Then they enter the Thermal-Pulse AGB phase, characterized by alternating periods of helium and hydrogen shell burning. On the CMD, the AGB runs roughly parallel to and above the RGB.
- Post-AGB and Beyond: The final phases of a star's life are directly linked to its mass. Only stars with initial masses above  $\sim 8\,M_\odot$  can ignite all thermonuclear reactions up to the formation of an iron core, after which fusion is no longer energetically favorable. Lower-mass stars cannot reach those final fusion stages and instead evolve into White Dwarfs (WD), which in sufficiently deep CMDs appear as low-luminosity cooling sequences.

Even though in this work the MS-TO will provide our primary age constraint, isochrone fitting using all sequences can improve reliability of estimates and provide constraints

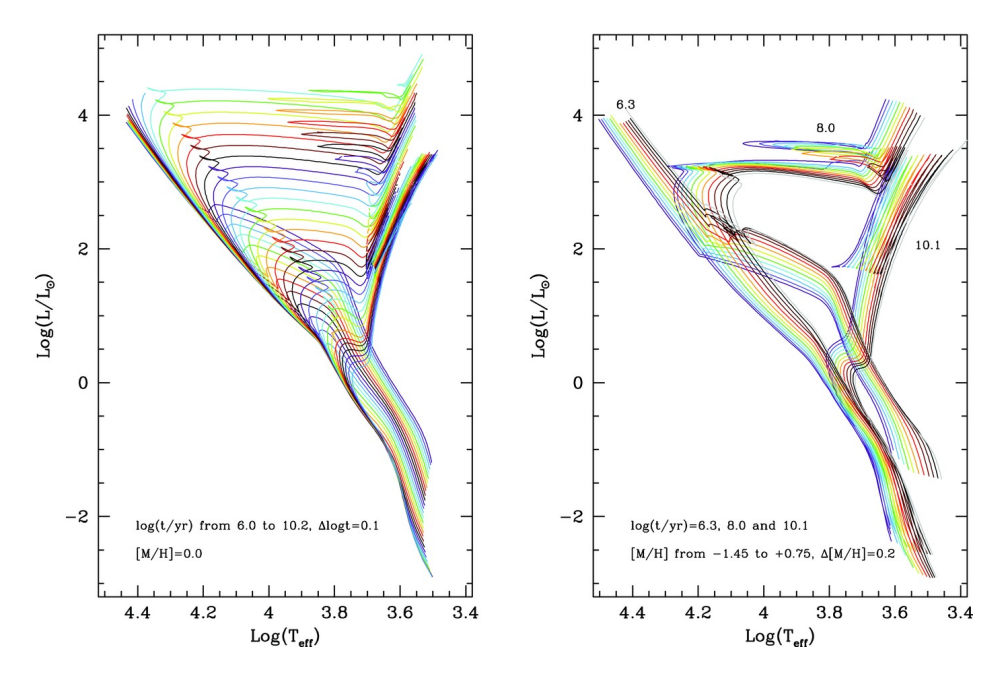


Figure 1.4: Example of model isochrones from PARSEC (PAdova and TRieste Stellar Evolution Code; Bressan et al. 2012).

on parameters like the distance modulus. More in general, using the full extent of the CMD one can attempt to reconstruct the full Star Formation History (SFH) and chemical enrichment of the population.

Indeed, the later stages of stellar evolution significantly impact the chemical enrichment of the surrounding environment, making metal abundance patterns crucial "fingerprints" for identifying the evolutionary history of a stellar population. At the end of their lives, stars enrich the interstellar medium with a variety of elements over very different timescales.

Massive stars  $(M \geq 8\,M_{\odot})$  explode as core-collapse (Type II) Supernovae within tens of millions of years of their formation, releasing  $\alpha$ -elements such as O, Mg, Si, and Ca, as well as some iron-peak nuclei. Intermediate-mass stars  $(1-8M_{\odot})$  evolve through the AGB phase over hundreds of millions to a few billion years. They shed their envelopes through strong stellar winds and planetary nebulae, enriching their surroundings with He, C, N and s-process elements. Lower-mass stars  $(M \leq 8\,M_{\odot})$  ultimately end their lives as WDs, which are compact objects supported against gravitational collapse by the electron-degenerate pressure of their progenitors' cores.

In binary systems, a WD can accrete material from a companion star or merge with another compact object; if this process drives its mass above the Chandrasekhar limit ( $\sim 1.4~M_{\odot}$ ), the maximum mass sustainable by electron degeneracy pressure, a thermonuclear runaway follows, completely disrupting the star and producing a Type Ia supernova. These events, occurring on timescales of roughly 1–10 Gyr after star formation, are the primary source of iron-peak elements.

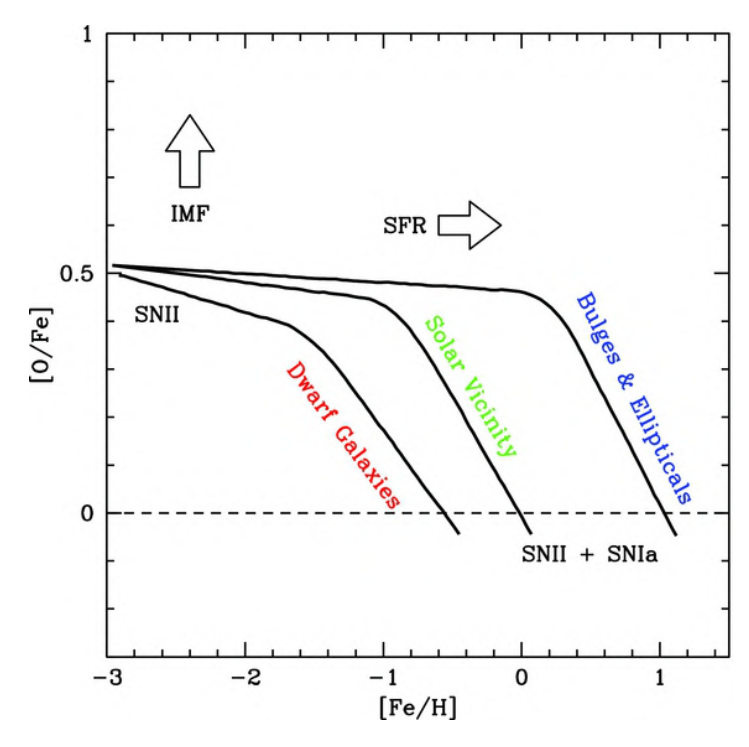


Figure 1.5: Theoretical models of typical  $[\alpha/\text{Fe}]$  trends for different stellar populations, from McWilliam (2016).

This sequence of prompt  $\alpha$ -enhancement from Type II Supernovae, followed by delayed iron enrichment from Type Ia Supernovae, as well as the slow release of AGB products, shapes the characteristic  $[\alpha/\text{Fe}]$  versus [Fe/H] trends observed in stellar populations. Such a plot typically shows an initially constant  $[\alpha/\text{Fe}]$  plateau followed by a sudden drop (the "knee"), which marks the point (or more precisely, the metallicity) when Type Ia Supernovae begin to contribute. This is a crucial tool for inferring the SFH of a stellar system, since a higher Star Formation Rate (SFR) implies that more SNe II will have exploded (and thus more high mass stars were born) by the time SNe Ia begin, causing the knee to appear at a higher metallicity. An example of how different stellar systems with distinct evolutionary histories manifest as different trends in this plot is shown in Fig. 1.5. Studies have shown that the Galactic bulge's knee in this diagram occurs at a higher [Fe/H] than that of the Galactic disk. This is interpreted as evidence of a more rapid and intense star formation history in the bulge.

### 1.4 The discovery of Bulge Fossil Fragments

#### 1.4.1 Terzan 5

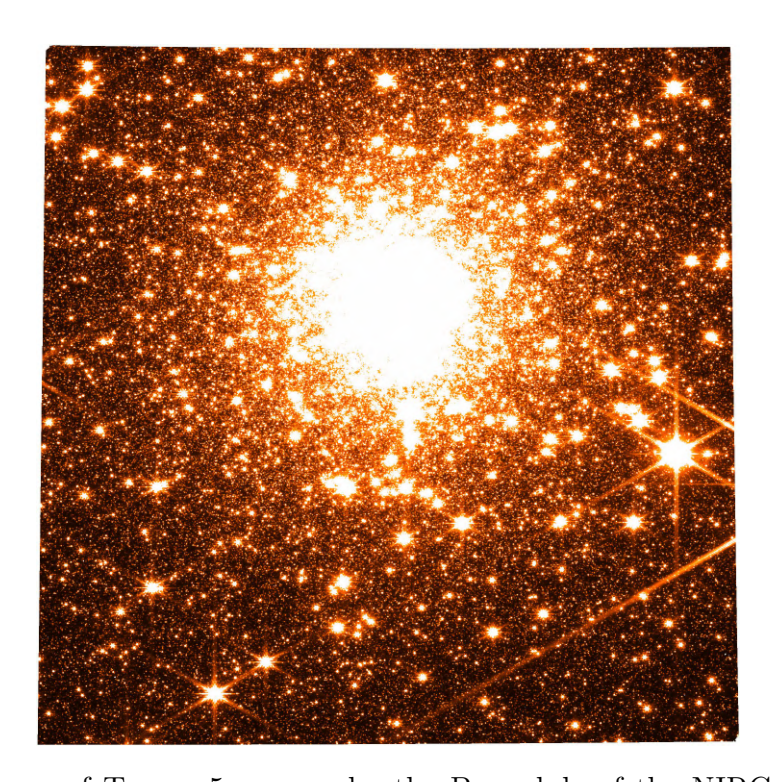


Figure 1.6: Image of Terzan 5 as seen by the B module of the NIRCam instrument onboard the James Webb Space Telescope in the longchannel F277W filter (dataset fully described in Chapter 2)

Terzan 5 is among the most massive stellar systems in the Galaxy ( $M \approx 2 \times 10^6 \, M_{\odot}$ ; Lanzoni et al. 2010) and is located at a distance of  $\sim 2$  kpc from the Galactic center ( $\alpha_{\rm J2000} = 17^{\rm h}48^{\rm m}4.85^{\rm s}$ ,  $\delta_{\rm J2000} = -24^{\circ}46'44.6''$ , Lanzoni et al. 2010). Some of its peculiarities include the highest stellar collision rate and the richest population of Millisecond Pulsars among Galactic GCs (Lanzoni et al., 2010; Ransom et al., 2005; Padmanabh et al., 2024). Historically classified as a bulge GC, it has since revealed a far more complex nature. A major breakthrough came with the discovery of two distinct sub-populations (Ferraro et al., 2009), revealed by the presence of two well-separated horizontal branch clumps (Fig. 1.7). This was made possible by a set of observations with the Multi-Conjugate Adaptive Optics Demonstrator (MAD) at the Very Large Telescope (VLT) of the European Southern Observatory, which enabled significantly improved photometric quality than previously achievable in the J and K bands.

A prompt spectroscopic investigation (Ferraro et al., 2009) revealed that the two distinct sub-populations have comparable radial velocities, thus confirming their membership to the system, but are characterized by different iron abundances. Also based

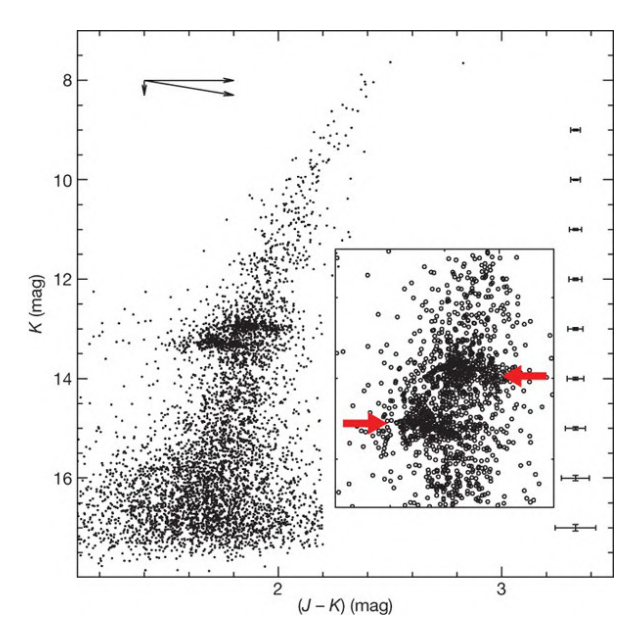


Figure 1.7: (K, J - K) CMD of Terzan 5 obtained with MAD at VLT, showing two distinct Horizontal Branch clumps, hinting at the presence of two distinct populations. From Ferraro et al. (2009)

on subsequent spectroscopic follow-ups, the estimated metallicities are [Fe/H] = -0.25 dex for the dominant metal-poor population, and [Fe/H] = +0.27 dex for the most metal-rich one (Fig. 1.9) as determined by Massari et al. (2014) and Origlia et al. (2011), with hints of a third, more metal-poor component at [Fe/H] = -0.79 (see left panel of Fig. 1.9, Origlia et al., 2013; Massari et al., 2014; Origlia et al., 2025).

By combining Hubble Space Telescope's Advanced Camera for Surveys (HST/ACS) imaging with VLT-MAD observations, Ferraro et al. (2016) provided a first estimate for the ages of the two dominant populations via isochrone fitting of the MS-TO in the (K, I - K) CMD, finding  $\sim$ 12 Gyr for the metal-poor population and 4–5 Gyr for the metal-rich one (Fig. 1.8). Such analyses require sophisticated differential reddening corrections, as Terzan 5 lies in a dense, highly extincted bulge region with  $E(B - V) = 2.38 \pm 0.55$  (Valenti et al., 2010). In this preliminary age estimate, the authors minimized the impact of reddening variations by selecting stars from a homogeneous but limited subregion of the field, thus reducing systematics at the cost of a necessarily small sample.

Further spectroscopic investigations (Origlia et al., 2011, 2013, 2019, 2025) revealed distinct chemical patterns for the two main populations: the metal poor stars are  $\alpha$ -enhanced with  $[\alpha/\text{Fe}] \simeq +0.34$  dex, while metal rich ones are solar-scaled, with  $[\alpha/\text{Fe}] \simeq 0.03$ . The  $\alpha$ -enhancement of the metal-poor component indicates rapid chemical enrichment dominated by SNe II, whereas the nearly solar  $[\alpha/\text{Fe}]$  of the metal-rich population points to longer formation timescales with substantial iron contribution

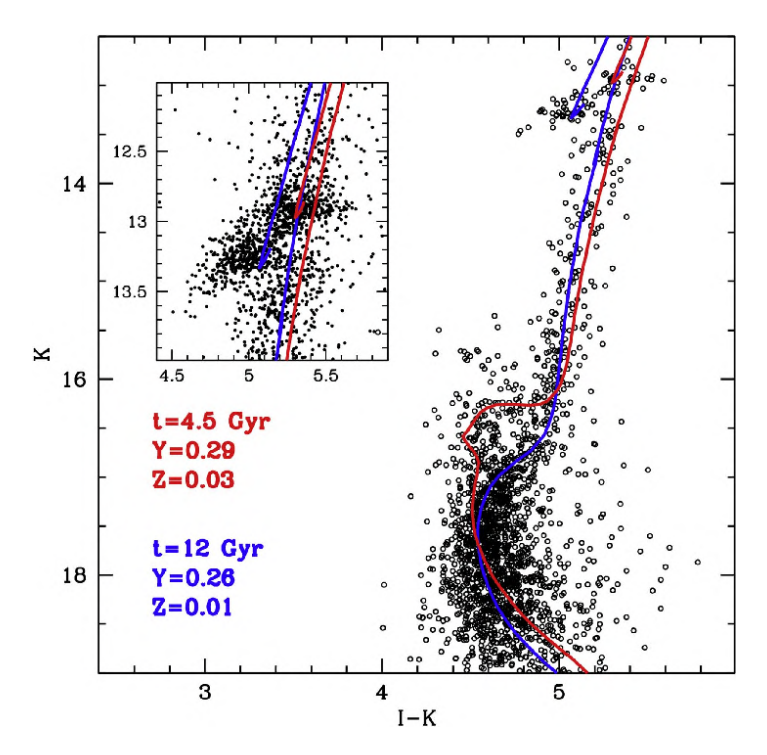


Figure 1.8: (K, I - K) differential reddening corrected CMD of Terzan 5 obtained with VLT-MAD and HST/ACS, for a small (600 arcsec<sup>2</sup>) portion of the FOV. The blue and red line show the best fit isochrones; the corresponding ages and metallicities are labeled. From Ferraro et al. (2016).

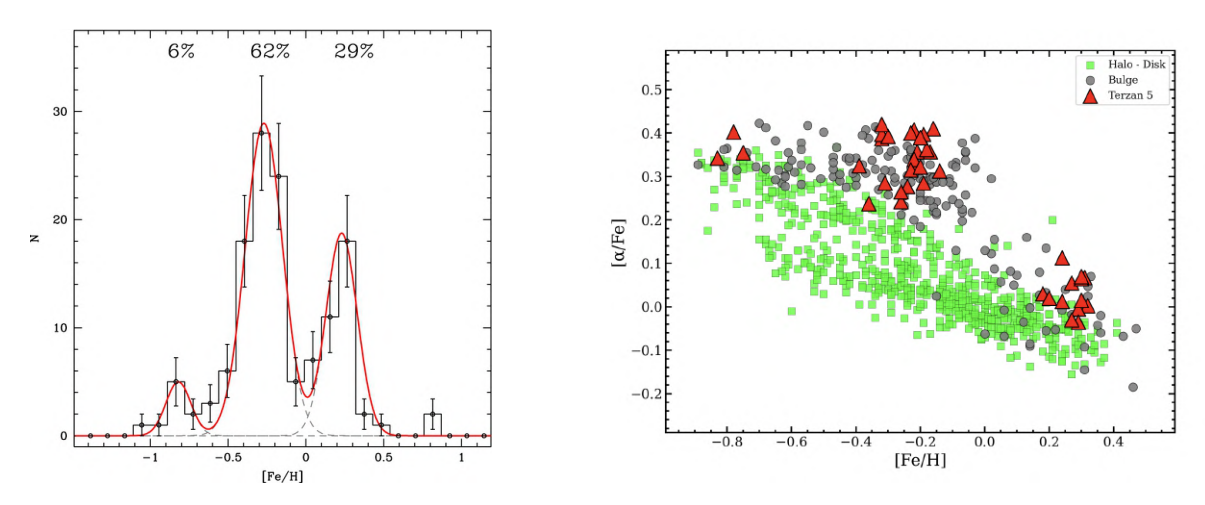


Figure 1.9: The chemical signatures of Terzan 5 confirming the presence of multiple iron sub-populations and a tight link to the Bulge. Left panel: [Fe/H] distribution as derived from Massari et al. (2014) with a FLAMES+DEIMOS and NIRSPEC spectroscopic sample comprising 135 stars. Right panel:  $[\alpha/\text{Fe}]$  vs [Fe/H] distribution of the stars observed in Terzan 5 (red triangles) with respect to that of bulge (grey circles) and halo/disk stars (green squares) from Origlia et al. (2025). This clearly shows the tight chemical link between Terzan 5 and the Bulge.

from SN Ia. The location of the "knee" in the  $[\alpha/\text{Fe}]$ –[Fe/H] plane thus suggests a very high early star-formation efficiency.

Combined with the observed iron spread, these chemical signatures strongly support a scenario of multiple star formation episodes, producing an overall abundance pattern strikingly similar to that of the Galactic bulge (Fig. 1.9).

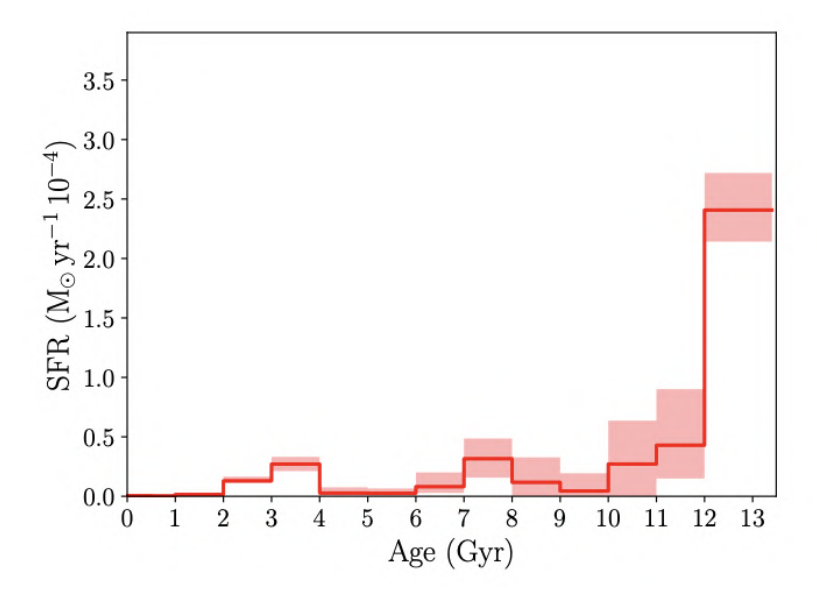


Figure 1.10: Reconstructed star formation history of Terzan 5 from Crociati et al. (2024).

The preliminary reconstruction of the SFH of Terzan 5 (Crociati et al., 2024) indicates a prolonged star formation activity with a dominant peak between 12 and 13 Gyr ago, accounting for roughly 70% of the present-day stellar mass, followed by two additional, lower-intensity episodes at approximately 7 and 4 Gyr ago. Radial distribution investigations have revealed the youngest metal rich populations to be more centrally segregated, as expected in a self-enrichment scenario (Ferraro et al., 2009; Lanzoni et al., 2010; Ferraro et al., 2016).

Overall, the available evidence demonstrates that Terzan 5 is not a genuine globular cluster, raising fundamental questions about its true nature and evolutionary history. The presence of multiple star formation episodes and a significant iron spread might suggest that Terzan 5 is the remnant of an accreted dwarf galaxy. However, this scenario is ruled out by the observed  $[\alpha/\text{Fe}]$ –[Fe/H] relation: the location of the "knee" points to a star formation rate far higher than those observed in dwarf galaxies (Tolstoy et al., 2009). Another possible explanation could be the merger of two globular clusters with different metallicities. This, however, is highly improbable given the extremely low likelihood of such events, the presence of multiple (in place of just two) iron peaks, and the fact that typical GC metallicities are significantly lower than those of the Terzan 5's metal-rich population. Moreover, Terzan 5 does not exhibit the Al–O anticorrelation

observed in most GCs (though this feature is not universal).

Considering its striking chemical similarity to the Galactic bulge and its reconstructed orbit, which has always remained confined within the bulge (Baumgardt et al., 2019; Baumgardt and Vasiliev, 2021), the most plausible interpretation is that Terzan 5 is intimately connected to the early evolutionary history of the bulge itself. It could, in fact, be the relic of a more massive primordial structure that contributed to the early formation of the Galactic bulge, thus the definition as a Bulge Fossil Fragment (BFF).

This interpretation fits within a broader theoretical framework that describes bulge formation as the result of early fragmentation in a turbulent, gas-rich disk. Such a process is fully compatible with the hierarchical assembly of galaxies in the  $\Lambda$ CDM paradigm, where baryonic matter settles into dark matter halos and, under the influence of angular momentum, forms rotationally supported disks. According to the 3D

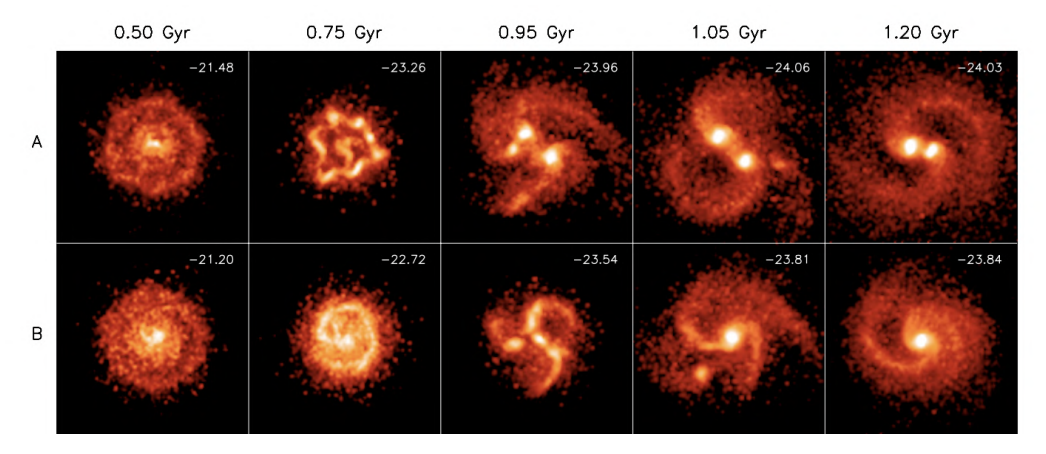


Figure 1.11: Morphological evolution of simulated disk galaxies (extract from Immeli et al., 2004). In both the cases shown here (case A and case B: see labels), the instability arises from the gas disk, with different levels of cooling efficiency (higher for case A, shown in the top row). This produces different levels of clumps in the simulation. Each panel corresponds to a different evolutionary time (0.5–1.2 Gyr).

chemodynamical model developed by Immeli et al. (2004), when energy dissipation is efficient, meaning gas cooling is effective, the disk becomes gravitationally unstable and fragments into massive clumps. These clumps are expected to have masses of the order of  $10^8-10^9 M_{\odot}$ , fully consistent with the estimated primordial mass of Terzan 5 ( $\sim 10^8 M_{\odot}$ ; Baumgardt et al. 2008). Such structures are predicted to spiral toward the Galactic center via dynamical friction, contributing to the build-up of the bulge and fueling its early starburst activity. Observational evidence for massive star-forming clumps has been found across a wide redshift range. At  $z \sim 1$ -5, HST imaging and integral field spectroscopy reveal turbulent disks hosting stellar clumps with typical masses up to  $10^9 M_{\odot}$  and sizes of  $\sim 1$  kpc (see Fig. 1.12; Elmegreen et al. 2008; Bour-

naud and Elmegreen 2009; Genzel et al. 2011). More recently, JWST has unveiled similar clumpy structures in galaxies at even higher redshifts ( $z \sim 10$ , see Messa et al. 2024; Adamo et al. 2024). This observational scenario is also well supported by cosmological hydrodynamical simulations (Ceverino et al., 2010). While most of these clumps are expected to fully coalesce and contribute to bulge formation, some simulations suggest that a fraction of them could survive disruption and now morphologically appear as globular clusters (Bournaud, 2016). Terzan 5 may have avoided disruption during the early bulge assembly as a dense structure that was displaced to the outskirts rather than dragged into the chaotic central regions. In this more quiet environment, it could have preserved SN ejecta over time, eventually giving rise to a metal-rich second stellar generation triggered by a later interaction with a bulge substructure. Terzan 5 thus represents the first bridge between resolved stellar archaeology in the Milky Way and the processes of galaxy formation at high redshift.

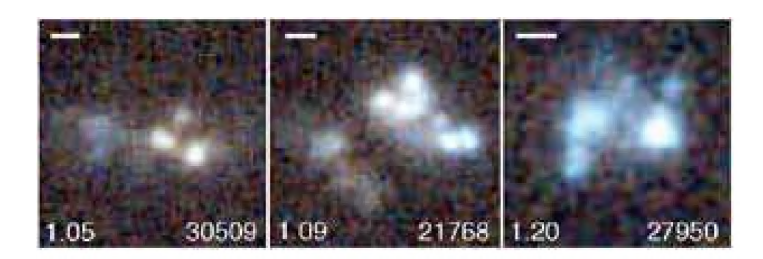


Figure 1.12: Skywalker images of clump galaxies observed in the Great Observatories Origins Deep Survey (GOODS). Each panel displays the galaxy's redshift (lower left), ID number (lower right), and a 2 kpc scale bar (upper left). These images reveal clumpy, spiral-like structures characteristic of galaxies at high redshift. From Elmegreen et al. (2009).

#### 1.4.2 Liller 1

Terzan 5 doesn't seem to be an isolated case. Liller 1 is another massive stellar system located in the inner Galactic bulge, at a distance of  $\sim 0.8$  kpc from the Galactic center  $(\alpha_{\rm J2000}=17^{\rm h}33^{\rm m}24.5^{\rm s},~\delta_{\rm J2000}=-33^{\circ}23'20'')$ . This GC-like system is located in an even more extincted region than Terzan 5, with an average color excess  $E(B-V)\simeq 4.5$  and reddening variations of  $\simeq 0.8$  (Pallanca et al., 2021). The two systems have comparable masses  $(M\simeq 1.5\times 10^6 M_{\odot})$  for Liller 1; Saracino et al., 2015).

Spectroscopic and photometric studies have revealed that Liller 1 also hosts multiple stellar populations with distinct chemical signatures, pointing to a similarly complex evolutionary history intimately linked to that of the bulge. Combining optical V and I data from ACS/HST and NIR (J,K) Gemini South Adaptive Optics Imager observations, Ferraro et al. (2021) discovered the presence of two main components of very

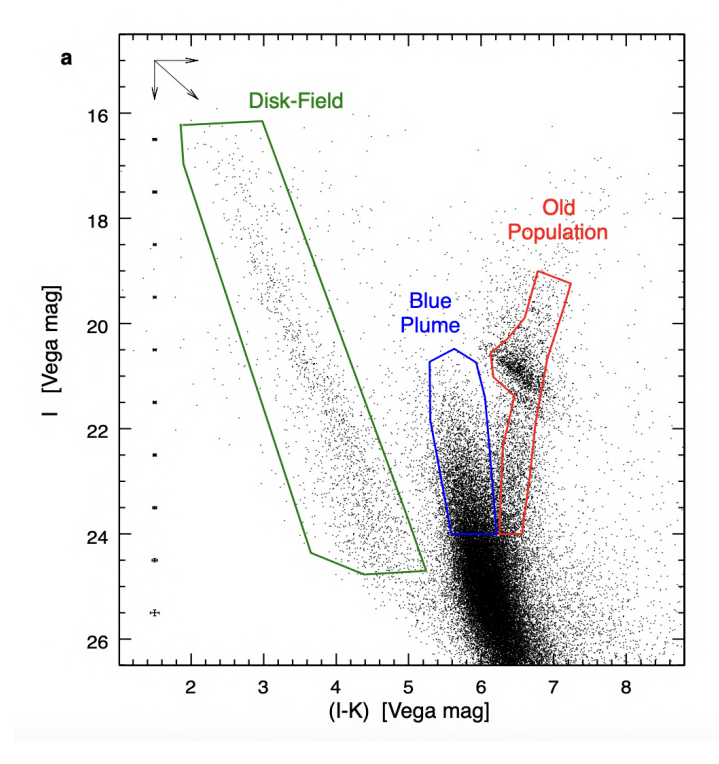


Figure 1.13: The (K, I-K) CMD of Liller 1 clearly revealing the presence of two main stellar populations: a  $\sim 12$  Gyr old component (marked with the red box) and a much younger sub-population (blue box). The stars included within the green box belong to the Galactic field. From Ferraro et al. (2021).

different ages: 1-3 Gyr for the youngest and 12 Gyr for the oldest. In the proper motion cleaned CMD, the former component appears as a "Blue Plume" of stars extending above the MS-TO, highlighting the occurrence of a younger star formation episode with respect to the one that generated the older GC-like population. The membership of the youngest population to the system was confirmed via density-distribution and proper motion studies. Spectroscopic follow-ups (see Fanelli et al., 2024 and references therein) uncovered a metallicity range of roughly 1 dex, comprising an older metal-poor population ([Fe/H]  $\simeq -0.5$ ), a younger metal-rich one ([Fe/H]  $\simeq +0.3$ ), and possibly a minor, intermediate-metallicity component with [Fe/H] $\simeq -0.1$ . As in Terzan 5, also in Liller 1 the oldest component is  $\alpha$ -enhanced (with  $[\alpha/Fe]\simeq +0.35$ ), while the youngest one has solar-scaled  $\alpha$ -element abundance (like the intermediate sub-population). The pattern drawn in the  $[\alpha/Fe]$ -[Fe/H] diagram is well consistent with that of bulge field stars, while it is totally incompatible with that of the Milky Way disk and halo, and those of dwarf galaxies.

The reconstruction of the SFH by Dalessandro et al. (2022) suggests that Liller 1 experienced an extended star formation activity with three dominant episodes: an early burst occurred 12–13 Gyr ago, followed by intermediate (6–9 Gyr) and recent (1–3 Gyr) activity. This pattern would support a self-enrichment scenario rather than a merger one. The evidence confirms that Liller 1 shares key characteristics with Terzan 5, identifying it as another case of Bulge Fossil Fragment.

Understanding the detailed evolutionary history of systems like Terzan 5 and Liller 1 is crucial to fully characterize their nature as BFF and to link them to the clumpy, star-forming structures observed at high redshift. In this context, the new analysis and age determination of Terzan 5 presented in this thesis, based on infrared photometry from the James Webb Space Telescope, provides a key step forward in the determination of its evolutionary timeline.

# Chapter 2

## The dataset

To conduct the photometric analysis of the stellar populations in Terzan 5 presented in this work, a combination of datasets from the James Webb Space Telescope (JWST) and the Hubble Space Telescope (HST) was employed. The primary dataset consists of proprietary deep infrared images obtained with the NIRCam instrument on board JWST, providing unprecedented sensitivity and resolution especially in highly reddened and crowded environments. In addition, archival HST observations were used, granting a complementary source of information in terms of both wavelength coverage and availability of different observational epochs. For the JWST dataset, an outline of the calibration pipeline processes is provided, as several parameters required accurate tuning in order to improve the image quality.

This chapter provides a detailed account of the datasets and the pre-reduction processing methods, along with an overview of the instrumentation and observational setups.

## 2.1 The James Webb Space Telescope

### 2.1.1 JWST insights into Terzan 5

The dataset used in this work was obtained as part of a broader study of Terzan 5: "Probing the existence of dark matter halos at parsec scale with JWST" (Cycle 3 GO Proposal ID: 5502, PI: F. Ferraro). The aim of these observations was to accurately sample the faintest end of the Main Sequence, in order to describe and characterize the stellar mass function down to  $0.2~M_{\odot}$ , and to obtain a higher-quality sampling of the MS-TO region.

For the specific science case and environment conditions, the main requirement to such an objective would be ultra-deep near-infrared photometry and high angular resolution. For this purpose, the James Webb Space Telescope and its NIRCam camera became the ideal choice. The high photometric quality provided by this dataset was also optimal for further investigations of Terzan 5's CMD, including the determination of its sub-populations' ages via the MS-TO, which is the main goal of this thesis.

#### 2.1.2 The instrument

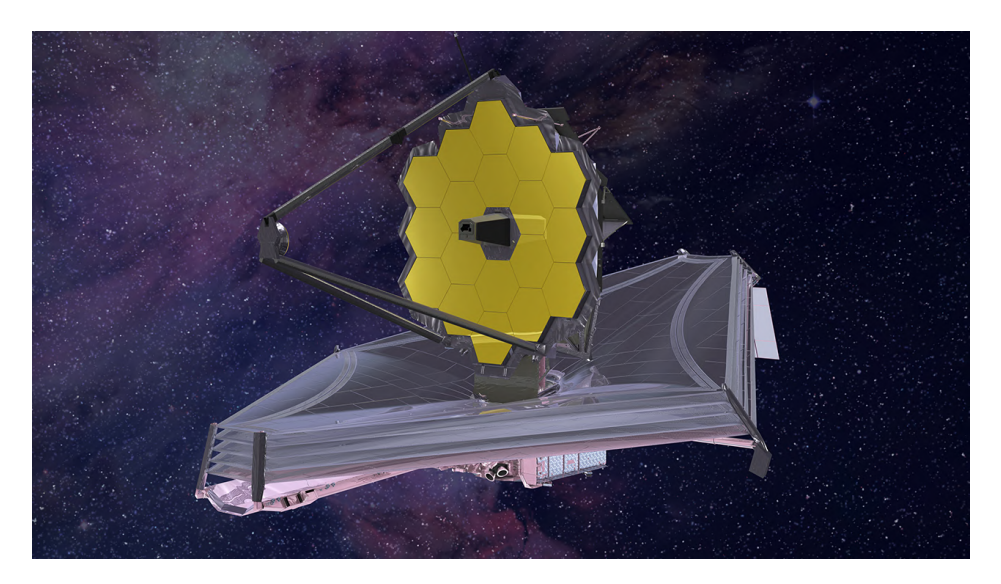


Figure 2.1: Illustration of the James Webb Space Telescope, ESA, CSA, Northrop Grumman NASA (c)

The James Webb Space Telescope (Fig. 2.1), launched in December 2021 through a collaborative effort between NASA, ESA, and CSA, holds the title of the most sophisticated and largest space observatory constructed to date. Its 6.5-meter primary mirror consists of 18 hexagonal beryllium segments, each coated with a 100-nanometer gold layer to enhance infrared reflectivity. Designed for structural efficiency and compatibility with the Ariane 5 launch system, each segment can be independently adjusted to form a precisely aligned concave surface capable of focusing light onto the secondary mirror with extreme precision. Light is then directed to the Science Instrument Module, located on the "Cold" or "Observing" Side.

The spacecraft's full structure (Fig. 2.2) is dominated by a  $21.2 \times 14.2$  meter sunshield designed to protect the telescope from visible and infrared light emitted by the Sun, Earth, and Moon. It essentially separates the observing part from the hot "Sun-Facing" Side. To ensure effective thermal insulation, the sunshield is composed of five distinct ultra-thin Kapton layers, an optimal heat resistant material, coated with aluminum and silicon. This side also includes: the Solar Array, which supplies JWST with electrical power; the infrastructure which controls all of Webb's operations known as the Spacecraft Bus; small telescopes for pointing and alignment called Star Trackers; and the High-Gain Antenna used for data transmission to Earth.

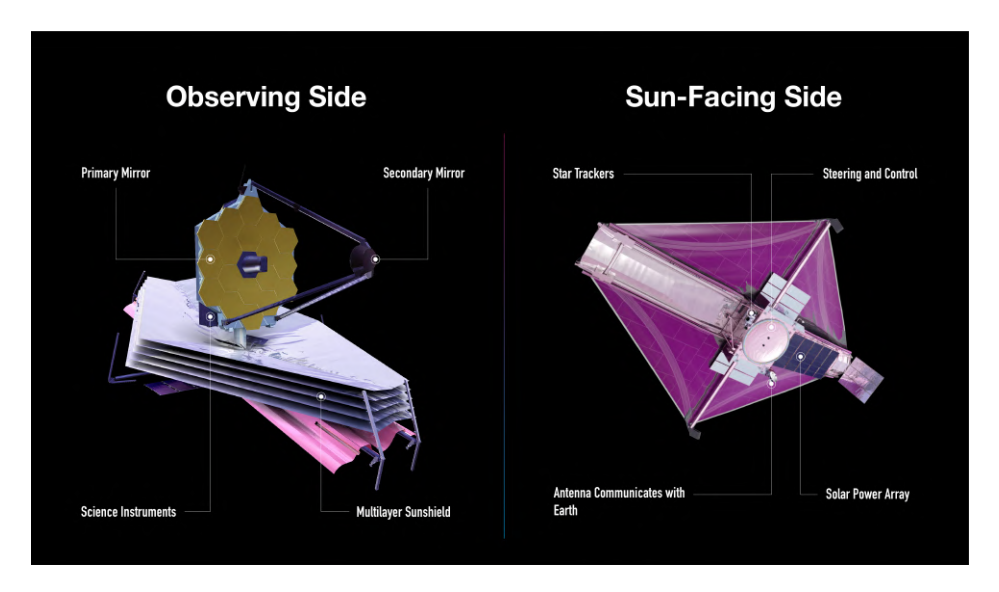


Figure 2.2: Labeled illustration of JWST structure, NASA (c)

JWST is designed for high-sensitivity and high-resolution observations in the nearand mid-infrared wavelength range (0.6–28.5  $\mu$ m). This capability is enabled by a state-of-the-art cooling system that maintains the telescope at cryogenic temperatures, below 50 K, effectively minimizing thermal emission from the instrument itself, which would otherwise contaminate infrared observations. This thermal control is achieved through the combined action of the large multilayer sunshield (whose Sun-facing side can reach temperatures up to 360 K), a passive cooling system, and an active cryogenic cooler specifically designed for the Mid-Infrared Instrument (MIRI). In particular, the operating temperature for the NIR detectors is maintained at approximately 33 K, while MIR observations require further cooling down to 7 K. JWST operates from L2, the second stable orbital position in the Earth-Sun gravitational configuration known as a Lagrangian point.

Its unprecedented observational capabilities, both from the photometric and spectroscopic perspective, include excellent sensitivity, subarcsecond angular resolution, and broad spectral coverage in the infrared range. All these features make JWST an essential tool for probing the Universe up to very high redshifts and for studying the most distant and faint galaxies. Moreover, it provides a completely new level of data quality for investigating stellar populations in environments like the Galactic bulge.

JWST is equipped with four scientific instruments: MIRI, NIRCam (Near-InfraRed Camera, 0.6–5  $\mu m$ ), NIRISS (Near-InfraRed Imager and Slitless Spectrograph), and NIRSpec (Near-InfraRed Spectrograph). Among them, the instrument best suited for photometric observations of resolved stellar populations in highly obscured regions, such as the Milky Way bulge, is NIRCam.

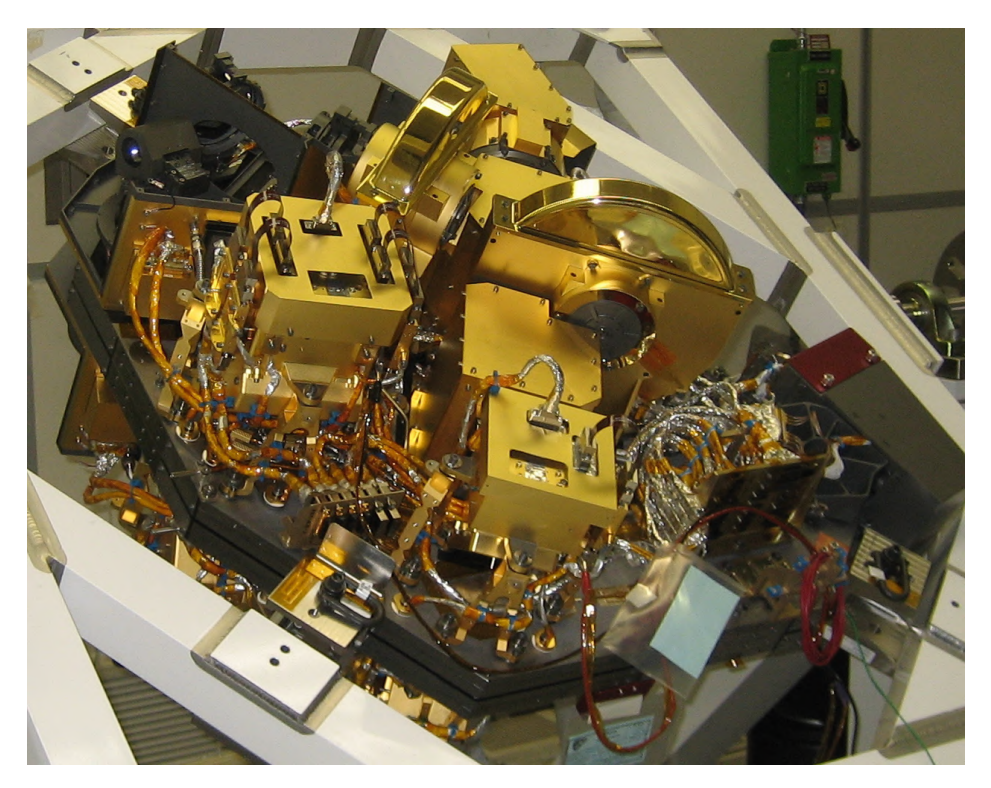


Figure 2.3: NIRCam modules mounted on the Integrated Science Instrument Module (NASA, JWST Near Infrared Camera )

### 2.2 NIRCam

NIRCam (Fig. 2.3) is the primary imaging instrument on board JWST and also plays an important role in wavefront measurements used to align the segmented primary mirror. Additional functionalities include coronagraphy, wide-field slitless spectroscopy, and time-series monitoring of variable sources.

Its operational wavelength range spans from 0.6 to 5.0  $\mu m$ , covered by a comprehensive set of 29 filters, with broad-, medium-, and narrow-band options, as shown in Fig. 2.4. NIRCam consists of two adjacent, nearly identical modules, each equipped with a dichroic beam splitter that enables simultaneous observations in a short-wavelength channel (0.6–2.3  $\mu m$ ) and a long-wavelength channel (2.4–5.0  $\mu m$ ). Each module provides a field of view (FOV) of approximately 2.2′ × 2.2′, with a 44" gap separating the two modules. The short-wavelength channel of each module is subdivided into four detector arrays, separated by 5" gaps, while the long-wavelength channel consists of a single detector per module. In total, NIRCam includes ten sensor chip assemblies, each with 2048 × 2048 pixels, of which 2040 × 2040 are light sensitive. In Fig. 2.5 the schematization of NIRCam's FOV and detector configuration is shown.

NIRCam's technical capabilities provide datasets vastly superior to those previously available for photometric studies on the Bulge, which drives its use in this study. The near-infrared filters F115W (J) and F200W (K) are optimal for sampling the faintest

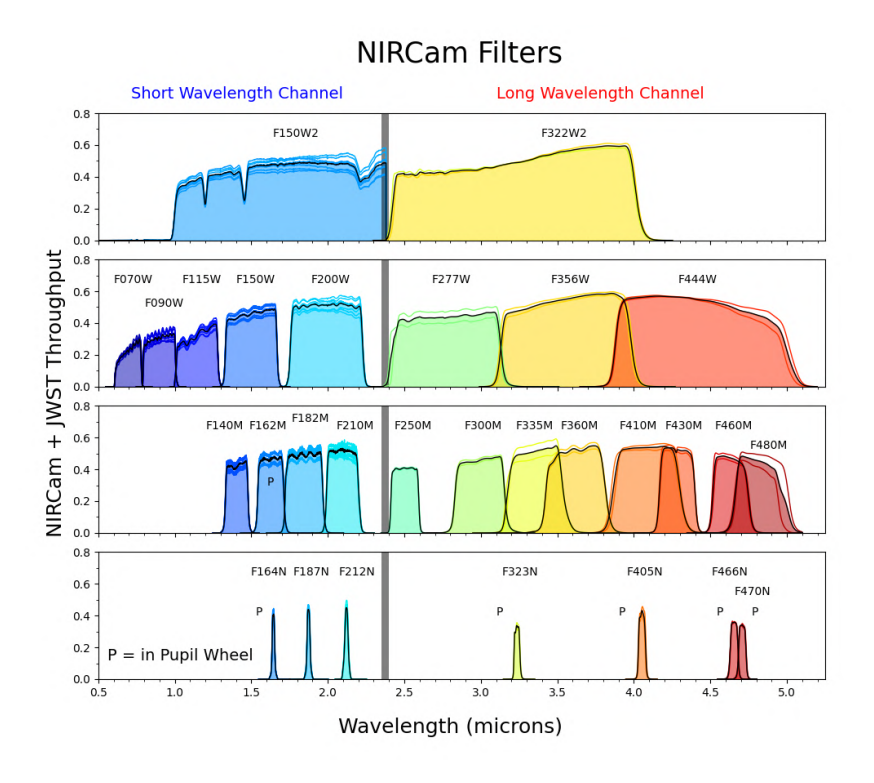


Figure 2.4: NIRCam available filters (NASA, JWST Near Infrared Camera)

end of the Main Sequence and distinguishing the two main populations in Terzan 5, particularly around the turn-off region, even in highly extincted environments. The unprecedented angular resolution of 0.031"/pixel at  $0.7~\mu m$  allows stars to be resolved even in the most crowded central regions, while the relatively wide total FOV ensures a complete and statistically robust analysis of the system's population and radial distribution. Furthermore, the dichroic configuration provided long-wavelength channel data in the F277W and F356W filters without requiring additional observation time.

#### 2.2.1 NIRCam Readout Patterns

Infrared detectors rely on non-destructive readouts, meaning that each exposure is divided into several integrations, each concluded by a reset. Within a single integration, as charge accumulates in the pixels, the detector is read out multiple times without clearing the signal, as illustrated in Fig. 2.7. Integrations are then averaged or "stacked", which allows to reach higher signal-to-noise ratios and decrease the readout noise per unit exposure time.

When designing an observation plan, different Readout Patterns can be selected based on the scientific goals, often with the aid of the Exposure Time Calculator (ETC). Each Readout Pattern specifies how the data points within an integration are obtained. For NIRCam the minimum time for a single non-destructive readout is 10.74 seconds, corresponding to one frame. Depending on the chosen pattern, frames may be averaged,

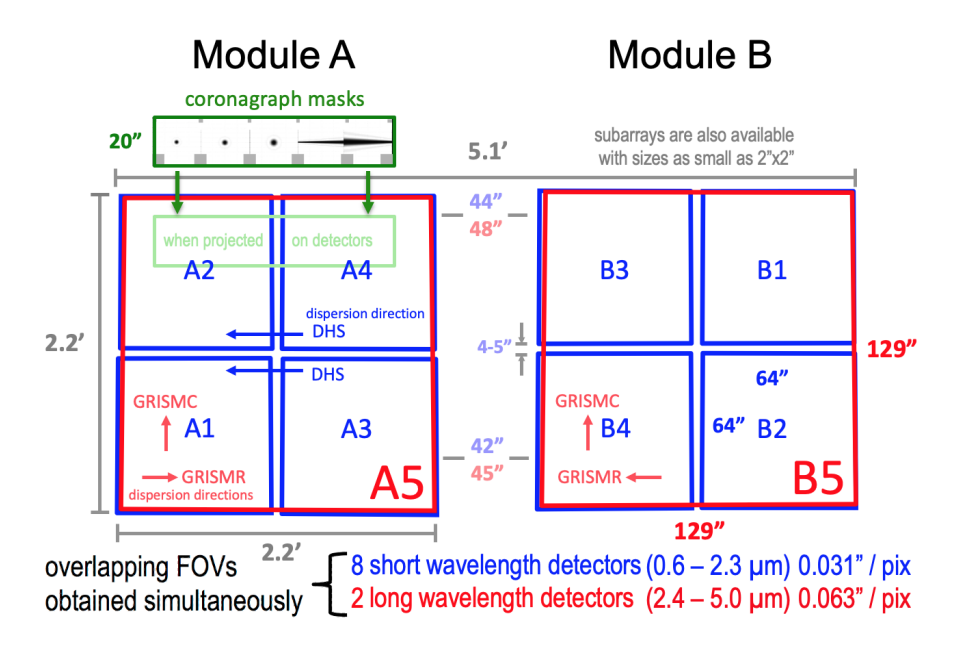


Figure 2.5: Schematic representation of NIRCam's FOV (NASA, JWST Near Infrared Camera )

summed, or skipped. The combination of a specific number of averaged and skipped frames defines a group, which is the smallest unit of data recorded by the instrument. Each integration can contain up to 20 groups. This strategy is necessary to reduce the amount of information to be stored in the onboard solid-state recorder which is downloaded twice a day and has capacity of approximately 57 GB: saving each individual frame would produce an amount of data corresponding up to 10 times the available storage.

There are 11 available Readout Patterns for NIRCam. Among these, RAPID and BRIGHT2 were used to obtain the dataset analyzed in this work. The RAPID pattern is designed for short exposures: in this configuration, each group consists of a single frame with no skips. For the data discussed in this thesis, the RAPID exposures consisted of a single integration, each containing two groups. The BRIGHT2 pattern, on the other hand, defines groups as averages of two frames with no skips. The observations relevant to this study include exposures of nine integrations for the F115W filter and seven integrations for the F200W filter, each composed of five groups. These two observational configurations provide access to both bright sources, via RAPID exposures, and faint sources, thanks to deeper BRIGHT2 integrations. An overview of the available patterns and group compositions is shown in Fig. 2.6.

Readout Patterns are the foundation of the "up-the-ramp" fitting method used to determine count rates in photometric observations. This approach provides several advantages: it reduces readout noise, yields average results from time-sampled data,

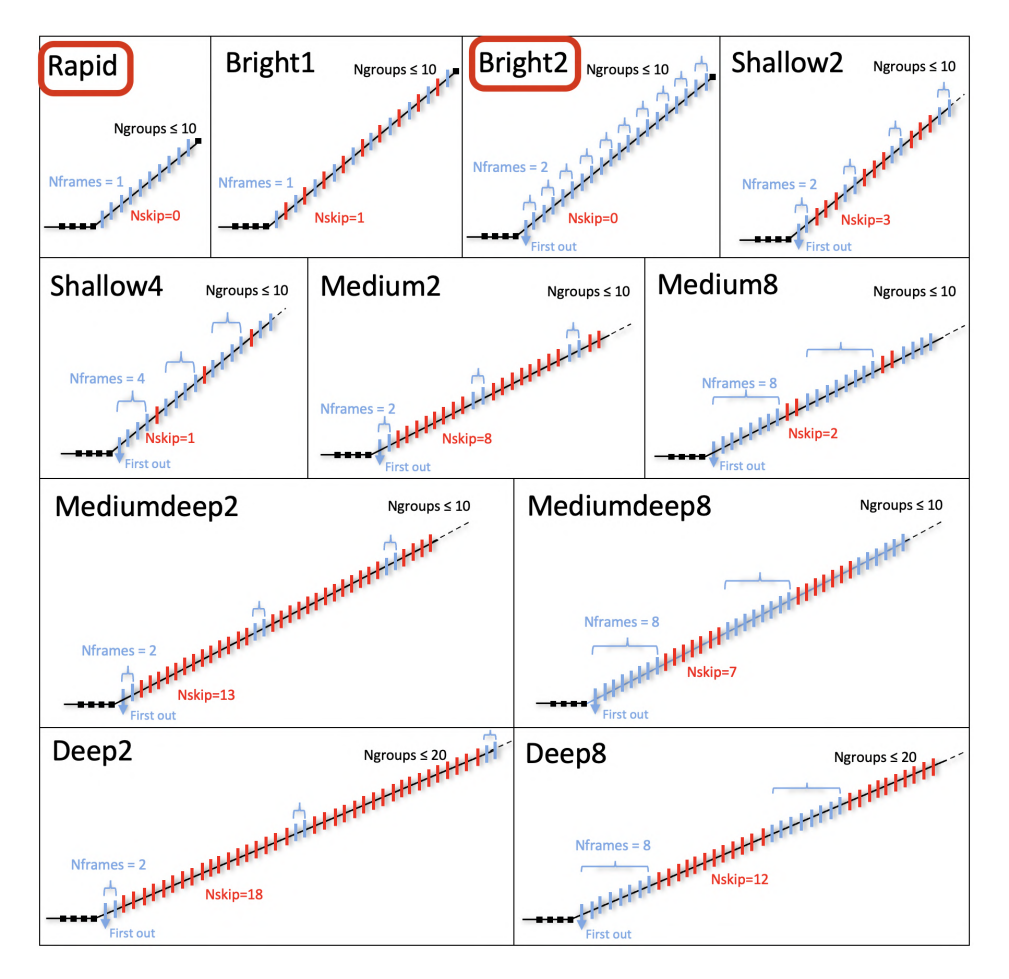


Figure 2.6: Available Readout Patterns for NIRCam and schematic view of group composition. The two chosen patterns for the dataset analyzed in this work are highlighted. (NASA, NIRCam Detector Readout Patterns)

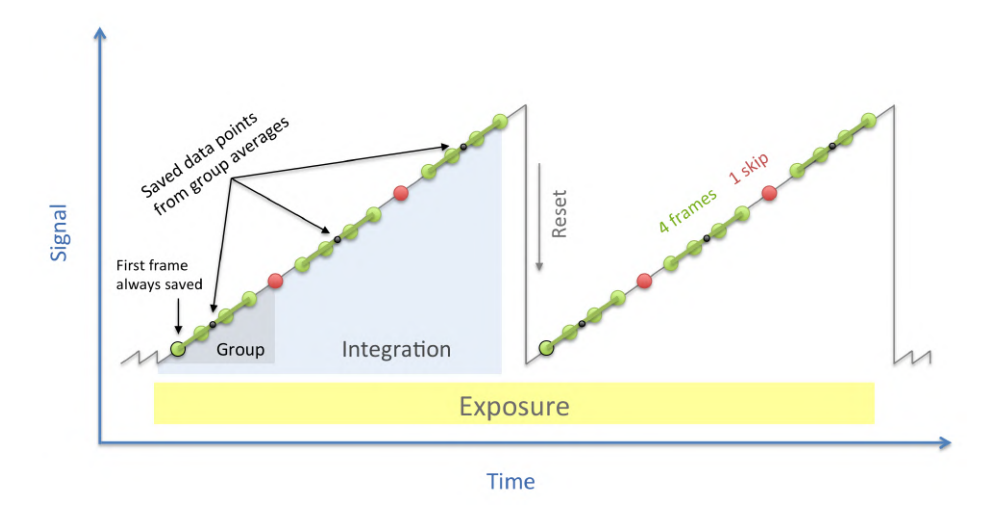


Figure 2.7: Graphical illustration of the up-the-ramp method for non-destructive readout of near-infrared photometric data by NIRCam detectors. (NASA, NIRCam Detector Readout Patterns)

facilitates cosmic ray detection, and allows for the recovery of saturated pixels.

#### 2.2.2 Frame 0

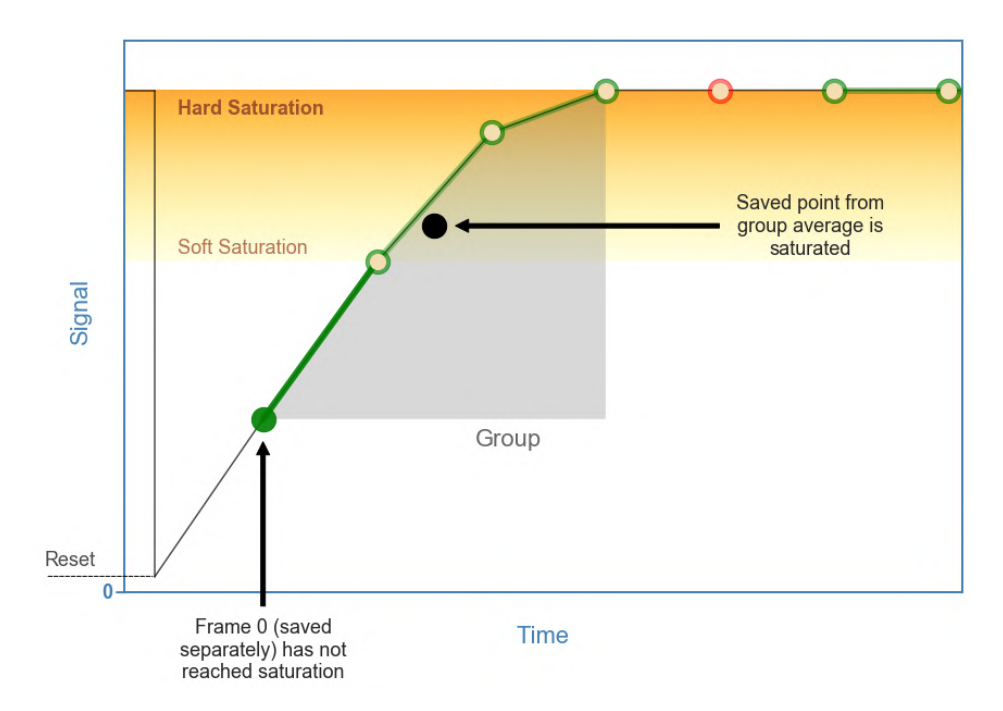


Figure 2.8: Schematic visualization of Frame 0 and its role in recovering information from potentially saturated pixels. (NASA, NIRCam Detector Readout Patterns)

Another major advantage of non-destructive readouts in infrared detectors is the increased dynamic range enabled by Frame 0, a feature specific to certain Readout Patterns. For the ones involving frame averaging, the signal collected during the very first interval, known as Frame 0, is saved in a separate extension of the output data. This allows recovery of information from pixels that saturate during the first group but not during the very first frame, as visualized in Fig. 2.8. This feature is particularly useful when analyzing JWST data of relatively bright sources such as nearby objects in crowded stellar fields, which are far more likely to suffer from saturation than typical high-redshift targets. In the context of this study, reducing saturation is critical to extending the measurable magnitude range and improving statistics on resolved stars, as saturation can also affect surrounding pixels.

Saturation thresholds for the various NIRCam detectors are provided in the JWST User Documentation and are typically around 60,000 ADU (Analog-to-Digital Unit), referred to each 10.74 second frame. Detailed values relevant to each chip are shown in Table 2.1.

#### 2.2.3 The dataset

The dataset this work is based on contains files from two separate visits to the target: the first between September 19th and 20th, 2024, and the second on April 4th, 2025 (Proposal ID: 5502, PI: F. Ferraro).

The first visit acquired images in both F115W and F200W filters, with a total of 8 dither positions for each filter and short-wavelength detector (A1, A2, ..., B4). For each quadruplet of sub-modules, the corresponding long-wavelength image in either F277W or F356W was also obtained simultaneously from the larger detector. This first set of images was acquired with both the BRIGHT2 readout pattern and the RAPID pattern, resulting in a total number of images effectively doubled for each dither and filter combination.

For the second visit, the resulting dataset consisted of 8 dither positions for each chip, all in F115W filter and BRIGHT2 pattern.

The dataset was downloaded from the JWST MAST portal, in the uncalibrated format. This was done to enable fine tuning of the calibration pipeline parameters for this particular science case. Unlike previous observatories like the Hubble Space Telescope, the JWST pipeline is unique to all its instruments and allows users to activate or deactivate specific corrections and procedures based on requirements such as photometry, spectroscopy, wavelength range, observation specifics, and research goals.

#### 2.2.4 Stage 1 Pipeline

The JWST Science Calibration Pipeline (Bushouse et al., 2025) is available to be installed by single users and accessed either through command line or Python interface, the latter of which was used for this work. Each of the 4 main stages is composed by a series of subsequent steps, which can be run with a unique stage-level command, or individually to apply specific corrections. The appropriate calibration reference files can be found within the Calibration Reference Data System<sup>1</sup> and are directly applied by the pipeline within each module.

The uncalibrated files in the FITS format contain raw single exposure data with information on the number of counts (DN) associated to each group in each integration, effectively creating the up-the-ramp readout.

The first stage of calibration consists of a sequence of detector level corrections designed to ensure a reliable estimate of the flux in each pixel. This is achieved through the up-the-ramp fitting procedure, which derives the count rate (expressed in DN/s) by estimating the slope of the accumulated signal over time. The result of this process is a set of uncalibrated slope images that serve as the starting point for subsequent

<sup>1</sup>https://jwst-crds.stsci.edu/

calibration steps.

This stage in particular required accurate fine-tuning, as it includes operations responsible for handling saturation and cosmic ray detections.

Detector	${ m Gain} \; ({ m e}^-/{ m ADU})$	Saturation (ADU)
A1	2.08	$60,300 \pm 1,760$
A2	2.02	$63,100 \pm 600$
A3	2.17	$59,300 \pm 220$
A4	2.02	$62,000 \pm 1,330$
B1	2.01	$62,300 \pm 440$
B2	2.14	$61,000 \pm 360$
В3	1.94	$62,500 \pm 860$
B4	2.03	$61,000 \pm 520$

Table 2.1: Gain and Saturation values for NIRCam's detectors (NASA, JWST Near Infrared Camera ).

In the context of very crowded stellar fields observed in the near-infrared, saturation is expected to be the dominant issue; the main objective should therefore be to recover as many usable pixels as possible by minimizing unnecessary flagging. Several parameters regulate the treatment of possibly corrupted pixels, and these can be manually adjusted using the Python script for the pipeline.

When the first stage of the pipeline is executed, the process begins with data quality initialization: calibration reference files are used to assign quality flags to pixels affected by detector-specific issues, identifying for example hot or dead pixels. These flags can be updated by subsequent steps as additional issues are identified. Preliminary uncertainty estimates are assigned to each pixel, which the pipeline will update as well by using a noise model, ensuring accurate error propagation throughout the calibration process which accounts for different sources of noise.

The pipeline then performs a saturation check. Saturation occurs when the detector's linear response to incoming photons breaks down due to instrumental limitations, typically at high signal levels where the relation between photon flux and digital counts (DN or ADU) no longer holds. Calibration reference files define the saturation threshold: if a pixel's ADU value exceeds this limit, a group-level data quality flag is set. The pipeline also accounts for charge migration and possible non-linearity by flagging surrounding pixels. A specific parameter n\_pix\_grow\_sat controls the radius, in pixels, of the area flagged around a saturated pixel. Let n represent this input value, 2n+1 pixels will be flagged; for this work, the default value of 1 was used.

When analyzing detector readouts, it is essential to account for additional counts in each pixel due to electronics. Ideally, this would consist of a constant value of counts across the entire pixel grid. However, in practice, there are often row-dependent variations, which are estimated using non-light-sensitive pixels located at the edges of the detector (4-pixel wide strips for NIRCam) and corrected during the Reference Pixel Check.

The following crucial step is known in the documentation as the Jump Step: events like cosmic ray impacts can lead to "jumps" in the ramps due to an excess of charge. These are identified by the pipeline by using a threshold value in sigmas above which the change in counts between two groups is classified as a jump.

The core of this first stage of the calibration pipeline is the Ramp Fitting procedure, which estimates the slope of the signal accumulation over time for each pixel by performing a linear least squares fit using optimal weighting: this constitutes the first uncalibrated value for the flux. During this step, the data quality flags set up to this point come into play, as they determine which pixel count values are actually used for flux estimation. Therefore, appropriate flagging of jumps, saturation, and charge migration is crucial to ensure accurate scientific measurements.

All the previously described steps are always performed, independently of the JWST instrument used to collect data. There are however several NIRCam-specific calibrations. Calibration reference files are used to determine the appropriate superbias subtraction to correct for additional counts due to electronics, followed by linearity correction to account for detector response deviations due to gain variability. This leads us to introduce two fundamental quantities in the analysis of photometric images (or any astrophysical observational dataset): gain and readout noise. Gain is defined as the conversion factor between the number of electrons collected in a pixel and the analog-to-digital units (ADU); readout noise is instead due to random fluctuations introduced during the process of reading the signal from the detector and converting it into a digital number. These values should be known in order to perform a coherent photometric analysis and NIRCam specific values were recovered from the documentation for the following photometric steps as described in Chapter 3.

Additional corrections performed at this stage include Persistence Correction, Dark Subtraction and Charge Migration. Having described the main operations performed by the pipeline, we can present the main adaptations that were done from the default settings in order to best manage the data for the science case at hand.

For this work, the key modification was enabling suppress\_one\_group = "False" during the ramp-fitting step. This adjustment enables the pipeline to recover the count values of pixels that are saturated from the first group but not in Frame 0, which would normally be flagged and thus ignored. As a result, the pipeline returns a rate value for those pixels and correctly accounts for, and propagates, the additional uncertainty introduced by fitting the slope using only a single data point. This approach significantly extends the dynamic range of the image, preserving information in high-signal regions such as the densest areas of the stellar system that would otherwise be lost. When comparing results with and without this pipeline modification, the most notable

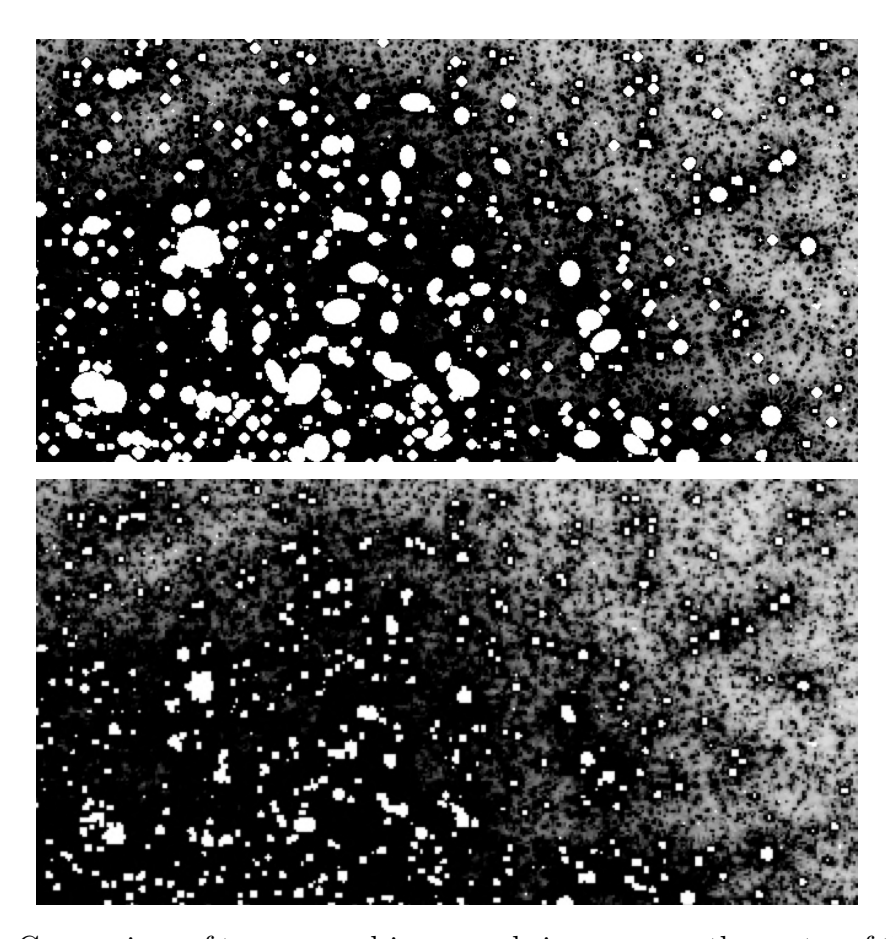


Figure 2.9: Comparison of two zoomed-in example images near the center of the system. The top panel shows uncalibrated data processed with default parameters. The bottom panel shows the same data processed with the option to recover good frame 0 exposures. The colour scale is inverted, making null pixels appear white. This comparison clearly demonstrates that the changes applied to the pipeline have significantly reduced the number of flagged saturated pixels and artifacts.

improvement was observed in BRIGHT2 F200W images, meaning the longest and reddest exposures, which are most prone to saturation. An example of such a comparison for this image type is shown in Fig. 2.9.

Another critical step that required particular attention was the Jump Step. As of pipeline build 9.0, this step includes accounting for excess charge that may spill into neighboring pixels during particularly energetic cosmic ray events. These events can range from affecting just 1–2 pixels to creating large artifacts involving hundreds of pixels. In the near-infrared regime, such features are referred to as "snowballs" due to their appearance on the detectors as circular artifacts centered on the saturated pixels associated with the cosmic ray hit. These artifacts arise from excess charge that alters



Figure 2.10: The figure illustrates a typical snowball correction performed by the default JWST science calibration pipeline (JWST User Documentation)

the pixel slope in a way that is not easily detected, as the signal typically falls below the detection threshold for jumps. Nonetheless, such effects can influence magnitude estimates. The JWST Pipeline Guide therefore recommends that users working with NIRCam data set expand\_large\_events = "True" in the Jump step, enabling the pipeline to account for these effects, as illustrated in Fig. 2.10.

Along with this change, other parameters were set and fine-tuned to efficiently detect affected pixels while minimizing overflagging: mask\_snowball\_core\_next\_int = "False", only\_use\_ints = "False", rejection\_threshold = 5.0.

However, upon closer inspection of the resulting images after applying this correction, some artifacts seemed to appear near bright stars with saturated cores (or non linear regimes very close to saturation). An example of this is shown in Fig. 2.11, where noticeable white rings (in colour-inverted images) frequently appear at the edge of some stellar profiles, as if excess charge were being incorrectly removed during the image's processing.

The most likely cause for this effect is that the pipeline can mistakenly identify saturated cores of very bright stars as cosmic ray hits, thus triggering the snowball subtraction. This problem was also highlighted in the Outstanding Issue section of the JWST Technical Report on "Detection and flagging of showers and snowballs in JWST" (Regan, 2024). Since no direct solution is currently available or recommended in the JWST pipeline documentation, the most reasonable approach for the present

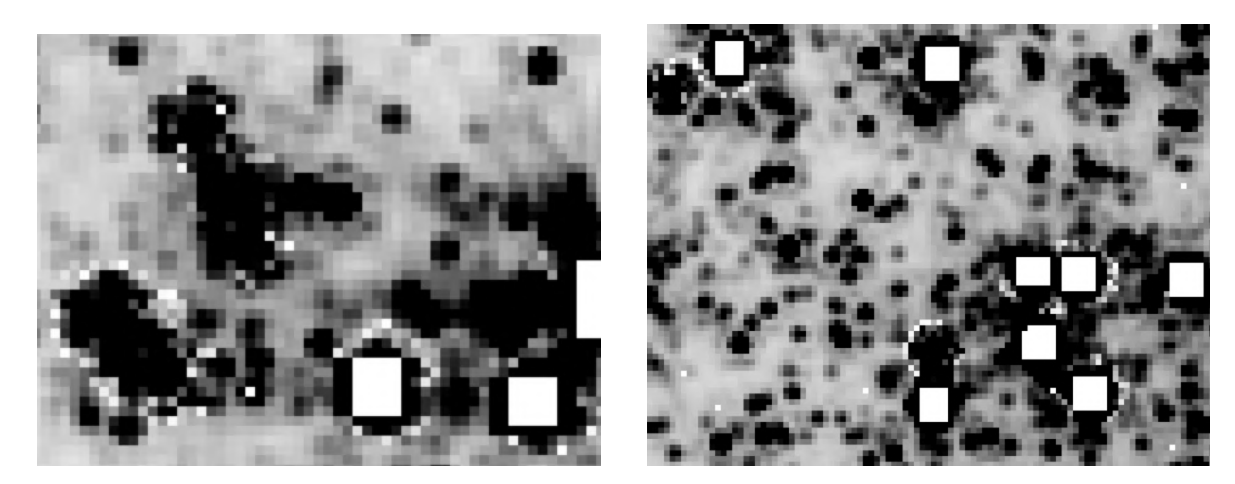


Figure 2.11: Zoomed-in regions of example images where the snowball correction was applied by the pipeline, resulting in multiple artifacts around bright stars.

	expand_large_events: True	expand_large_events: False
n_pix_grow_sat:	200	99
n_pix_grow_sat:		89

Table 2.2: Effect of expand\_large\_events and n\_pix\_grow\_sat parameters on F200W BRIGHT2 images. The final value for both was chosen as the combination that minimizes the presence of overflagging and artifacts, so respectively "False" and 1.

case was to set expand\_large\_events = "False", effectively disabling snowball detection. This choice was made because this type of misidentification in a very crowded stellar field resulted in hundreds of stars being affected in each image, impacting at least ten times as many pixels. Although snowballs have a typical occurrence rate of approximately 1 every 20 seconds, in some exposures they may not appear at all. Nevertheless, when present, they can be manually identified and removed if needed, as their number would generally be lower than the number of artifacts produced by automated correction. Additionally, there is reason to believe that the subsequent algorithm used to identify stars through PSF fitting, along with its associated quality parameters, would naturally exclude pixels affected by such artifacts.

## 2.2.5 Stage 2 Pipeline

The second Stage of the pipeline mainly deals with instrumental calibration of initial flux values provided by the first stage, giving as output the calibrated data from individual exposures.

Its main steps include flat field correction, flux calibration and WCS creation. The latter simply associates the correct astronomical coordinates to the pixel scale, information which is then stored in the datafiles. Flux calibration is performed, converting DN/s values to MJy/sr; however, for some of the subsequent reduction steps, it was preferable to work with raw counts, as they better suited the requirements of the photometric analysis performed with DAOPHOT (see Chapter 3) This was achieved using the conversion factors stored in the header by the pipeline during this Stage 2 step. Flat fielding was the most relevant step for our purposes, as it provides a correction for both pixel-to-pixel and large scale variations in the instrumental response. This is typically done by dividing the observed image by one obtained under uniform illumination, like the one shown in Fig. 2.12, where any variation across the detector is attributable solely to the detector's response. The JWST pipeline applies this correction using appropriate reference files.

For this thesis, all Stage 2 parameters were left at their default values.

Processing was deliberately stopped after Stage 2, since the calibrated outputs produced at this stage met all the requirements for the analysis carried out in this work. In terms of JWST pipeline data products, the images obtained through this process are the so-called "cal" images, meaning calibrated exposures in detector space.

The "i2d" images were also obtained, meaning rectified, calibrated 2D, sky-projected images. Although i2d products were not employed in the following photometric reduction, they were useful for visual inspection due to their calibrated and geometrically corrected format.

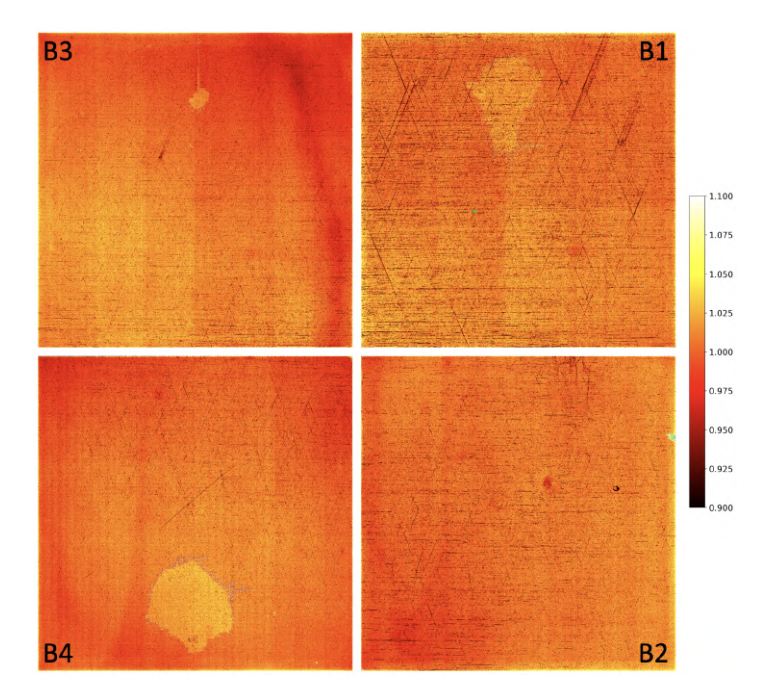


Figure 2.12: Flat fields of the B module of NIRCam (NASA, JWST Near Infrared Camera )

#### 2.2.6 Calibrated data products

The final step before performing the actual photometric analysis on the JWST data was the correction for the Pixel Area Map (PAM), which accounts for geometric distortion caused by pixel area variations. This correction is essential to ensure the success of both aperture and PSF photometry.

In JWST data products, the PAM information is stored in index 4 of the Science Extension: each image was thus multiplied by the corresponding pixel area map. The whole dataset was also converted to "float32" format in order for it to be legible for the reduction softwares.

Furthermore, to maintain consistency across different types of exposures and ensure that the primary photometric software (DAOPHOT) correctly interpreted the data, all fluxes were converted to simple count values by multiplying them by the duration of a single frame (10.74 s).

Finally, since the software used is optimized for typical optical astronomical data, where saturated pixels are characterized by very high count rates, all "NaN" pixels were assigned a value of 100,000.

# 2.3 Completing the dataset: HST observations

## 2.3.1 The Hubble Space Telescope

Launched by NASA in 1990, the Hubble Space Telescope (HST) has become a pillar of modern astronomy, helping to drive some of the most groundbreaking discoveries over the past 35 years. Its observations continue to be extensively studied and fuel new scientific breakthroughs.

Unlike JWST, Hubble was placed in Low Earth Orbit at an altitude of approximately 540 km and was specifically designed to be accessible for regular Servicing Missions carried out by astronauts. This level of maintenance is not possible for other observatories such as JWST, Euclid, or Gaia, which operate around the second Lagrange point (L2), located about 1.5 million kilometers from Earth. The ability to repair, upgrade, and even replace instruments proved fundamental to Hubble's longevity and scientific productivity.

Hubble is a reflective telescope with a Cassegrain configuration: light is first collected by the primary mirror and reflected to the secondary mirror, then directed through the focal plane to the scientific instruments, either a camera or a spectrograph, and finally onto the detector. The primary mirror has a diameter of 2.4 meters, the secondary of only 30.2 cm, while the entire telescope tube measures 13.2 meters in length and 4.2 meters in width. The spacecraft is powered by two solar arrays and stores electrical energy in six nickel-hydrogen batteries. The full structure is shown in Fig. 2.13.

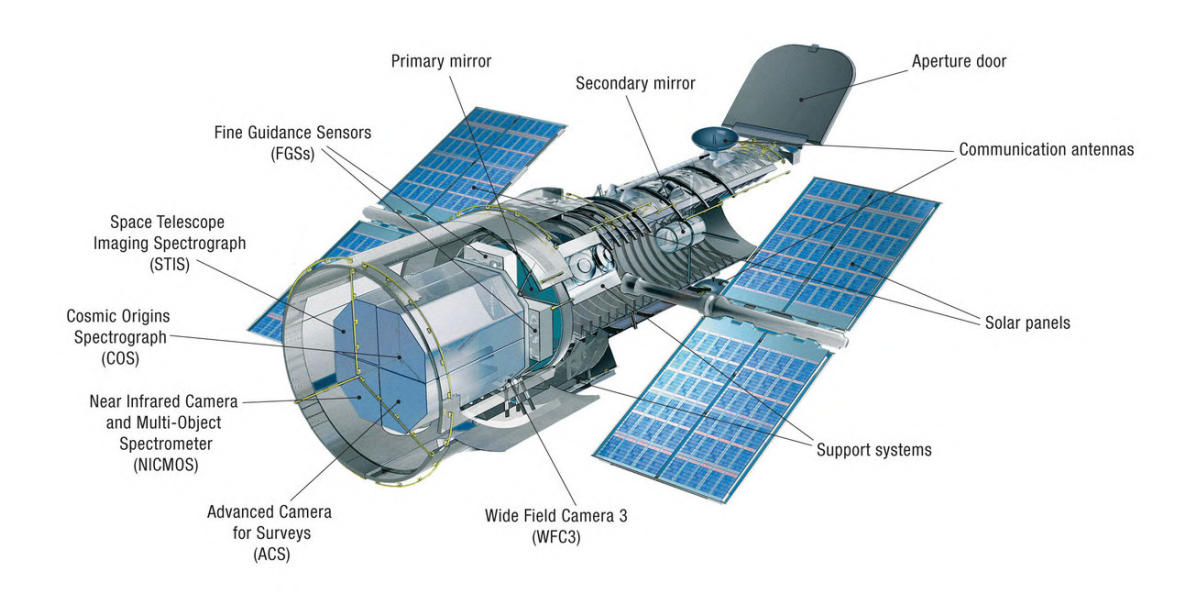


Figure 2.13: Labeled illustration of the Hubble Space Telescope, NASA (a)

Many instruments have been deactivated or decomissioned over the years. Currently,

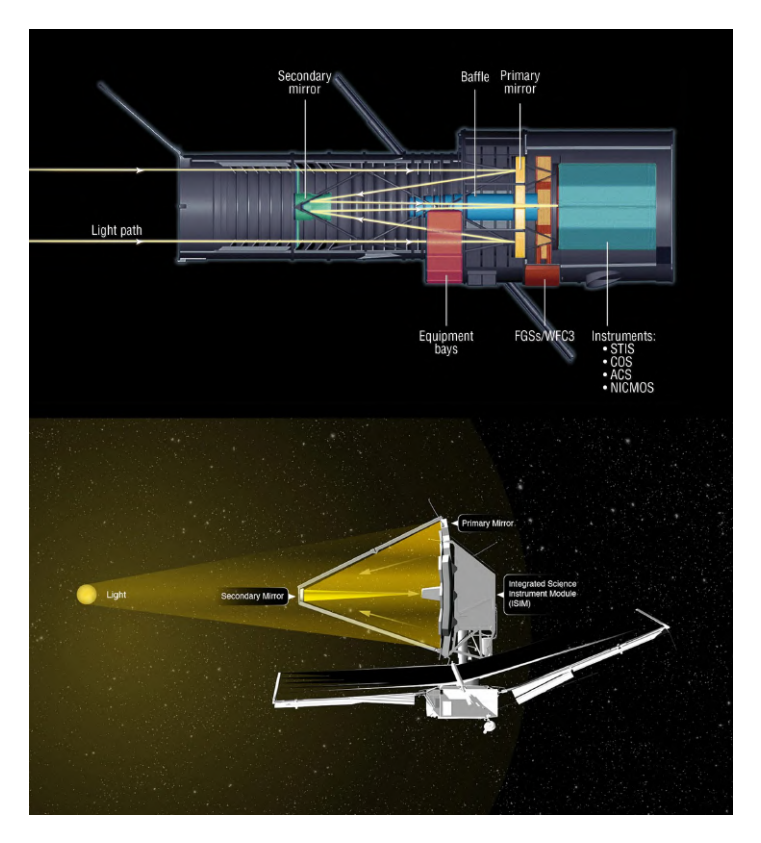


Figure 2.14: Comparative illustration of Hubble and James Webb Space Telescope, NASA (b)

Hubble has 5 working instruments: Advanced Camera for Surveys (ACS), Wide Field Camera 3 (WFC3), Cosmic Origins Spectrograph (COS), Space Telescope Imaging Spectrograph (STIS) and Fine Guidance Sensors (FGS); they cover a wide range in wavelength, spanning from the ultraviolet, visible, up to near-infrared light (a comparison with JWST's range is shown in Fig. 2.15). For this work, the dataset was obtained using the ACS, which is the instrument we will focus on.

ACS is the main imaging system onboard the Hubble Space Telescope, installed in 2002 during Servicing Mission 3B. Covering wavelengths from 115 nm to 1050 nm, it includes three independent channels: the Wide Field Channel (WFC), the High Resolution Channel (HRC), and the Solar Blind Channel (SBC). While the HRC has been unavailable since 2007 due to an electronics failure, the WFC is still operational and remains one of the most frequently used instruments on HST. It is optimized for deep, wide-field imaging and consists of two adjacent  $4096 \times 2048$  CCDs, known as WFC1 and WFC2, which are sensitive to light from the blue end of optical to the near-infrared light (approximately 350–1100 nm). These detectors produce a combined field of view of  $202" \times 202"$ , with a 2.5" gap between the two chips. The pixel scale of 0.05"/pixel enables high-resolution imaging, significantly surpassing what was achievable from ground-based telescopes before the era of adaptive optics.

This capability has greatly enhanced the study of various astrophysical phenomena, particularly in the analysis of stellar populations. The Point Spread Function (PSF) Full Width at Half Maximum (FWHM) for ACS ranges from 0.1" to 0.14", depending on the filter and wavelength. A wide variety of filters are available for observations, including broad-band (e.g., F435W, F606W, F814W), medium-band, and narrow-band filters, enabling targeted studies of both continuum emission and specific spectral lines.

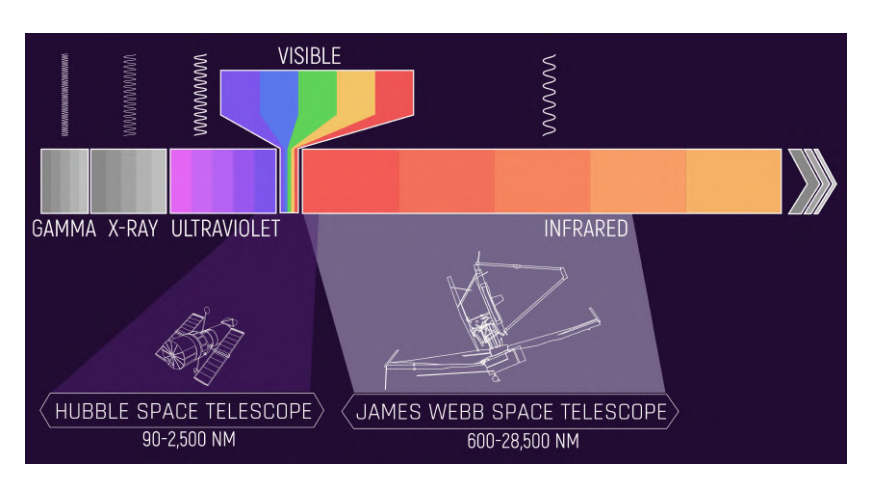


Figure 2.15: Comparison of Hubble and James Webb Space Telescope wavelength ranges, NASA (b)

#### 2.3.2 The HST dataset

The dataset analyzed in this work was retrieved from the Mikulski Archive for Space Telescopes (MAST). Three distinct epochs of observations were available, all centered on Terzan 5 and acquired with the ACS/WFC using the F606W and F814W filters. The first set of observations was obtained on September 17, 2003 (Proposal ID: 9799, PI: Rich) and consists of one long exposure of 340 seconds in F606W, and three exposures in F814W: one long exposure of 340 seconds and two short exposures of 10 seconds each.

The second set was acquired between August 18 and 19 in 2013 (Proposal ID: 12933, PI: Ferraro), comprising six exposures per filter. In the F606W filter, five long exposures of 365 seconds and one short exposure of 50 seconds were obtained, while in F814W, five long exposures of 365 seconds and one short exposure of 10 seconds are available.

The third and final set was acquired between April 20 and 21 in 2015 (Proposal ID: 14061, PI: Ferraro), again consisting of six exposures per filter. For F814W, the dataset includes one short exposure of 10 seconds and five long exposures ranging from 370 to 372 seconds. Similarly, for F606W, one short exposure of 50 seconds and five long

exposures ranging from 397 to 398 seconds were acquired.

Unlike in the JWST case, these images were downloaded with calibrations already applied, more specifically in the "FLC" format: calibrated, flat-fielded and CTE-corrected single exposures. The "DRC" (drizzled, distortion-corrected) images were also obtained, which are conceptually similar to the i2d products available for JWST data. Both are fully calibrated, geometrically corrected, and projected onto a common astrometric grid, making them particularly useful for visualization and initial inspection. The main difference being DRC images combine multiple exposures.

The PAM correction was applied by using the appropriate Python package stsci.skypac and the contained function pamutils.pam\_from\_file which creates the corresponding Pixel Area Map for each exposure. Lastly, the dataset was converted to "float32" format for proper software reading during the photometric reduction.

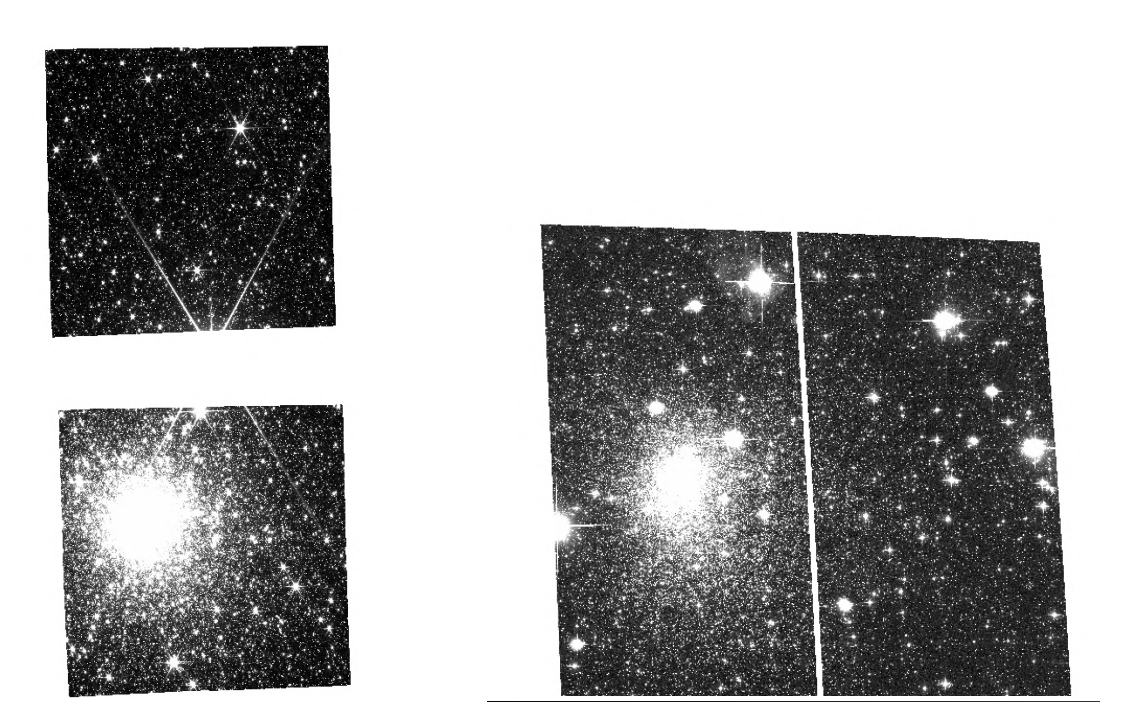


Figure 2.16: Comparison between the fields of view covered by JWST's NIRCam (left) and HST's ACS (right) of Terzan 5. The images shown are representative examples, selected respectively from the second epoch of JWST observations and the first epoch of HST observations.

#### 2.3.3 The final dataset

A summary of the complete dataset used in this work is presented in Table 2.3. In Fig. 2.16 an example of the FOV of the two different telescopes during the obtained Terzan 5 observations is shown.

Instrument	Year	Filter	Exposures	Exposure Time (s)
	2003	F606W	1	340
		F814W	1	340
			2	10
	2013	F606W	5	365
			1	50
HST		F814W	5	365
			1	10
	2015	F606W	3	397
			2	398
			1	50
		F814W	3	371
			2	372
			1	10
JWST	2024	F115W	8 BRIGHT2	966.4
			8 RAPID	21.47
		F200W	8 BRIGHT2	751.6
			8 RAPID	21.47
	2025	F115W	8 BRIGHT2	966.4

Table 2.3: Summary of the JWST and HST observations used in this work. The long-channel images for JWST in filters F277W and F356W were excluded from the reduction and only used for geometric transformations.

# Chapter 3

# Photometric reduction

This chapter aims to provide a comprehensive description of the photometric reduction steps for both datasets outlined in the previous section. The ultimate goal of these procedures is to obtain accurate position and magnitude values for the final catalogue of stars belonging to Terzan 5.

The techniques described are based on robust PSF fitting photometric procedures that have been consolidated over the years, adapted here for the newly acquired JWST data. The primary focus remains on the NIRCam dataset, with the goal of constructing an F115W-F200W Colour-Magnitude Diagram to facilitate an in-depth study of the ages of the two stellar populations. However, the HST reduction is also described, as it plays a crucial role due to the availability of multiple epochs allowing for an accurate proper motion determination.

# 3.1 Photometric techniques: PSF fitting

For any imaging system, point sources such as stars do not appear as perfect points in the resulting image, but rather their light is distributed over several pixels due to a combination of optical and detector related effects. The shape of this light distribution is described by the Point Spread Function (PSF), which characterizes how a point source is recorded by the system and depends on both the instrument and observational conditions. In analytical terms, the delta-dirac function, which would describe a perfect point source, is convolved with the detector response generating a broader gaussian-like curve.

In the particularly favorable case of HST and JWST, the absence of atmospheric turbulence eliminates one of the dominant sources of PSF broadening present in ground-based observations. As a result, the PSF in these space-based instruments is primarily determined by the optical response of the telescope itself, making it effectively diffraction limited with a pattern often known as an Airy Disk.

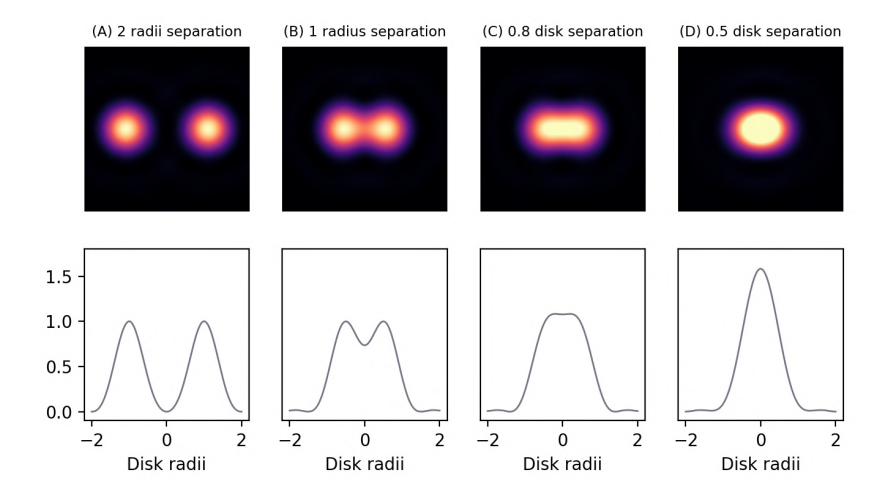


Figure 3.1: Figure from Bankhead et al. (2023) illustrating Airy patterns, diffraction patterns produced when light passes through circular apertures, separated by different distances. The bottom row shows intensity profiles computed across the centers of the patterns.

In order to estimate the magnitude for each star, the most common approach is thus PSF fitting: a best-fit model of the PSF shape is built across the image using a sample of suitable reference stars, selected for their isolation and high signal-to-noise ratio, and fitted to each source. The flux is then estimated by computing the integral of each fitted PSF model, to account for the total emitted light. This is a model-based method that relies on the accuracy of the PSF shape determination

A more direct technique is known as aperture photometry, which consists of summing all the counts within a circular aperture of chosen radius around the star, and subtracting the background contribution estimated from an outer concentric annulus. This approach is not only simpler, but also theoretically exact, as it does not include modeling techniques but accounts for each photon count. However, this is an approach that can only be effective for isolated sources and becomes quite inaccurate in very crowded fields where background estimates are not as easily obtained and stars can be blended. In these cases, like the one presented in this work consisting of the central region of a globular cluster-like system, PSF fitting proves to be the most accurate and reliable option. The formula for magnitude estimation in the two cases is defined as follows:

$$m = \begin{cases} -2.5 \log(C - A \times B) & \text{(aperture photometry)} \\ -2.5 \log(V) & \text{(PSF fitting)} \end{cases}$$
 (3.1)

where C is the sum of counts in the aperture, A is the area in pixels of the aperture, B is the mean count/pixel ratio calculated in the background annulus, V is the integral under the PSF curve.

Another advantage of PSF modeling for each source is the possibility to determine

the curve's peak, which is the estimated centroid of the star. This makes for an accurate determination of positions which is fundamental in the proper motion calculation. Typical PSF shapes for JWST are shown in Fig. 3.6.

# 3.2 Daophot II photometric reduction

#### 3.2.1 JWST dataset

The main photometric analysis of the JWST dataset was carried out using the *DAOPHOT II* software package (Stetson 1987, Stetson 2011) incorporating also the stand-alone programs *Allstar* and *Allframe*, often used in conjunction. These tools are designed to detect point sources in two-dimensional astronomical images, perform aperture photometry, model the PSF, and fit this model to each identified source to derive accurate magnitude estimates and astrometric positions.

Running DAOPHOT requires the user to provide several key input parameters specific to each dataset. The most fundamental among these are the readout noise and gain values. The reference values for NIRCam can be found in the JWST User Documentation: the gain is reported as  $2.05 \pm 0.4 \,\mathrm{e^-/ADU}$ , while the readout noise is  $15.77 \pm 0.94 \,\mathrm{e^-}$ . However, these values refer to a single frame. Although the frame time of  $10.74 \,\mathrm{s}$  was used to convert to integer count rates, the final images were produced by averaging or summing multiple frames, which significantly alters the noise characteristics. The correct way to adjust the gain and readout noise in these cases is described in the DAOPHOT II manual, and summarized in Table 3.1.

	If N frames were averaged	If N frames were summed
photons/ADU	$p(N) = N \cdot p(1)$	p(N) = p(1)
read-out noise	$R(N) = \frac{R(1)}{\sqrt{N}}$	$R(N) = R(1) \cdot \sqrt{N}$

Table 3.1: Effect of averaging or summing N frames on gain and read-out noise as shown in the  $Daophot\ II$  manual

Firstly, one needs to convert the readout noise from electrons to ADU by dividing by the gain value: this yielded approximately 7.70 ADU. The final readout noise and gain values then vary depending on the Readout Pattern used, as determined by the number of frames combined in each case following the guidelines.

Another key parameter that must be provided by the user is the expected Full Width Half Maximum (FWHM) of the stellar profile, also tabulated in the JWST documentation. This value has a significant impact on both source detection and PSF fitting, and it should be selected based on the specific filter and observing mode. For

the short-wavelength channel, the FWHM is reported as 1.29 pixels for the F115W filter and 2.13 pixels for F200W.

These and the other fundamental required parameters were stored for each individual image in the corresponding *.opt* file. The structure of said file is the codeword for the parameters and the corresponding value to be used. The chosen values for the JWST dataset where:

- Readout Noise: values as previously described, depending on filter and readout pattern.
- Gain: values as previously described, depending on filter and readout pattern.
- High Good Datum or Saturation Threshold: this is the value above which the program will consider the pixel as defective. Having put all saturated pixels to 100,000 and knowing the theoretical saturation threshold depends on various conditions but is usually slightly above 60,000, this was set to 70,000.
- PSF Radius: the pixel scale radius inside which the PSF will be defined. This value needs to be fine tuned in order to well fit the broader profiles. The used value was 10.
- Varia parameter: defines the degree of the polynomial which describes how the PSF is allowed to vary throughout the image. This was set to 1, allowing for a linear variation of the PSF, as confirmed by dedicated tests.
- Analytic parameter: describes which type of analytic function is used to try and model the PSF. This was set to -6, an option which allows for all 6 of the available models to be employed in order to find the best fit. The models are later described in the PSF fitting process section.
- Threshold: it describes the significance level, in standard deviations, that the program will use to identify sources and distinguish them from random noise fluctuations. This was set to  $3\sigma$ .
- FWHM: values chosen as previously explained.
- Fitting Radius: it defines the radius of the circular area within which the profile fits will be calculated. This is a parameter that needed delicate fine tuning, since the optimal value often depends on the single image. It was usually kept between the 1 and 2 times the FWHM.

Once all parameters were set, iterative programs were implemented to execute the various steps of the analysis on all images, with adjustments depending on the image

type. Firstly, the two *DAOPHOT* routines "FIND" and "PHOTO" were run. The former identifies stellar sources in the image by scanning for local maxima in counts above the user-defined threshold, expressed in sigmas. It also uses the specified FWHM value to convolve the image and match detected sources with preliminary Gaussian profiles. This step includes an estimation of the local background to account for large scale variations caused by unresolved stars in dense stellar fields, such as the one considered in this work. The coordinates of the identified stars are saved in dedicated .coo files.

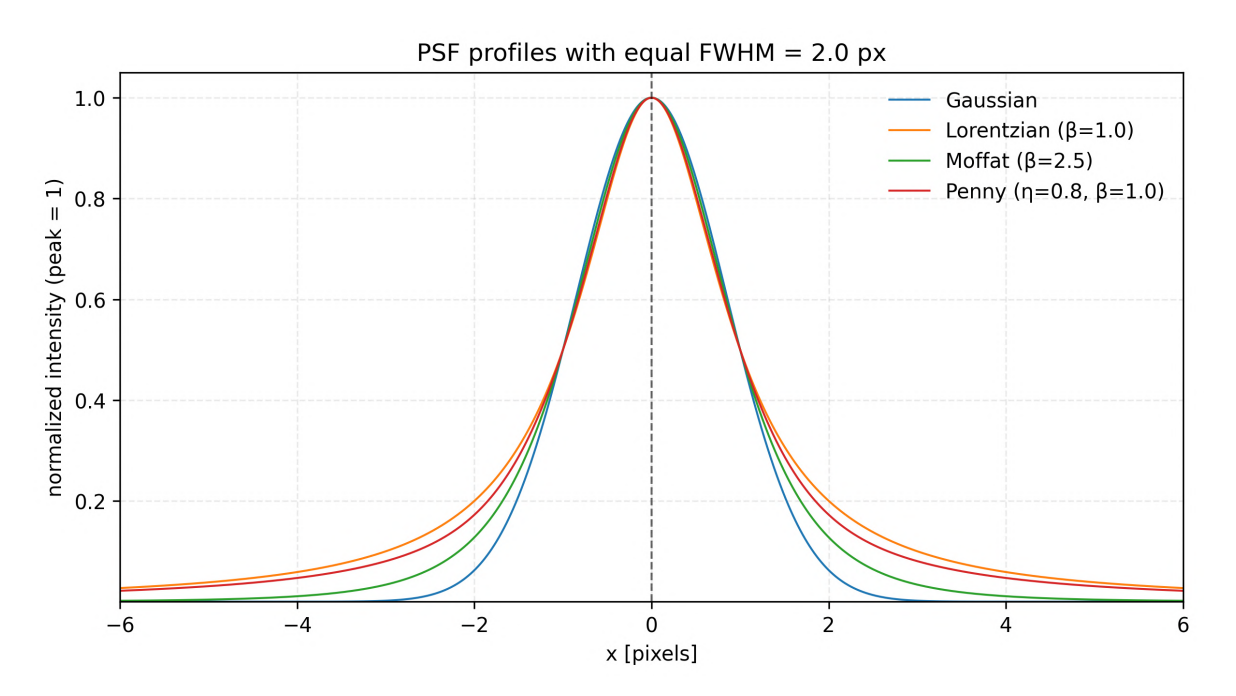


Figure 3.2: Examples of one-dimensional PSF profiles for Gaussian, Lorentzian, Moffat, and Penny models, all normalized to unit peak intensity and matched to have the same FWHM.

Aperture photometry is then performed through the routine specifically designed for this task ("PHOTO"), allowing for the preliminary estimation of magnitude values. This is done by measuring the flux within multiple circular apertures centered on each star, using the coordinates output by FIND. The local sky background is subtracted, estimated from an annular region around each star. The aperture radii are specified in the photo.opt file: in this analysis, apertures with radii ranging from 1 to 20 pixels were used, and the background annulus was set between 10 and 25 pixels. The results are saved in .ap files.

Having laid the groundwork for the PSF fitting routine, the best fit PSF was computed with the DAOPHOT "PSF" command. Bright, isolated, unsaturated stars well distributed across the image were selected to model the PSF.

The stellar PSF is modeled using a combination of analytic functions and empirical

residuals. The analytic functions available in DAOPHOT include: Elliptical Gaussian, Elliptical Moffat with  $\beta=1.5$ , Elliptical Moffat with  $\beta=2.5$ , Elliptical Lorentzian, 4-parameter Penny Function (sum of a Gaussian and Lorentzian), and a 5-parameter Penny Function.

For the analyzed JWST dataset, the optimal choice for the PSF model was the Penny function with image-specific corrections. These models were saved in the corresponding *.psf* files.

To obtain final magnitude estimates from PSF fitting, the *Allstar* routine was employed. This program takes as inputs the stellar positions and preliminary magnitudes derived from aperture photometry, and applies the PSF model to each source in order to refine both position and flux estimates. The fitting is performed iteratively: at each step, the model PSFs are subtracted from the image at the locations of the stars, progressively building a residual image. If the procedure is successful, the residual image should appear flat, with only minimal structure, mainly due to saturated stars, bad pixels, or imperfectly modeled sources that are excluded from the fitting. An example of the residual image is shown in Fig. 3.3. At the end of this process, the data containing refined positions and PSF magnitudes of each star is saved in *.als* files.

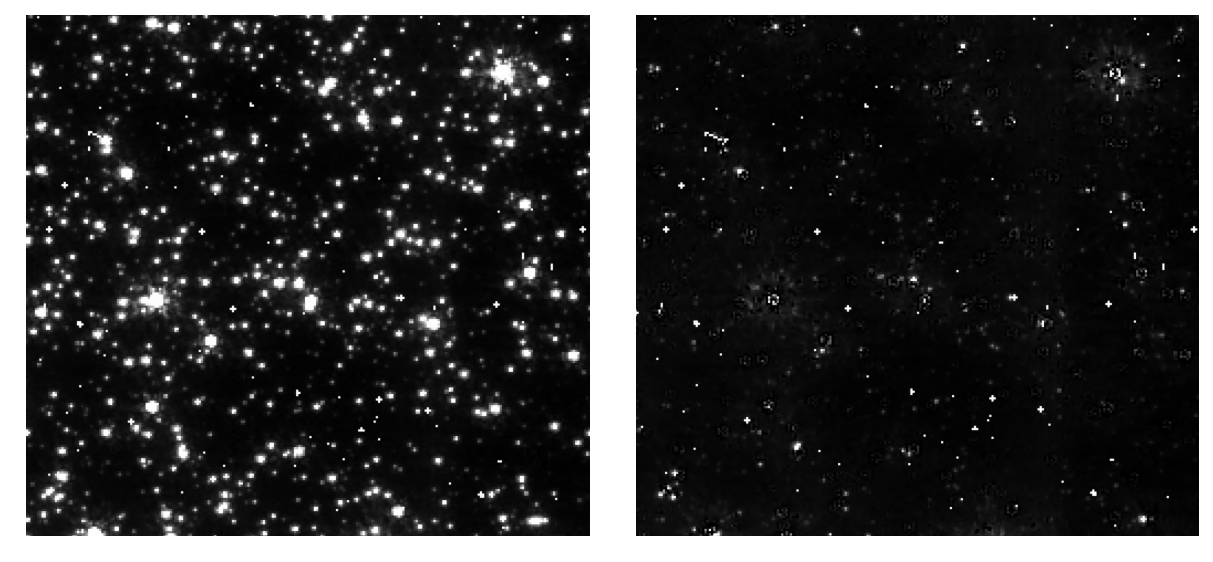


Figure 3.3: Example of a zoomed in region of a JWST F115W BRIGHT2 image (left panel) and the corresponding residual image (right panel) after the *Allstar* routine

The analysis can be further refined by combining multiple images. To this end, the *DAOMATCH* routine was used to determine the geometric transformations between images taken with different detectors, using the long-channel images as reference frames.

In cases where this alignment proved particularly challenging, such as when combining images from the first and second epochs, which were acquired with different rotation angles, a dedicated Fortran script was employed which exploited the matching of stellar triangles between the two images to derive a reliable transformation.

#### 3.2.2 HST dataset

For the HST dataset the same reduction methodology used for the JWST dataset was employed but with specific parameter adjustments to account for the different instrument characteristics, filters, and exposure times. The adopted parameters which required changes are listed below:

- Readout Noise: set to a reference value of 5 e<sup>-</sup>, based on ACS Instrument Handbook (2024).
- Gain: set to 1 e<sup>-</sup>/ADU, also from ACS Instrument Handbook (2024).
- High Good Datum (Saturation Threshold): set to 70,000 ADU, the typical saturation level for the ACS detector.
- FWHM: set to 2 pixels, based on HST user documentation.
- Fitting Radius: chosen relative to the FWHM, with values between 2.5 and 3.5 pixels depending on the specific image.

The reduction followed the same steps as for JWST: sources were detected, aperture photometry performed, the PSF modeled on reference stars, and refined positions and PSF magnitudes saved in .als files. For HST images, the best-fit analytical model was a Moffat function. As with JWST, transformations between dithered exposures and epochs were derived and saved in .mch files.

## 3.2.3 Combined catalogue

For the construction of the combined *DAOPHOT* catalogue, only JWST images obtained with the B chip from both visits were included. The A chip, covering the outermost regions of the system, was excluded from the joint analysis since it wasn't necessary for the scopes of this thesis.

Having as starting point the .als files for all JWST and HST frames, the full dataset was subdivided into several subsets based on filter and spatial coverage:

- F606W images of the central pointing across the three HST epochs (WFC1 for the first two epochs and WFC2 for the third);
- F814W images of the same central region;
- F606W images of the opposite peripheral regions across the three epochs (WFC2 for the first two epochs and WFC1 for the third);

- F814W images of the same outskirt regions;
- All F115W exposures from both JWST visits on the B chip;
- All F200W exposures from JWST, limited to the B chip.

The DAOMASTER routine, taking as input the previously generated .mch files, was run on each subset to generate individual masterlists. This process identifies common stars across images, refines coordinate transformations, filters out spurious detections (e.g., cosmic rays or detector artifacts) by requiring a minimum number of detections per star, and produces a masterlist in the reference frame of the first image. The minimum number of detections was set to 4 for all subsets, a value that effectively balanced the removal of spurious detections while preserving coverage, particularly in regions observed in fewer exposures due to dither patterns and multiple epochs. The main output consisted of .mag files listing the coordinates, IDs, and mean instrumental magnitudes with associated errors for each star, referred to the coordinate system of the first reference image and homogenized for exposure time and any detector-related systematic difference.

One of the most challenging aspects of this work was the derivation of accurate geometric transformations for the preliminary DAOPHOT catalogues of both JWST and HST images. In particular, the combination of the two datasets into a single, consistent reference frame required a careful and iterative procedure due to the different spatial resolutions, fields of view, and instrumental distortions of the two telescopes. To achieve precise alignment without losing homogeneity between the data, we used the programs DAOMATCH and DAOMASTER alternately in an iterative way, in order to progressively refine the transformations. This approach allowed us to improve the matches between the catalogs, ensuring that the coordinates of the sources were correctly transformed and comparable in the two frames. As reference frames, the first F115W exposure on the B1 chip for JWST and the first long F606W exposure on the WFC1 chip for HST were selected, both covering the central region of the system. This procedure resulted in defining very precise geometric transformations between the six sub-catalogues, properly saved in a .mch file.

A subsequent *DAOMASTER* run, with the constraint of retaining all stars, produced a global masterlist including all detected sources across filters, epochs, and instruments. Next, the *Allframe* routine was employed to improve PSF fitting, refining positions and fluxes using the global masterlist across all images, which enhances accuracy compared to frame-by-frame analysis. A crucial advantage of combining the two datasets lies in the ability to leverage information from different filters. For example, sources blended in optical images can often be resolved into two distinct stars in the higher-resolution JWST data, leading to improved measurements not only in

the combined catalogue but also in the individual filters. The updated magnitudes for each frame were saved in .alf files.

With the same logic as the .als files processing, .alf files were used to produce six distinct masterlists using DAOMASTER. For each image subset, both the .mag and .cor files were generated and saved. The .mag files are particularly important as they contain not only the measured magnitudes and associated errors but also essential DAOPHOT quality parameters such as  $\chi^2$  and sharpness, which are fundamental for assessing the reliability of the photometry. Furthermore, they contain the variability parameter, a ratio comparing external error (frame-to-frame scatter) to internal photometric errors, used to flag variable stars. The .cor files contain instead the matched star identifications across multiple images of the same field and will be crucial for future analysis.

Finally, a unique comprehensive masterlist was created based on a *.mch* file containing these sub-masterlists. This run of *DAOMASTER* produced a *.raw* file with mean magnitude values for each filter (F606W, F814W, F115W, and F200W) and, in the case of HST, chip. This preliminary catalogue is aligned to the ACS reference frame.

#### 3.2.4 Calibration

Up to this stage, magnitudes were simply instrumental, linked to the specific characteristics of each telescope and detector, and coordinates were expressed in detector pixel units (ACS WFC1 and NIRCam B1). To make these catalogues scientifically meaningful, both magnitudes and positions need to be converted to standard reference systems.

Since *DAOMASTER* homogenizes magnitudes to the first image in each subset, calibration was performed with respect to the six corresponding reference frames. The general calibration equation applied to convert the instrumental magnitudes to the Vegamag photometric system is:

$$m_{calibrated} = m_{instrumental} + ZP + corr_{ap} + corr_{EE} + 2.5 \log(t_{exp})$$
 (3.2)

Here, ZP is the filter-specific zeropoint (Tab. 3.2),  $corr_{ap}$  accounts for aperture correction, and  $corr_{EE}$  adjusts for encircled energy losses. Exposure times were 340 s for HST and 10.74 s for JWST reference frames. The term  $corr_{ap}$  was determined by selecting bright, isolated, unsaturated stars free from defective pixels within the PSF radius, computing the average difference between aperture and PSF magnitudes. The  $corr_{EE}$  factor corrects for flux falling outside the photometric aperture, with values from JWST Science Calibration Pipeline Team (2024) for JWST and Bohlin (2016) for HST.

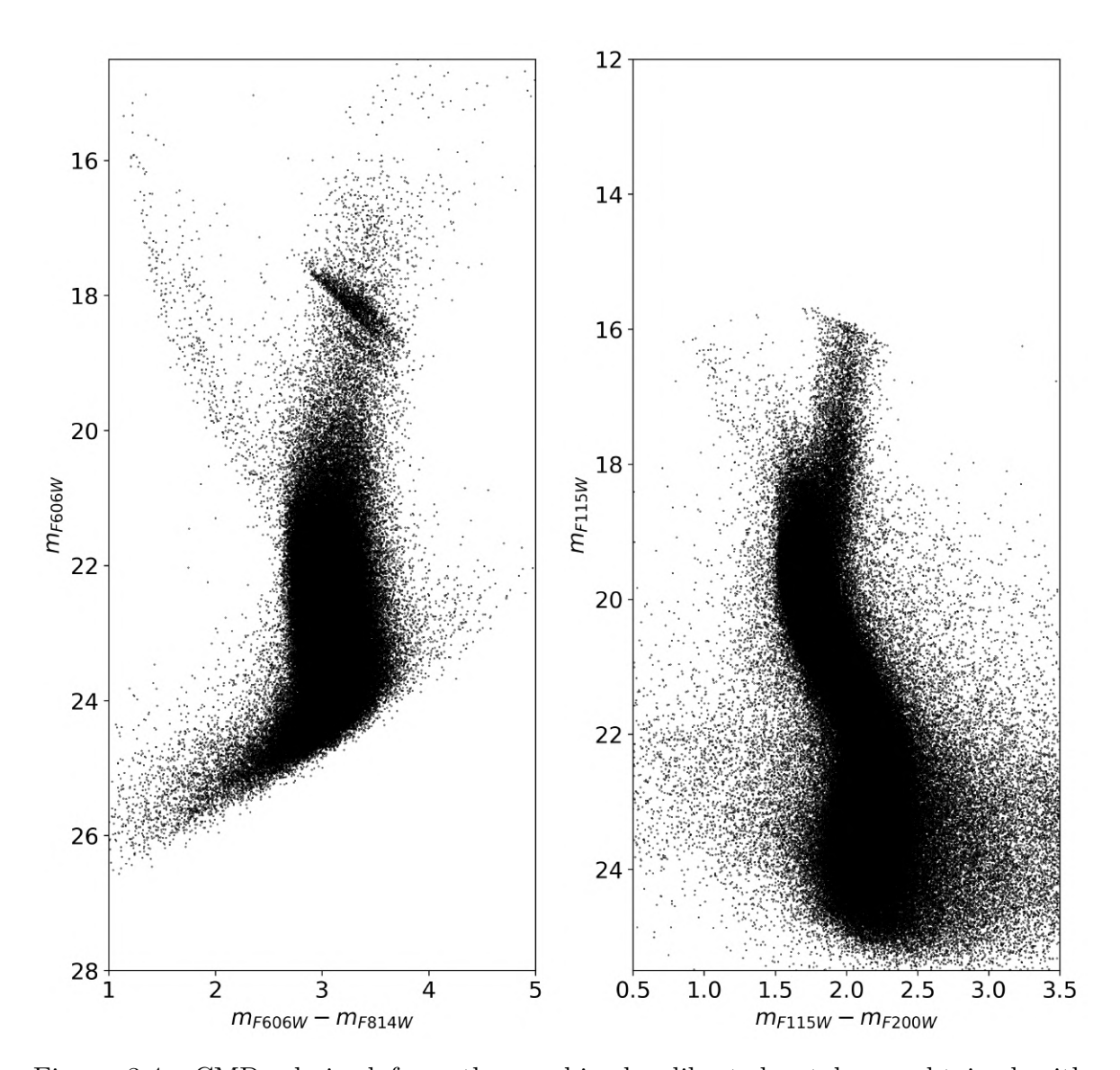


Figure 3.4: CMDs derived from the combined calibrated catalogue obtained with DAOPHOT. The left panel shows the optical CMD using HST ACS/WFC data in the F606W and F814W filters, while the right panel presents the near-infrared CMD using JWST observations in the F115W and F200W filters. In both cases some quality cuts were applied in order to select only reliable magnitude estimates. This bipanel visualization highlights the complementary wavelength coverage of optical and NIR data for stellar population analysis.

Filter	Detector	Zero Point
F200W	NIRCam B1	25.55
F115W	NIRCam B1	25.92
F814W	ACS WFC1/WFC2	25.521
F606W	ACS WFC1/WFC2	26.420

Table 3.2: Vegamag Zeropoint values for NIRCam and ACS recovered from the NIRCam documentation (STScI (2024b)) and the ACS Zeropoint Calculator (STScI (2024a)) respectively.

Once calibrated, the catalogue could be employed for a first generation of the CMDs associated to optical an NIR magnitudes. A comparison of these diagrams, appropriately selected on the basis of the quality parameters, is shown in Fig. 3.4. The comparison between the two panels emphasizes the complementary nature of the datasets and the significant advantage offered by the new NIR observations. JWST is in fact capable of resolving and providing accurate measurements of much fainter magnitudes along the MS, extending beyond the MS knee. Although stars at the horizontal branch level appear saturated (and are thus not shown since they are non-reliable magnitude estimates) in the NIR data, this issue was effectively mitigated by employing the *jwst1pass* photometric method (discussed in the next section).

In Fig. 3.5 a comprehensive view of all stars detected in the NIRCam B module FOV is shown with no quality cuts. This highlights the incredible capabilities of both the detector and photometric software: more than 300,000 stars were detected in this FOV alone. This is by far the deepest CMD ever observed for Terzan 5 since the previous one could reach just 1-2 mags below the MS-TO point corresponding to  $m_{\rm F115W} \sim 21$ . This newly obtained CMD is thus at least 4 magnitudes deeper than any previous result.

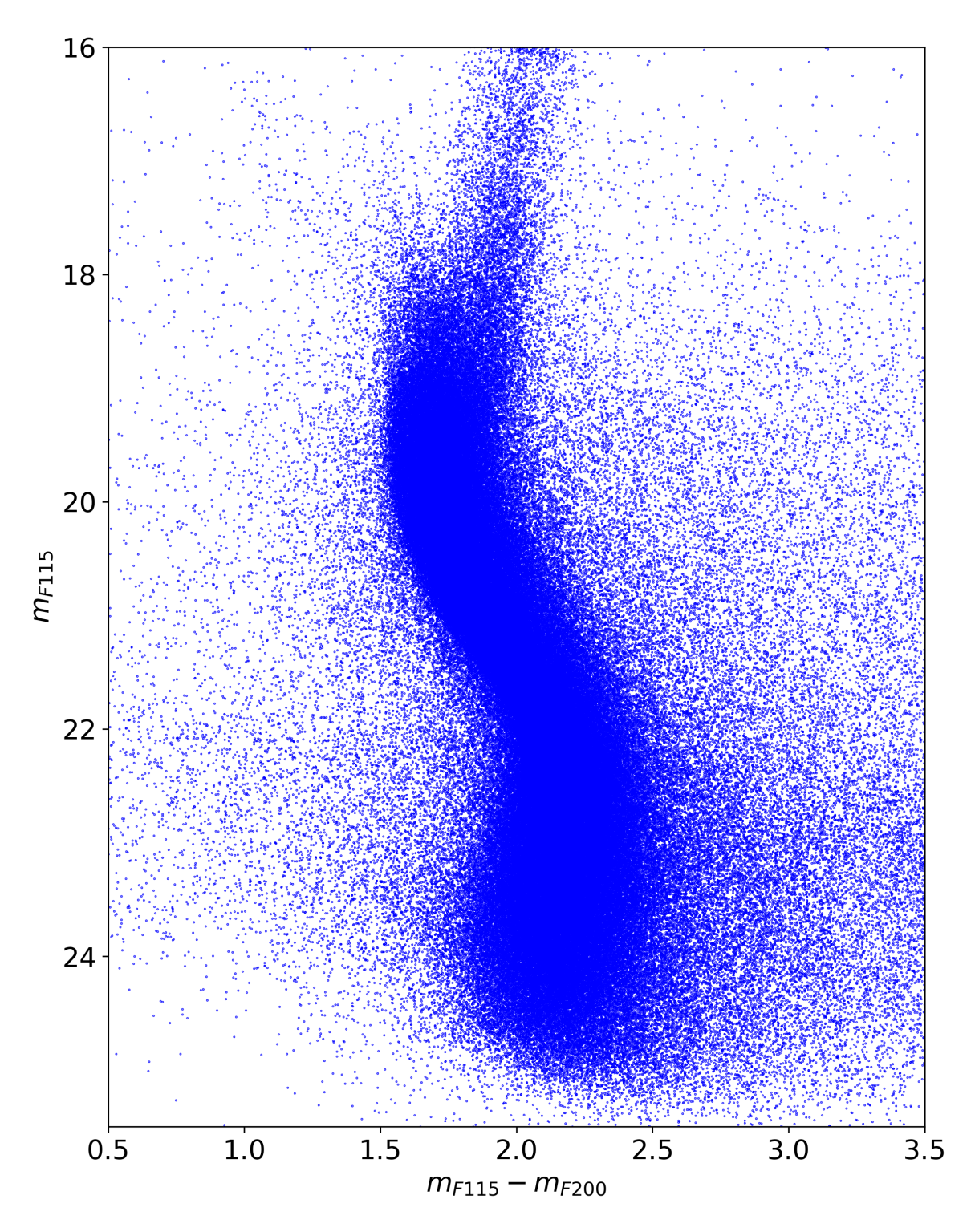


Figure 3.5: NIR CMD for Terzan 5 derived from the combined, calibrated catalogue obtained with DAOPHOT. All detected sources are shown, without applying any quality cuts, resulting in a sample of over 300,000 stars detected in the B module of NIRCam alone.

# 3.3 jwst1pass photometric reduction

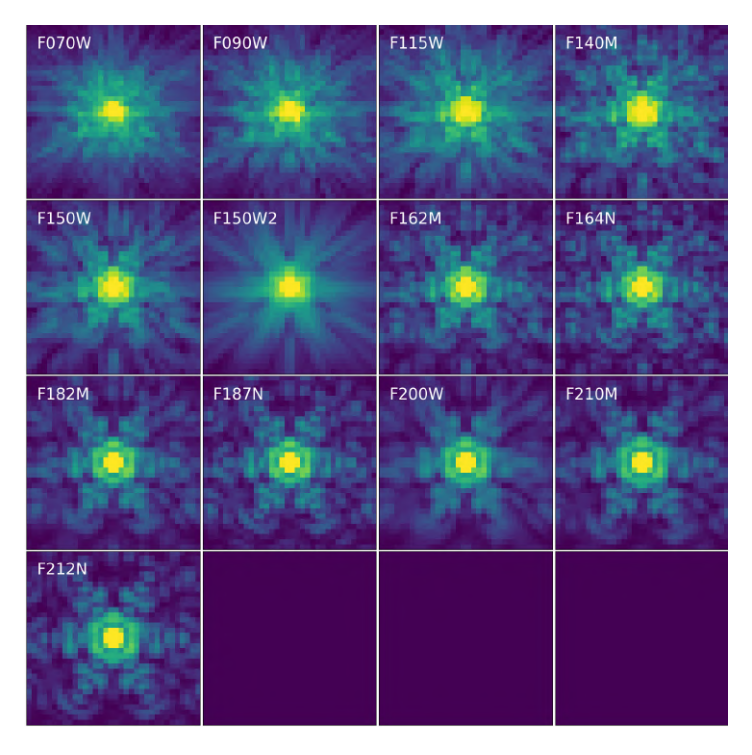


Figure 3.6: Simulated PSF models for short wavelength channels (NASA, JWST Near Infrared Camera )

The analysis was further complemented by employing the publicly available FOR-TRAN code *jwst1pass* (Libralato et al., 2023), with the aim of obtaining an independent yet comparable estimate of stellar magnitudes for the JWST dataset.

The various routines provided in the online repository enable PSF fitting using empirical point spread functions (ePSFs) specifically tailored for NIRCam, which proved particularly effective for bright sources, as it recovers positions and fluxes from the unsaturated wings of the PSF even when the core is saturated. This extends the dynamic range of the observations and mitigates saturation effects.

jwst1pass operates directly on the "cal" images, which are the outputs of the second stage of the JWST calibration pipeline. Unlike DAOPHOT, it processes data in DN/s, allowing independent photometric reductions of BRIGHT2 and RAPID exposures without the need to homogenize frames with different integration times. Additionally, geometric distortion corrections are applied directly to each image.

Starting from well-modeled empirical PSFs, the code computes correction coefficients at each run to further refine the model. Multiple dithered exposures corresponding to the same NIRCam detector were combined to improve the reliability of the magnitude estimates. These measurements were then placed on a common reference frame, adopting the B1 chip as reference, through the combined use of the xym2mat

and xym2bar routines. Up to this stage, magnitudes obtained from different NIRCam detectors were kept separate and calibrated independently.

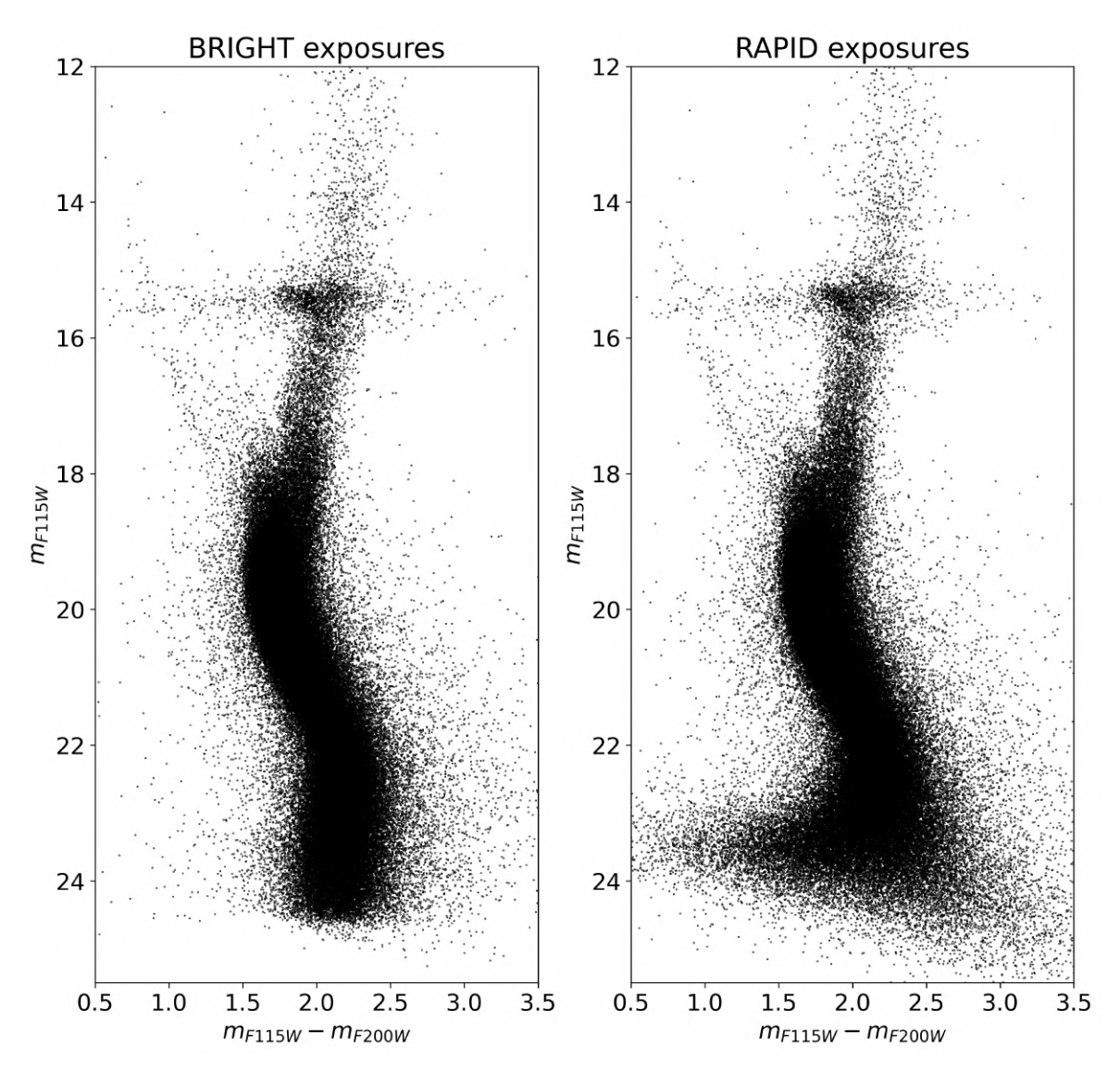


Figure 3.7:  $(J, J^{\sim}K)$  CMDs of Terzan 5 obtained with the jwst1pass magnitudes. The panels show magnitude values obtained from BRIGHT2 exposures (left) and RAPID ones (right). A clear improvement with respect to previous CMDs is observed for bright sources above the HB level, demonstrating the enhanced capability of the photometric method to accurately measure these luminous stars. This figure also highlights the crucial differences in the capabilities of the two readout patterns, especially at faint magnitude values. Although we would expect an improved photometry for bright sources in RAPID exposures, this is mitigated by the combined use of jwst1pass and the option to recover Frame 0 values.

#### 3.3.1 Calibration

For the *jwst1pass* dataset the calibration slightly differed from the previously described one, as magnitudes were derived from count rates and did not require exposure time correction. The calibrated magnitude was computed as:

$$m_{calibrated} = m_{instrumental} + ZP + corr_{ap} + corr_{EE}$$
 (3.3)

Magnitudes from different chips were calibrated separately and then averaged for common stars to produce a unified catalogue with F115W and F200W magnitudes. A comparison of the calibrated magnitudes with the corresponding stars in the *DAOPHOT* catalogue shows good agreement within the uncertainties, which strengthens the reliability of our calibration procedure. As a result, the two catalogues can be merged, since they are both referenced to the same photometric system. Figure 3.7 displays the CMDs derived from the calibrated catalogue. In terms of recovering bright sources, the improvement over previous plots is evident, as we are now able to clearly reach the horizontal branch level, demonstrating the enhanced photometric capabilities of this softwares at these magnitudes. However, the CMDs obtained with *DAOPHOT* reach approximately 1 magnitude fainter along the main sequence compared to this method, allowing for a deeper probing of the lower MS. Together, the two methods cover a broader magnitude range, with *DAOPHOT* excelling at faint sources and *jwst1pass* improving bright-star measurements.

# 3.4 Astrometry

The astrometric calibration was performed using Gaia DR3 data (Gaia Collaboration et al., 2016, 2023), selecting stars within 180 arcsec of the coordinate center of Terzan 5 to ensure a high-quality reference sample. The *DAOPHOT* catalogue, initially in ACS pixel coordinates, was matched to absolute RA-Dec coordinates using the CataXcorr software (Montegriffo et al., 1995), yielding a robust astrometric solution with typical residuals of less than 0.03" in both coordinates. A visualization of this match is shown in Fig. 3.8. This solution was then used as a reference to align the *jwst1pass* catalogue, ensuring consistency between the two datasets.

The resulting catalogue is fully calibrated both photometrically and astrometrically. It includes magnitudes in the Vegamag system for four filters (F115W, F200W, F606W, and F814W), with F115W and F200W estimates derived independently from both the *DAOPHOT* and *jwst1pass* reductions. The final produced catalogue provides a solid foundation for subsequent scientific analyses thanks to its multi-epoch nature, the inclusion of both optical and NIR data, and an unprecedented magnitude depth along

the main sequence.

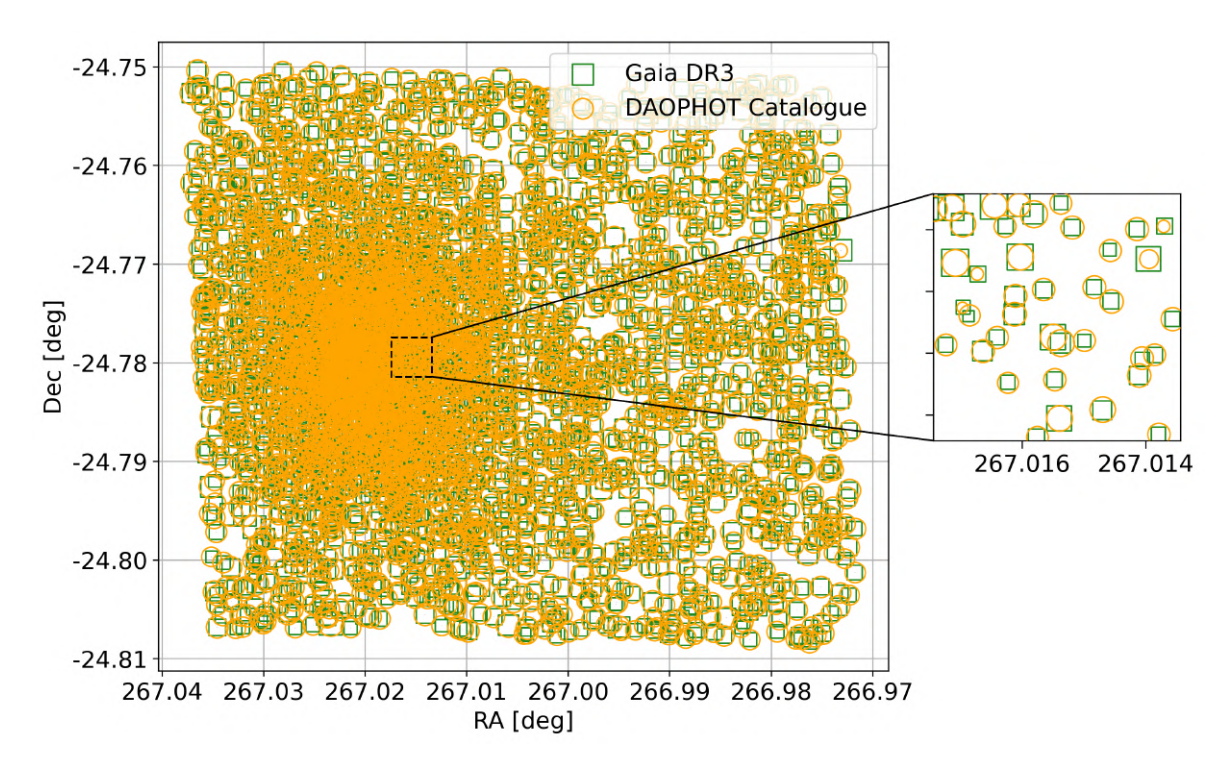


Figure 3.8: Positional comparison between sources identified in the *DAOPHOT* catalogue (orange circles) and those from the Gaia DR3 catalog (green squares) in Terzan 5. The markers' size is related to the magnitude in the G band for Gaia and F606W for the catalogue obtained in this work. The full field of view is shown in the main panel. A black dashed box highlights a magnified region, the detail of which is shown in the inset on the right. The inset, featuring a magnified and square aspect ratio, displays the same pairs of sources. This demonstrates the excellent positional agreement between the two catalogs.

# Chapter 4

# Proper motions and differential reddening

This chapter describes the computation of stellar proper motions and differential reddening corrections to the previously described catalogue of Terzan 5 stars. The ultimate goal of these procedures is determining cluster membership, accounting for spatial variations in extinction across the FOV, and constructing a final, corrected CMD.

# 4.1 Proper motions

Understanding the physical properties and structure of a stellar system requires accurately identifying which stars within the observed field are genuine members. One of the main challenges in studying resolved stellar populations in the Galactic bulge is the significant contamination from foreground field stars, which do not belong to the system. A key step toward overcoming this issue is the analysis of stellar proper motions, made possible in this study by the availability of multi-epoch observations.

Proper motions are defined as the apparent angular displacements of stars on the plane of the sky, perpendicular to the line of sight. Detecting these motions for typical resolved stellar populations generally requires a temporal baseline of at least a decade. In this work, the combination of early-epoch HST observations from 2003 with the most recent JWST data from April 2025 provides an exceptionally long baseline, enabling highly precise measurements.

Relative proper motion analysis offers an effective method to identify genuine Terzan 5 members since cluster stars are expected to share the same bulk motion, while foreground stars, being closer to the observer and characterized by a different kinematics, typically display larger and more dispersed apparent motions, possibly centered around a different mean value. By selecting the stars that draw a narrow distribution in the proper motion diagram, it is possible to isolate the population physically associated

with Terzan 5, effectively enabling a cleaner investigation of its structure, stellar content, and evolutionary history.

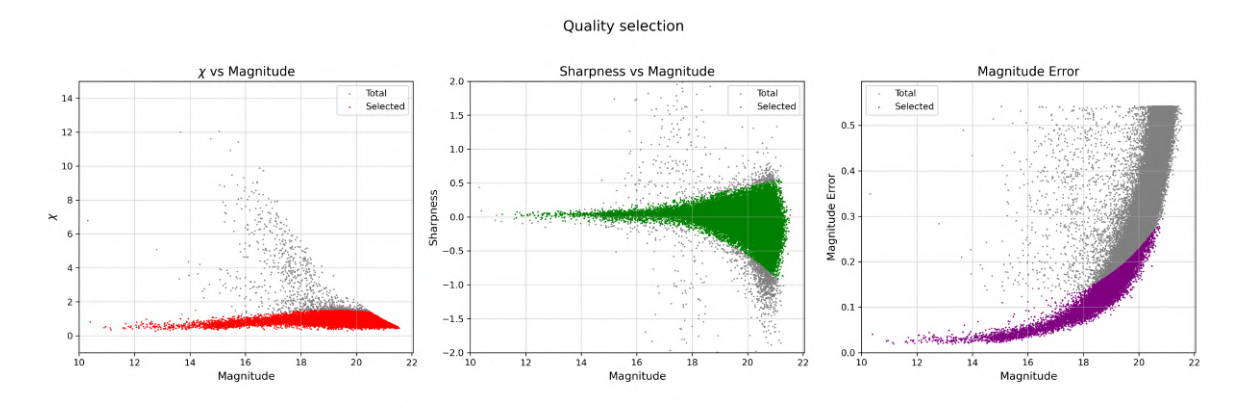


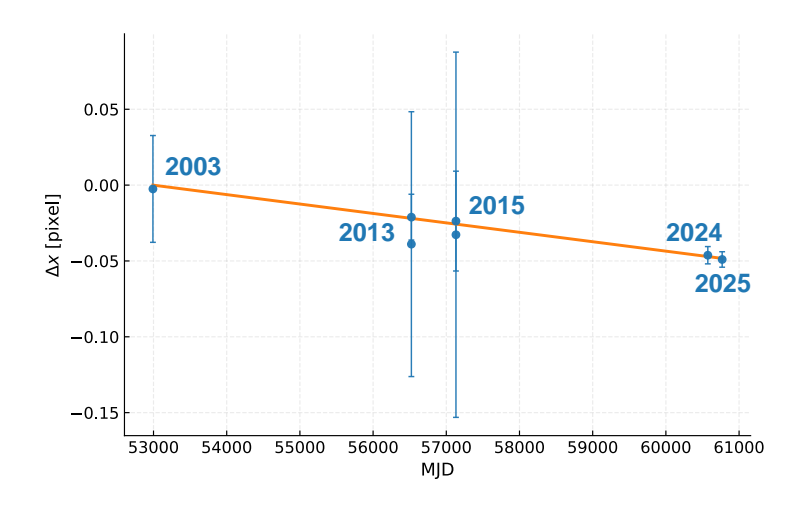
Figure 4.1: Example of quality selection on HST data. The left panel shows the adopted selection in the DAOPHOT parameter  $\chi^2$ , the central one is for the sharpness parameter, and the right panel is for the error on the magnitude.

The first step in determining proper motions is to accurately estimate the stellar centroid positions. One of the main outputs of a photometric PSF-fitting routine is the centroid of stars based on the peak positions of the modeled PSF functions. In the previously described photometric analysis, these are contained in *DAOPHOT* .alf files. All initial images in this format need first to be corrected for geometric distortions. For the JWST observations, this was achieved using the routine implemented by Griggio et al. (2023), which both corrects for distortions and transforms all coordinates to a common reference system. In the case of HST we used a dedicated Fortran routine, correcting the distortions and bringing the coordinate arrays, which are specific to each detector, into a unified instrumental reference frame.

The list of files was then grouped by epoch and filter, and each subgroup was aligned to a reference image using CataXcorr. From each file, the relevant information was retained, namely coordinates, magnitude, magnitude error,  $\chi^2$ , and sharpness, which are the main quality parameters associated by DAOPHOT to each detection.

An initial quality selection was applied to each image based on  $\chi^2$ , sharpness, and photometric error, with the goal of retaining only well-measured stars for accurate position and proper motion estimates. This selection was performed by examining each parameter as a function of magnitude. Specifically, the data were divided into magnitude bins, and within each bin, the mean and standard deviation of the parameter were calculated. A sigma-clipping procedure was then applied, followed by spline interpolation across the bins, to define a valid range of acceptable values at each magnitude. An example of this selection process is shown in Fig. 4.1. Stars that satisfied these criteria were flagged as valid, and only their detections were used to compute the average x and y positions, the corresponding standard deviations (which represent the positional

uncertainties), and the number of images contributing to each measurement.



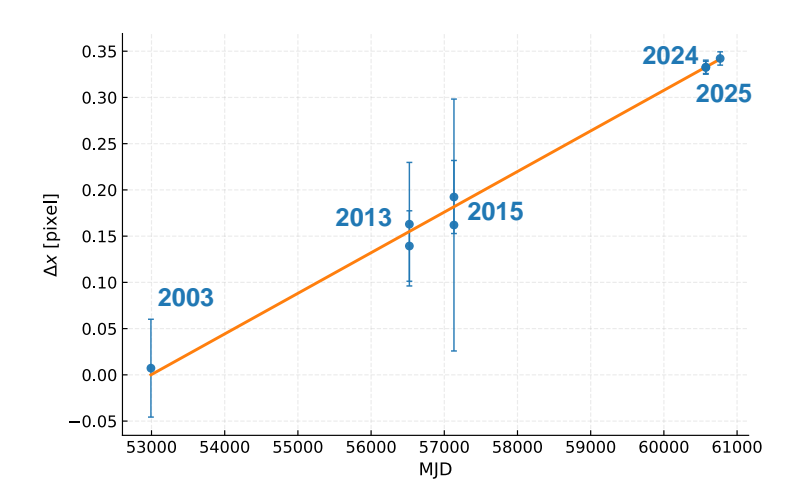


Figure 4.2: Example of the two linear fits of the measured stellar positions as a function of time (expressed as MJD) for two of the selected stars with five available epochs (2003, 2013, 2015, 2024 and 2025). On the y axis the variation in the x coordinate with respect to the initial reference position is plotted. The blue circles with error bars indicate the measured x-coordinate in the reference frame of ACS's WFC1 at each epoch, while the solid orange line shows the weighted linear regression best-fit line, whose slope is the computed proper motion in pixel/MJD. The labels indicate the observation epoch.

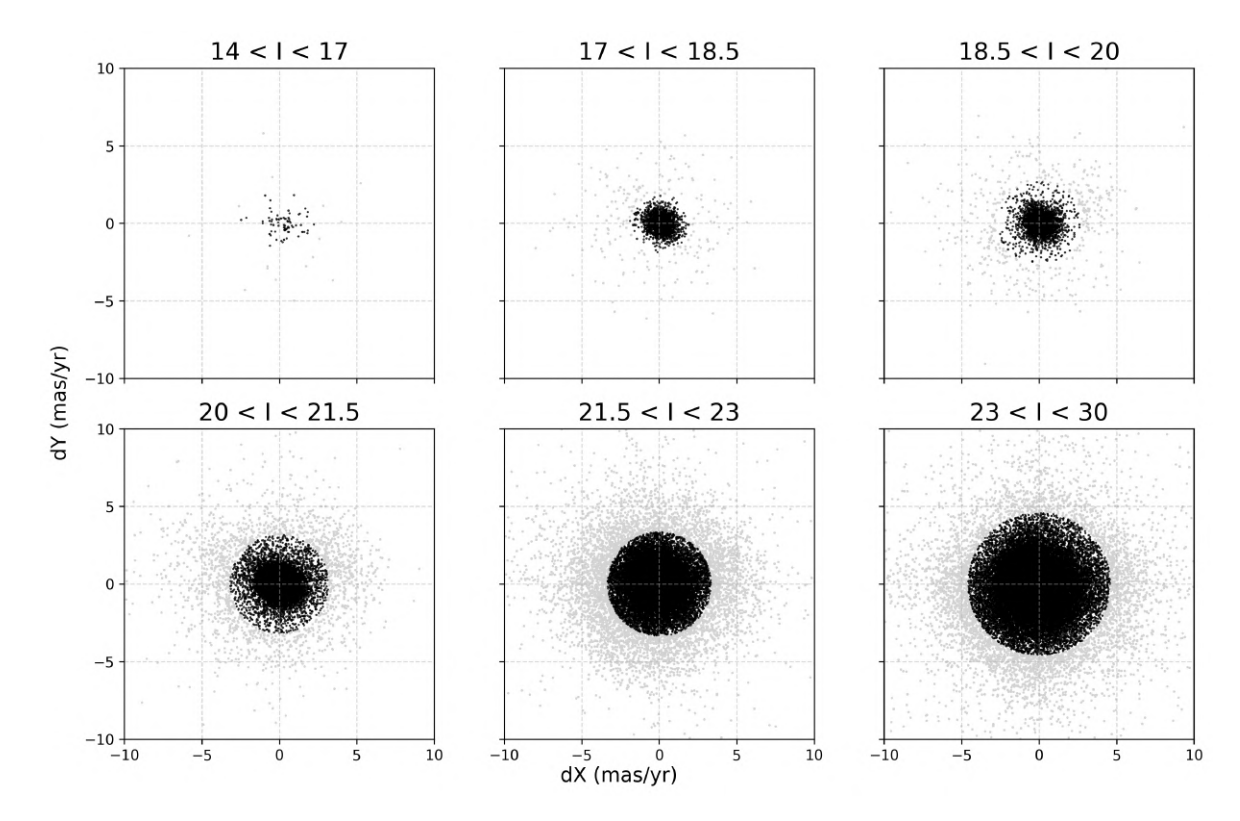


Figure 4.3: Vector Point Diagram (VPD) showing the computed proper motions in different F814W (here noted as I) magnitude bins, as marked in the top-label of each panel. The black dots correspond to the selected member stars, while the grey dots are those considered as Galactic field interlopers.

In cases where two valid position measurements, obtained from different filters, were available for the same epoch, their average was adopted. Otherwise, the single available measurement was used.

Once the mean stellar positions in relative detector coordinates were obtained for each subset (epoch, filter), they were matched and transformed into a common reference frame, chosen as the first-epoch ACS/WFC1 image. The alignment was performed with CataXcorr in two steps: first, a transformation limited to first-order terms was applied to establish a robust initial match among the catalogs; then, higher-order polynomial terms were introduced to refine the transformation and increase the number of matched stars.

Proper motions were then determined by performing a weighted linear fit of the positions as a function of time, using the Modified Julian Dates (MJD) corresponding to the different observations epochs. This was done separately in the x and y directions. The fit was weighted according to the positional uncertainties, and was computed only for stars with at least two valid positional measurements across the available epochs. An illustration of the fitting procedure in cases of baselines of more than 20 yr is shown in Fig. 4.2. These values for proper motions and relative errors were associated to the

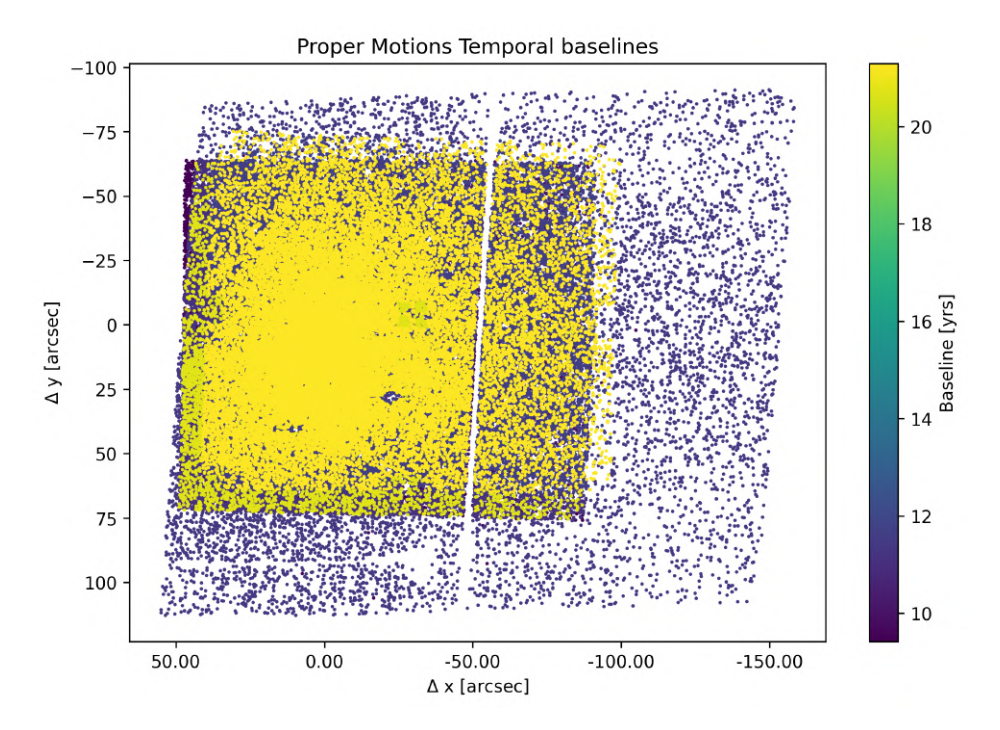


Figure 4.4: Map of stars with computed proper motions, colored by the corresponding temporal baseline (see the adopted color code in the side bar). The coordinates are relative to the system's center and are expressed in arcseconds.

corresponding stars in the main catalogue.

For a robust selection of cluster members, we retained only the values computed from temporal baselines exceeded 3 years (see the map of the available temporal baselines in Fig. 4.4), because those obtained with only two epochs close in time (i.e., the two JWST visits) are susceptible to large positional uncertainties. They were then converted to the commonly used units of mas/yr by adopting the appropriate pixel scale.

To identify the likely cluster members, we divided the stars into magnitude bins in the F814W filter (I) and considered their total proper motion, defined as  $\mu = \sqrt{(\mu_x^2 + \mu_y^2)}$ . Given the relative nature of the proper motion measurements, the distribution of  $\mu$  is expected to be centered around zero for cluster members. In each magnitude bin, a sigma-clipping procedure was applied on  $\mu$  to reject outliers and retain only stars consistent with the cluster motion. This selection was performed using an iterative clipping algorithm, which excludes stars with  $\mu$  exceeding a given threshold (set as a multiple of the standard deviation), until convergence is reached or a maximum number of iterations is performed. The result of this selection is plotted in Fig. 4.3, which shows the Vector Point Diagrams (VPDs, where each data-point corresponds to the star's position in proper motion space) for the adopted magnitude bins.

Figure 4.5 shows the effect of the proper motion selection on the CMD. As apparent,

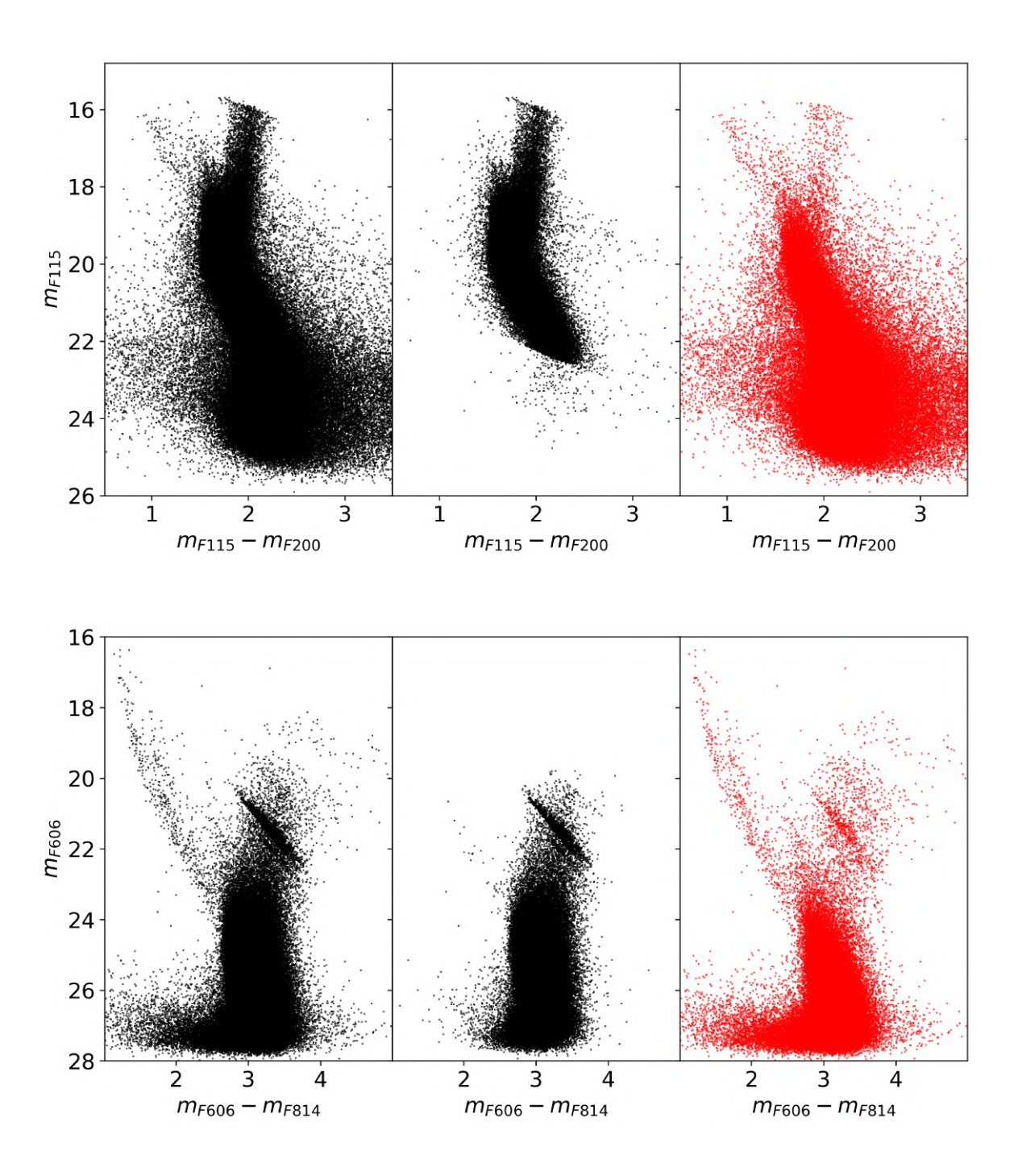


Figure 4.5: Effect of proper motion-based membership selection on the JWST (top) and HST (bottom) CMDs. The left panels show all the detected stars, the central panels display stars selected as likely members of Terzan 5, and the right panels highlight stars that either have no valid proper motion measurements, or are identified as likely non-members based on the proper motion selection.

the stellar evolutionary sequences are better defined in the CMDs of the selected members, the proper motion cleaning is very effective in identifying as field interlopers the stars that draw the long diagonal sequence in the blue and bright part of the observed CMDs, while some residual stars genuinely belonging to Terzan 5 populate the CMDs plotted in the left-panels because they have no accurate proper motion measure. It is important to note that the apparent cutoff of the MS faint-end in the NIR selection is due to lack of correspondingly faint HST data providing the temporal baseline needed for the computation of proper motions. While this may pose challenges for future studies of the fainter main sequence, it is negligible for the current analysis, which requires proper motion measurements for stars around the main sequence MS-TO region.

# 4.2 Differential reddening

#### 4.2.1 Extinction and reddening

When analyzing photometric images or any astrophysical dataset, it is essential to account for the effects of the interstellar medium (ISM). This consideration is particularly crucial when studying lines of sight toward the Galactic Bulge, where the influence of the ISM is especially significant. Terzan 5 lies within the inner 1–2 kpc of the Bulge, in a region that is heavily affected by the presence of gas and dust, which alter the observed light through two related phenomena: extinction and reddening. Extinction refers to the overall dimming of light due to absorption and scattering by dust grains along the line of sight. Reddening, on the other hand, describes the wavelength-dependent nature of this effect: shorter, bluer wavelengths are more strongly attenuated than longer, redder ones. This differential absorption leads to the characteristic "reddening" of observed sources.

Analytically, these processes are described by the equations of radiative transfer. Let  $I_{\lambda}$  be the radiation intensity at wavelength  $\lambda$ . Considering an infinitesimal path length ds through the ISM, the change in intensity due to absorption is given by:

$$\frac{dI_{\lambda}}{ds} = -\alpha_{\lambda}I_{\lambda},\tag{4.1}$$

where  $\alpha_{\lambda}$  is the absorption coefficient at wavelength  $\lambda$ . Introducing the optical depth  $\tau_{\lambda}$ , defined as:

$$d\tau_{\lambda} = \alpha_{\lambda} \, ds,\tag{4.2}$$

and integrating along the line of sight, the solution to the differential equation yields the exponential attenuation law:

$$I_{\lambda} = I_{\lambda,0} e^{-\tau_{\lambda}}, \tag{4.3}$$

where  $I_{\lambda,0}$  is the unattenuated (intrinsic) intensity. Although the full radiative transfer framework includes additional effects such as scattering and re-emission by heated dust grains, in the optical and NIR regimes, absorption by interstellar dust is typically the dominant process. For this reason, in this work we focus on absorption-driven extinction and reddening, where the observed magnitudes  $m_{\lambda}$  relate to the intrinsic ones  $m_{\lambda,0}$  via:

$$m_{\lambda} = m_{\lambda,0} + A_{\lambda},\tag{4.4}$$

with  $A_{\lambda}$  being defined as:

$$A_{\lambda} = -2.5 \log_{10} \left( \frac{I_{\lambda}}{I_{\lambda,0}} \right) \simeq 1.086 \, \tau_{\lambda}.$$
 (4.5)

As a general trend,  $A_{\lambda}$  increases for decreasing wavelengths, leading to the reddening of astrophysical sources. However, the precise shape of the extinction curve varies depending on dust grain properties, such as composition, size distribution, and geometry, which remain only partially understood and can differ significantly along different lines of sight. A widely adopted parametrization of the extinction law in the Milky Way is provided by Cardelli et al. (1989). First, we define the color excess E(B-V) as:

$$E(B-V) = A_B - A_V, (4.6)$$

where  $A_B$  and  $A_V$  are the extinctions in the respective filters. This parameter quantifies the degree of reddening due to the filter-dependent nature of extinction. The empirical model proposed by Cardelli et al. (1989) describes the extinction law as:

$$\frac{A_{\lambda}}{A_{V}} = a(x) + \frac{b(x)}{R_{V}},\tag{4.7}$$

where a(x) and b(x) are empirically determined functions of  $x = 1/\lambda$  (in  $\mu m^{-1}$ ), and

$$R_V = \frac{A_V}{E(B-V)} \tag{4.8}$$

is the extinction ratio, the sole free parameter of the model. The canonical value of  $R_V$  for the diffuse ISM in the Milky Way is approximately 3.1. Since  $R_V$  is sensitive to the size and composition of dust grains, variations in these properties lead to changes in the slope of the extinction curve. The behavior of the extinction law as a function of this parameter, as described by Li et al. (2007), is shown in Fig. 4.6. The average value of 3.1 may not accurately describe the extinction toward the Galactic Bulge, where the dust grain population may differ significantly.

Several recent studies suggest that a lower value, around  $R_V = 2.5$ , provides a

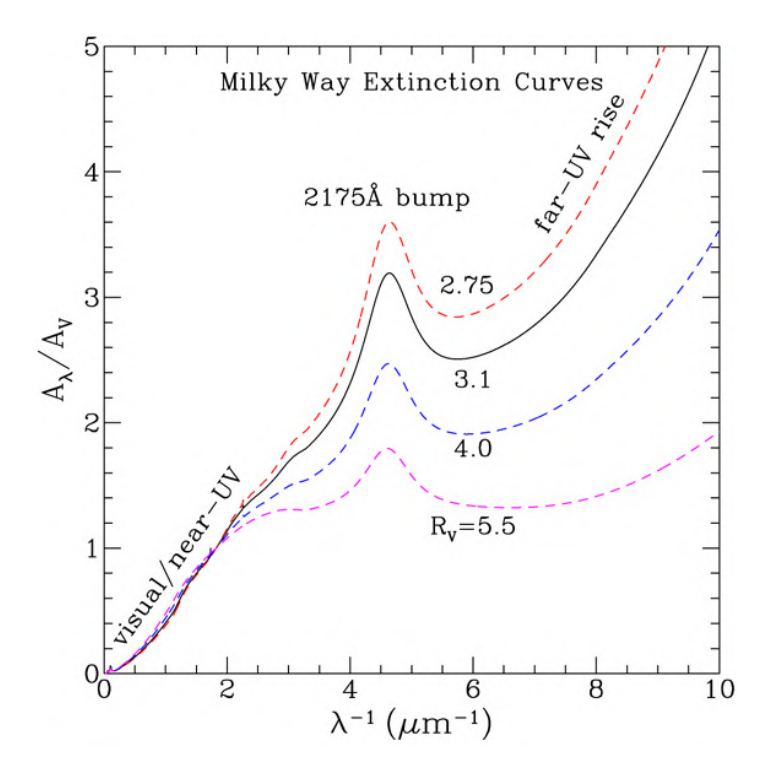


Figure 4.6: Extinction law for different values of  $R_V$ , from Li et al. (2007).

better description in this direction (e.g., Pallanca et al., 2021; Nataf et al., 2013). More generally, for any wavelength  $\lambda$ , the parameter:

$$R_{\lambda} = R_{V} \frac{A_{\lambda}}{A_{V}} = \frac{A_{\lambda}}{E(B - V)} \tag{4.9}$$

can be used to quantify the extinction in specific bands. In this work, we adopt  $R_V = 2.5$ , consistent with previous studies and supported by isochrone fitting in various color-magnitude planes (see the following section). This choice leads to the following values of the extinction coefficients:

$$R_V = 2.297,$$
  
 $R_I = 1.433,$   
 $R_J = 0.732,$   
 $R_K = 0.305,$ 

where V and I correspond to the HST filters F606W and F814W, respectively, while J and K refer to the NIRCam filters F115W and F200W. The extinction in each of these bands is obtained by multiplying these values by the color excess E(B-V) associated with the line of sight.

#### 4.2.2 Differential reddening correction

In a CMD, extinction shifts stars toward fainter magnitudes and redder colors, producing a diagonal displacement along the reddening vector. In the Bulge, this effect varies across the field due to patchy dust distribution and clouds with different column density. The overall phenomenon is known as differential reddening, leading to a broadening of the sequences along the reddening vector and complications in precise stellar population analysis. Correcting for these spatial variations in E(B-V) is therefore essential.

The differential reddening correction procedure adopted in this work is an adapted version of the method described in Pallanca et al. (2021). The first step of the routine involves identifying and tracing the Mean Ridge Line (MRL), which represents the average locus of stars along the evolutionary sequence in the CMD. This is achieved by selecting reliable member stars, based on proper motion analysis and photometric quality cuts, and restricting the sample to stars located along the MS, SGB, and RGB, below the HB. The MRL is derived by computing average colors and magnitudes within defined magnitude bins, establishing a reference sequence representative of the intrinsic stellar population. This sequence serves as a baseline for quantifying differential reddening effects on a star-by-star basis, allowing for spatially resolved corrections. The MRLs adopted in the optical and NIR CMDs are shown in Figure 4.7.

Once the MRL has been defined, the actual differential reddening correction is performed. For each star, a local set of nearby reference stars, selected within a fixed angular radius and meeting the same membership and quality criteria, is identified. This local sample is used to evaluate reddening variations by comparing the observed CMD positions of the reference stars against the MRL. A grid of trial  $\delta E(B-V)$  values, with a 0.1 step, spanning a defined range, is applied to the colors and magnitudes of the reference stars. For each trial value, a distance quantifying the deviation from the MRL is computed. The optimal reddening correction corresponds to the value of  $\delta E(B-V)$  that minimizes this distance, thus providing the best local adjustment to align the sequence of the selected stars with the intrinsic stellar sequence. This process relies on an extinction law (here with  $R_V = 2.5$ ) to convert trial color excess values into corresponding magnitude shifts in each filter.

The algorithm outputs individual differential reddening values  $\delta E(B-V)$ , along with associated quality indicators (such as the number of nearby stars used and the computed distance metric). Spatial coordinates relative to the field center are also calculated, enabling the construction of two-dimensional reddening maps that illustrate the spatial distribution of differential extinction across the field. This correction was calculated and applied in both the optical and NIR planes. The resulting high-resolution reddening maps are shown in Figures 4.8 and 4.9. Overall, we observe a

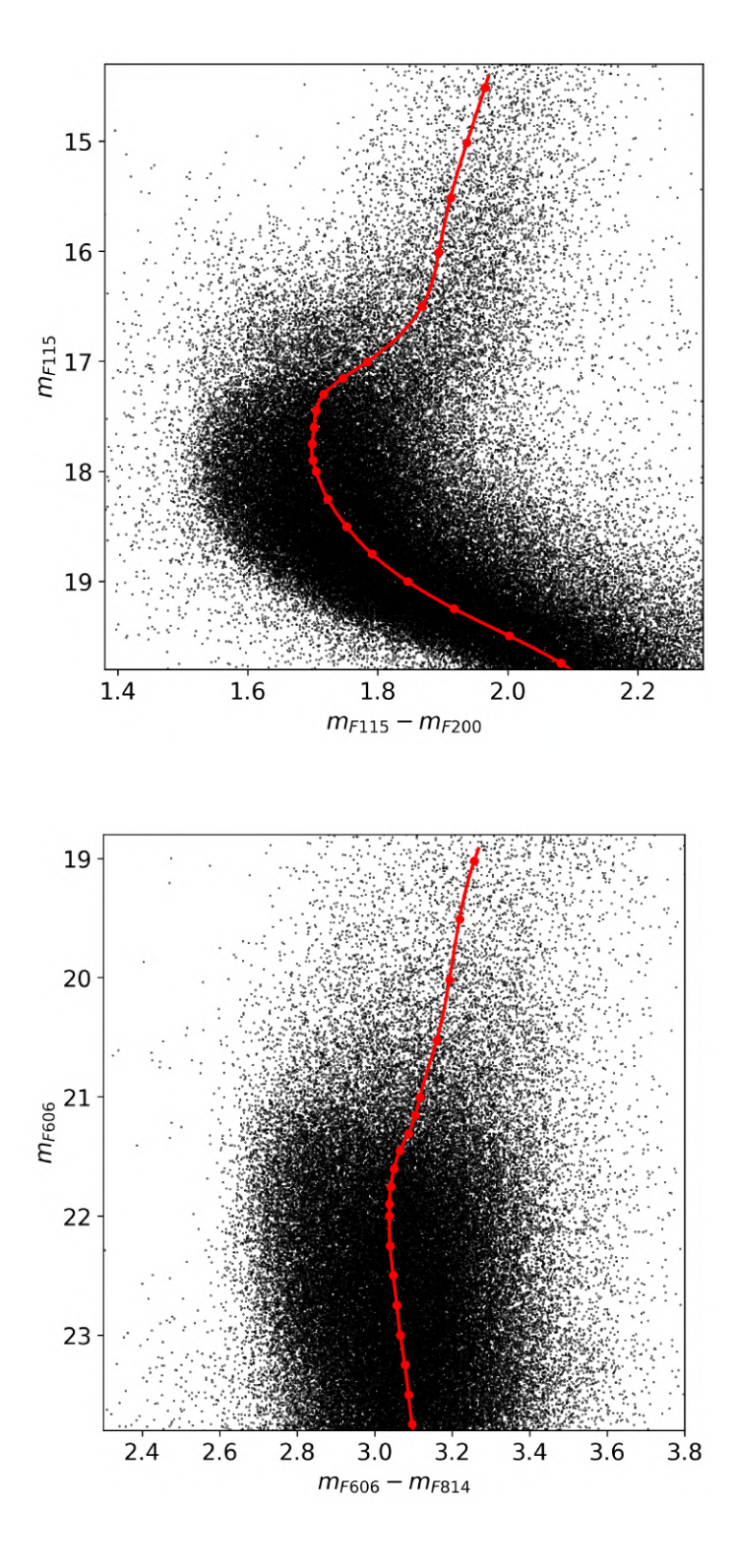


Figure 4.7: CMDs of the proper-motion-selected member stars in the NIR (top) and optical (bottom) planes. The red lines are the interpolated MRLs.

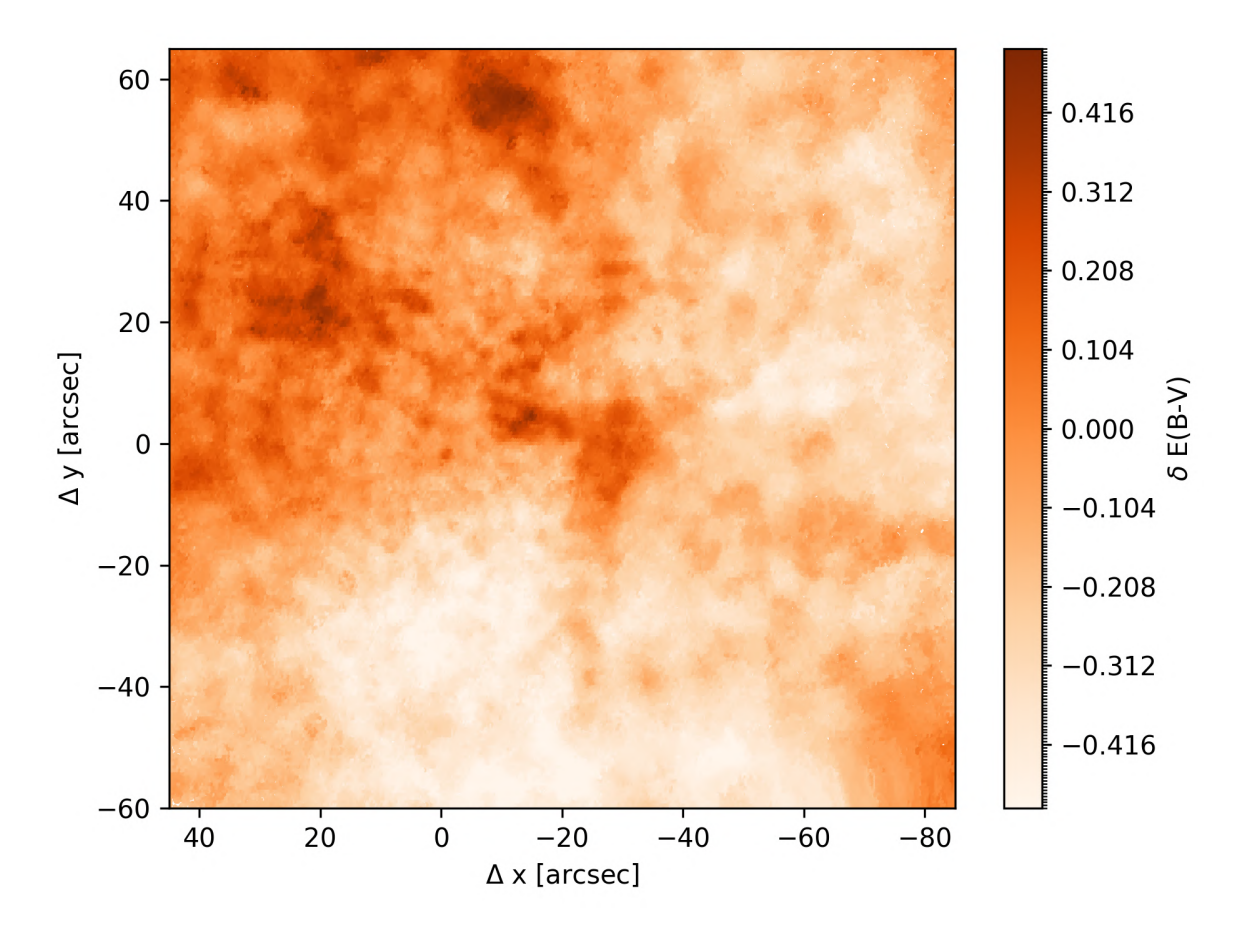


Figure 4.8: Map of differential reddening  $\delta E(B-V)$  across the JWST NIRCam field of view, derived from the (F115W, F115W–F200W) CMD. The coordinates  $\Delta x$  and  $\Delta y$  (in arcseconds) represent the angular offsets relative to the system's center. The color scale indicates spatial variations in the color excess, revealing the patchy and non-uniform interstellar dust distribution causing differential extinction effects within the field.

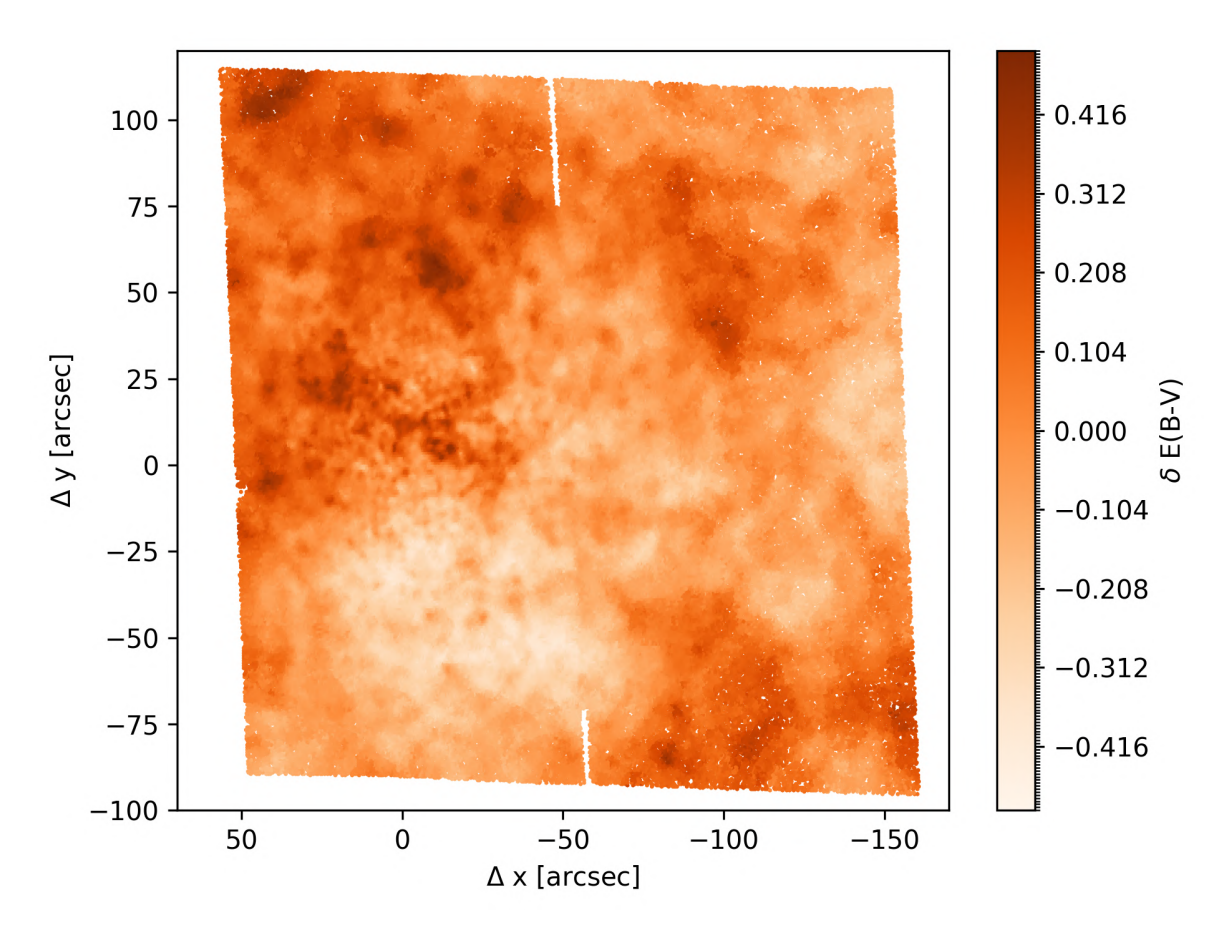


Figure 4.9: As in Fig. 4.8, but for the HST ACS field of view, and as derived from the (F606W, F606W–F814W) CMD. A good agreement with the differential reddening map derived from the NIR plane in the same FOV is apparent.

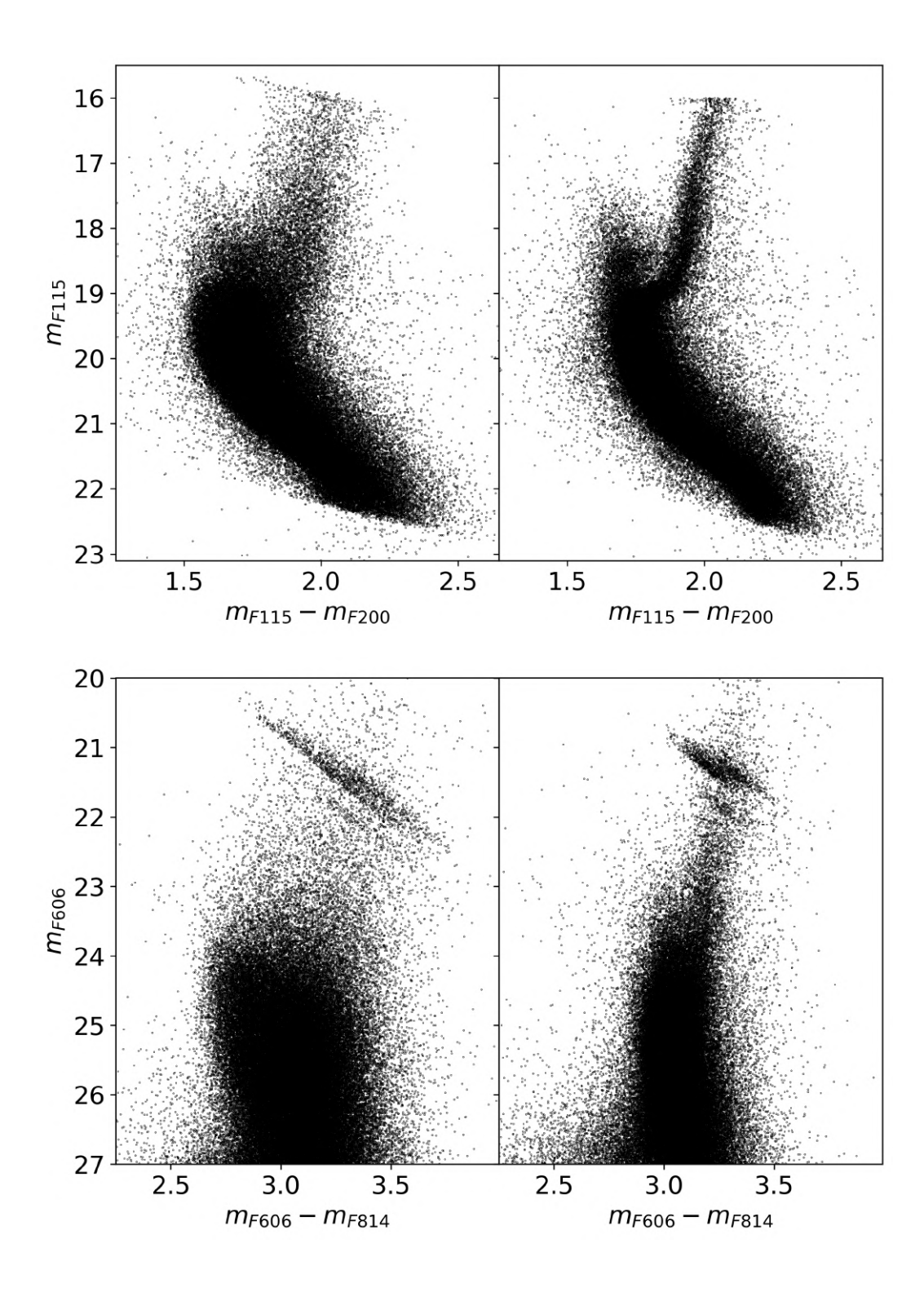


Figure 4.10: Effect of the differential reddening correction the JWST near-infrared (top panels) and the HST optical (bottom panels) CMDs. In both cases, stars have been identified as likely members through proper motion analysis and satisfy strict photometric-quality criteria. The correction significantly reduces color broadening and reveals tighter evolutionary sequences. As expected, the optical CMD is more strongly affected by spatially variable extinction.

maximum reddening variation of  $\sim 0.8$  magnitudes across the FOV, with  $\delta E(B-V)$  varying from  $\sim -0.4$  to  $\sim +0.4$ . The differential reddening correction is applied to the observed magnitudes of each star according to the following formula:

$$m_{\lambda,\text{corr}} = m_{\lambda} - R_{\lambda} \, \delta E(B - V).$$
 (4.10)

The CMDs before and after the differential reddening correction are presented in Figure 4.10. Both CMDs display the stellar sample selected based on proper motion membership and photometric quality cuts. The post-correction CMDs demonstrate tightened stellar sequences and reduced color dispersion. This comparison highlights the effectiveness of the correction procedure in recovering the intrinsic characteristics of the stellar population.

#### 4.3 Final corrected CMD

We present the final  $(m_{F115W}, m_{F115W} - m_{F200W})$  CMD for the stars selected as likely members of the system based on proper motion analysis, and corrected for differential reddening in Fig. 4.11. The magnitudes are primarily taken from the DAOPHOT photometric catalog; however, in cases where the DAOPHOT measurements reach saturation and become unreliable, we adopt jwst1pass magnitudes to recover the horizontal branch.

The CMD reveals the presence of an old, metal-poor population, with typical GC-like features. In addition, the clearly visible second main-sequence turn-off, with its characteristic hook-like morphology, suggests the presence of a prominent younger population. This feature, further emphasized by the coexistence of two distinct horizontal branches, highlights the complex star formation history of the system, which will be further constrained through detailed isochrone fitting in the following sections.

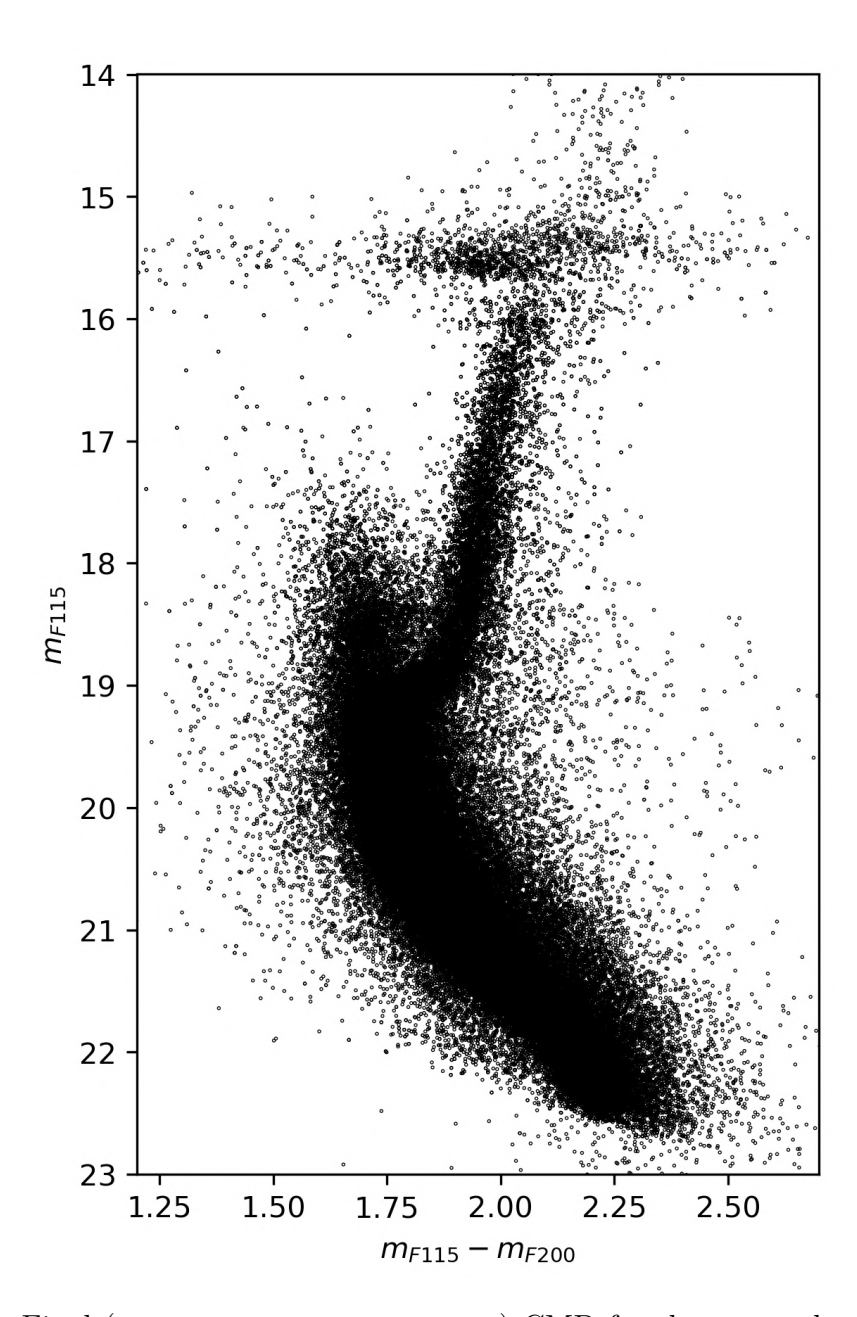


Figure 4.11: Final  $(m_{F115W}, m_{F115W} - m_{F200W})$  CMD for the stars selected as likely members of the system based on proper motion analysis and corrected for differential reddening. The magnitudes are primarily from the DAOPHOT photometric catalog, with jwst1pass measurements adopted in the regime where DAOPHOT photometry becomes saturated.

# Chapter 5

## Results

This chapter aims to provide a robust age estimate for the two main stellar populations in Terzan 5, making use of the proper motion selected and differential reddening corrected CMD obtained in the previous sections. The age determination is performed through isochrone fitting. In particular, we focus on the MS-TO, which is the most sensitive age indicator.

### 5.1 Distance modulus and color excess

In order to reach the final goal of age determination, the first parameters to be estimated are the distance modulus and the color excess. The distance modulus  $\mu_0$  is defined as follows:

$$\mu_0 = (m - M)_0 = 5\log_{10}(d) - 5 \tag{5.1}$$

where m is the apparent magnitude, M is the intrinsic magnitude and d is the distance in parsecs. The subscript "0" indicates that this is the intrinsic distance modulus, which does not account for extinction.  $\mu_0$  is a measure of the decrease in brightness (increase in magnitude) of a source because of its distance from the observer, making it a distance indicator. In order to directly compare the theoretical isochrones with the observed CMD, we need to shift them according to the values of  $\mu_0$  (vertical shift) and of the mean color excess (diagonal shift, along the direction of the reddening vector), in the following way:

$$m_{iso,\lambda} = M_{iso,\lambda} + \mu_0 + A_\lambda = M_{iso,\lambda} + \mu_0 + R_\lambda E(B - V)$$
(5.2)

where  $M_{iso,\lambda}$  is the absolute magnitude of the isochrone,  $\mu_0$  is the true distance modulus,  $A_{\lambda}$  is the total extinction in the considered band, and E(B-V) is the mean color excess. The observational data were previously corrected for differential reddening, as described in Chapter 4. Therefore, once the mean extinction and distance effects are

applied to the models, a consistent comparison in the CMD space will be possible.

To determine the best fit values for these parameters, we performed a preliminary isochrone fit analysis focused on the old, metal poor component, consistently identified as the dominant and oldest population in the system (Ferraro et al., 2009; Ferraro et al., 2016; Crociati et al., 2024). We adopted PARSEC (PAdova and TRieste Stellar Evolution Code) isochrone models (Bressan et al., 2012), downloaded from the online repertory, with metallicities  $[M/H] \in \{-0.35, -0.2\}$  and ages of 12, 12.5, and 13 Gyr. These values are consistent, within the uncertainties, with literature estimates for the oldest population. We determined the best-fit values by simultaneously fitting three CMD planes: (F606W-F814W, F814W), (F814W-F200W, F200W), and (F115W-F200W, F115W). Only stars identified as likely members and corrected for differential reddening were used. The model magnitudes were shifted according to Eq. 5.2, with  $R_{\lambda}$  computed from the O'Donnell (1994) extinction law assuming  $R_{V} = 2.5$  at the effective wavelengths of the HST and JWST filters employed.

This first step focuses on determining the global shifts, meaning  $\mu_0$  and E(B-V), by fitting the same isochrone across the three CMDs (optical, hybrid, NIR). Extinction produces coherent displacements whose direction and amplitude depend on  $R_{\lambda 1}$ ,  $R_{\lambda 2}$  for each filter pair; using three planes with very different passbands strongly constrains the  $(\mu_0, E(B-V))$  pair that aligns the model simultaneously in all the CMDs with special focus on the HB level for the distance modulus. This multi-CMD approach provides a robust determination of  $\mu_0$  and E(B-V), after which the age can be refined in the most age-sensitive region (the MS-TO) in the NIR plane, where we have the most accurate dataset.

The comparison metric used in this work for fitting is a bivariate  $\chi^2$  that accounts for color–magnitude covariances. For a CMD defined by bands  $m_1, m_2$  and variables  $(C, M) = (m_1 - m_2, m_1)$ , the adopted statistic is thus

$$\chi^{2} = \sum_{i} \min_{j} \left[ \left( \Delta C_{ij} \ \Delta M_{ij} \right) \begin{pmatrix} \sigma_{2,i}^{-2} & -\sigma_{2,i}^{-2} \\ -\sigma_{2,i}^{-2} & \frac{\sigma_{1,i}^{2} + \sigma_{2,i}^{2}}{\sigma_{1,i}^{2} \sigma_{2,i}^{2}} \end{pmatrix} \begin{pmatrix} \Delta C_{ij} \\ \Delta M_{ij} \end{pmatrix} \right], \tag{5.3}$$

where  $\Delta C_{ij}$  and  $\Delta M_{ij}$  are the color and magnitude differences between the *i*-th star and the *j*-th point along the isochrone, and  $\sigma_{1,i}^2, \sigma_{2,i}^2$  are the photometric error variances in  $m_1$  and  $m_2$  for that star. The central matrix is thus the inverse of the covariance matrix of the  $(m_1 - m_2, m_1)$  pair written as function of the magnitude errors. To account for additional sources of uncertainty that are not fully represented by the standard photometric errors, we adopt a minimum photometric uncertainty of 0.02 mag. This choice reflects the need to include both systematic contributions (such as the differential reddening correction) and to account for *DAOPHOT*'s tendency to

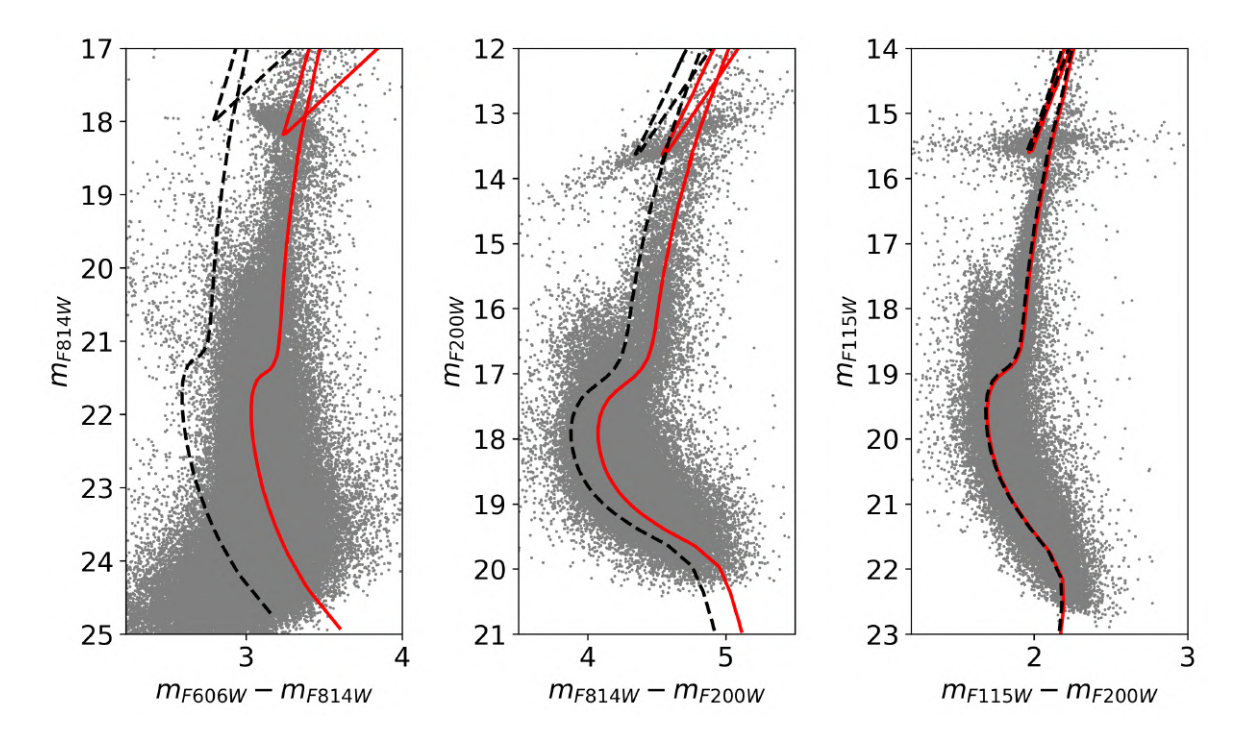


Figure 5.1: Optical (left), hybrid (center), and near-infrared (right) CMDs for propermotion—selected stars after applying the differential reddening correction. The red solid line is the 12.5 Gyr old isochrone with [M/H] = -0.35 (from Bressan et al., 2012) that best-fits the NIR CMD under the assumption of  $R_V = 2.5$ , and adopting  $\mu_0 = 14.15$ and E(B-V) = 2.92. As apparent, it properly reproduces also the optical and the hybrid CMDs. The black dashed line is the same isochrone reddened with  $R_V = 3.1$ , which requires  $\mu_0 = 14.15$  and E(B-V) = 2.1 to properly match the NIR plane, but clearly fails in reproducing the observations in the other color-magnitude combinations. The comparison clearly illustrates the inability of the  $R_V = 3.1$  law to reproduce all three CMDs simultaneously, confirming  $R_V = 2.5$  as the optimal extinction law in this case. This is very similar to what was found for Liller 1 by Pallanca et al. (2021), reinforcing the evidence for a non-standard extinction law in these heavily reddened bulge systems.

underestimate photometric errors.

The  $\chi^2$  is computed independently in the three CMDs and then summed to obtain a global statistic. For each matched ([M/H], age) pair we minimized this total  $\chi^2$  to estimate the parameters  $\mu_0$  and E(B-V) relevant to that isochrone. Among all matched pairs, we adopted as our final solution the one yielding the lowest global  $\chi^2$ . The resulting best–fit parameters are

$$\mu_0 = 14.15$$
 and  $E(B-V) = 2.92$ .

The corresponding distance is 6.76 kpc, in full agreement with the recent determination of Terzan 5's distance by Baumgardt and Vasiliev (2021) of  $d = 6.78 \pm 0.22$  kpc obtained with the latest Gaia DR3 data.

It is worth noticing that, although the adopted E(B-V) differs from the value of 2.38 commonly used literature (where  $R_V=3.1$  is assumed), here we rely on a different and more appropriate extinction law. In fact, not a single value of E(B-V) is able to simultaneously reproduce the optical, hybrid, and NIR CMDs if the standard coefficient  $R_V=3.1$  is assumed (see the black dashed lines in Figure 5.1). Conversely,  $R_V=2.5$  provides a consistent alignment of the isochrones with the observed data in all the planes for E(B-V)=2.92 (red lines in the figure). Indeed, when using three different CMDs with distinct coefficients  $R_{\lambda 1}$ ,  $R_{\lambda 2}$ , the solution becomes highly sensitive to the adopted extinction law, and the simultaneous comparison between observations and isochrones allows the determination of the most appropriate value of  $R_V$ . Figure 5.1 clearly confirms  $R_V=2.5$  as the most appropriate choice for Terzan 5, in agreement with results obtained for other heavily reddened systems in the bulge (see, for example, the case of Liller 1 in Pallanca et al., 2021).

### 5.2 Age determination with the MS-TO

Once these parameters were fixed, the detailed age analysis could be performed. The best-fit procedure was carried out by selecting stars within a radial interval between 10" and 50" from the cluster center. This choice minimizes the effects of crowding, which are particularly severe in the innermost regions ( $\leq 10$ "), and at the same time reduces the contamination from field stars, which becomes significant beyond 50".

Within this radial range, both stellar populations of Terzan 5 are well sampled, thus providing a dataset that is sufficiently numerous and representative for the comparison with theoretical isochrones. To separate the two populations, we selected stars located between the MS-TO and the SGB, adopting the *DAOPHOT* photometry, which is more reliable at these magnitudes (see Fig. 5.2).

The same statistics described in the previous section was then applied to determine

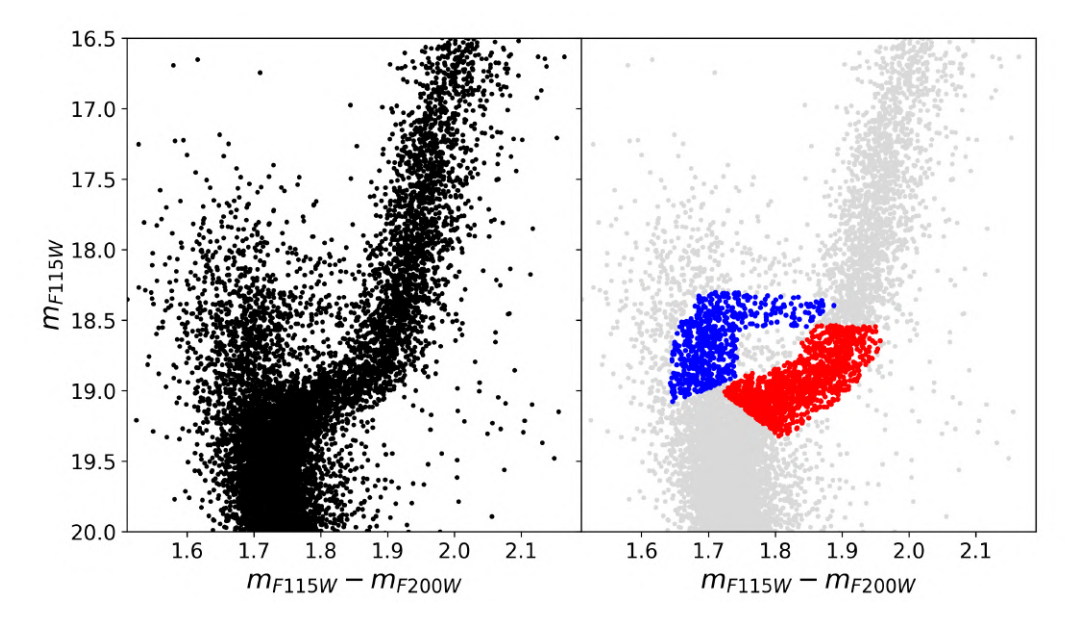


Figure 5.2: Proper-motion selected and differential-reddening corrected CMD zoomed in the MS-TO region. Left: all high-confidence stars located within an annulus of 10–50 arcsec from the system center (black circles). Right: the same stars (grey circles), with those used for the isochrone fitting highlighted in blue and red colors.

the best-fit models, this time keeping E(B-V) and  $\mu_0$  fixed, and leaving the age as the only free parameter. Models with metallicities  $[\mathrm{M/H}] \approx -0.35$  and  $[\mathrm{M/H}] \approx 0.3$  were adopted for the older and younger populations, respectively. Isochrones spanning a range of ages in steps of 0.1 Gyr were tested, as shown in Fig. 5.3. Darker colors correspond to lower  $\chi^2_{\nu}$  values, while lighter shades mark progressively less probable solutions, with the reduced  $\chi^2$  being defined as:

$$\chi_{\nu}^2 = \frac{\chi^2}{\nu},\tag{5.4}$$

where  $\nu$  is the number of degrees of freedom, here equal to N-1, with N being the number of stars used in the fit and one free parameter (the age). The resulting age vs  $\chi^2_{\nu}$  distributions are shown in Fig. 5.4 with their parabolic fits used to locate the minima, which identify the best-fit ages of the two populations:  $12.7 \pm 0.5$  Gyr for the oldest component,  $4.6 \pm 0.5$  Gyr for the younger one. The quoted uncertainties conservatively take into account the statistical error of the parabolic fit, together with systematics mainly due to intrinsic uncertainties in stellar models and degeneracies involving the adopted E(B-V) and metallicity. Figure 5.5 shows the best-fit isochrones for both populations, with a zoom on the TO regions where the fitting procedure was performed. The adopted solutions reproduce well the observed morphology of both TO and SGB, supporting the reliability of the derived ages.

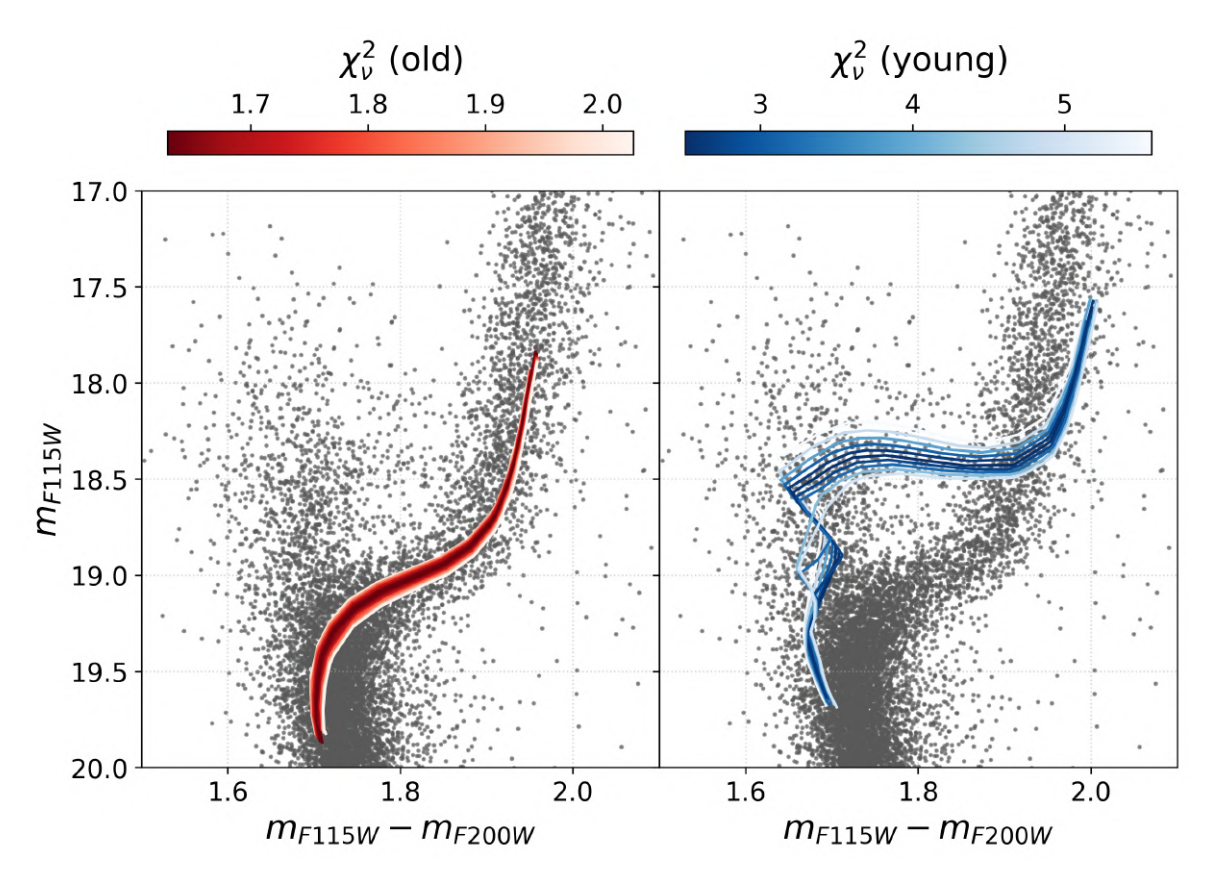


Figure 5.3: JWST CMD with the PARSEC isochrones (Bressan et al., 2012) used in the fitting procedure overplotted, for the oldest and metal-poor component (left panel), and for the younger and metal-rich one (right panel). For clarity, only the models lying closest to the final solution providing the most likely representation of the data, are displayed. These correspond to an age range between 12 and 13.5 Gyr in steps of 0.1 Gyr for the older sub-population, and between 4 and 5 Gyr for the younger component. The isochrones are color-coded according to the corresponding  $\chi^2_{\nu}$  value, with darker shades for lower values (see the colorbars), highlighting more likely models.

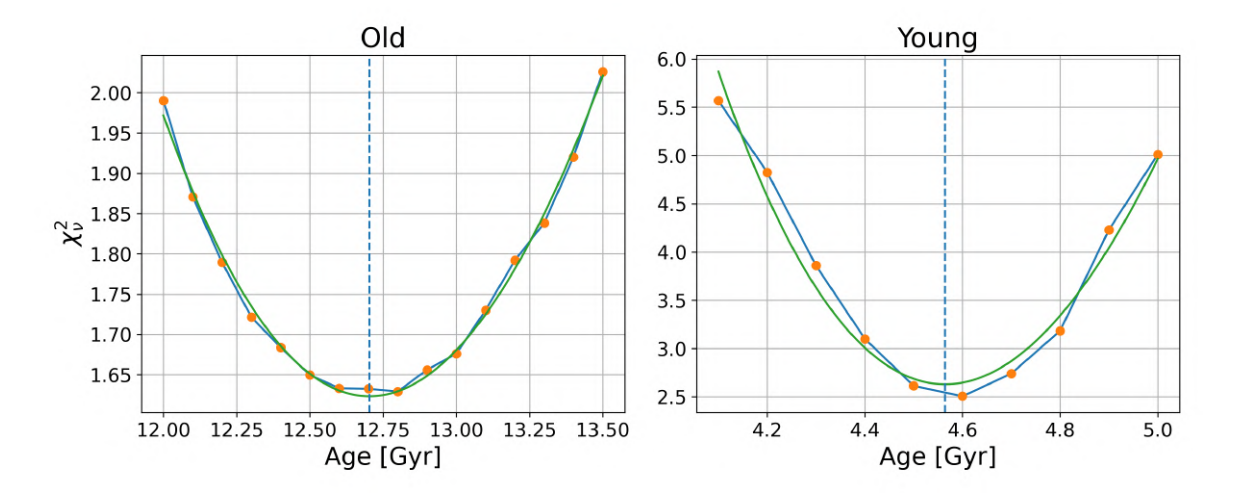


Figure 5.4:  $\chi^2_{\nu}$  as a function of age for the older (left) and younger (right) populations. The orange circles and their connecting blue lines mark the values of  $\chi^2_{\nu}$  obtained for each 0.1 Gyr-stepped age, the green line is the best-fit parabola, and the dashed vertical line highlights the corresponding best-fit age (the function's minimum).

To further test the robustness of the results, Fig. 5.6 presents the same best-fit isochrones overplotted on the full CMD, obtained without radial restrictions and combining the bright (jwst1pass) and faint (DAOPHOT) datasets. The agreement remains very good also along the brighter evolutionary sequences, from the RGB up to the HB, strengthening the validity of the adopted solutions.

One of the most intriguing characteristics of the new JWST CMD is the evidence of a large number of stars in the MS region drawing a sort of blue plume brighter than the 4.6 Gyr young population (see the points brighter than the blue line in Figs. 5.5 and 5.6). This could be the clue of a prolonged, recent star formation. Indeed, the careful inspection of the CMD zoomed in the MS-TO region allowed us to identify an intriguing alignment of stars in this region of the CMD that we used to give an estimate of the age of this additional component. We selected the stars aligned above the second MS-TO and adopted the same  $\chi^2$  statistics discussed above to estimate the age of this component, finding  $\approx 3.8$  Gyr. Figure 5.7 shows the corresponding isochrone as a green line, while the  $\chi^2_{\nu}$  distribution is plotted in Figure 5.8. Intriguingly, this age value is compatible with the preliminary SFH study by Crociati et al. (2024), who found indications of an extended period of star formation.

To further investigate the nature of these stellar populations, we selected three corresponding samples in the MS-TO region of the CMD as shown in the left panel of Fig. 5.9 and analyzed their radial distributions. As shown in the right panel of the same figure, the cumulative radial profiles reveal a clear trend: the younger the population, the more centrally concentrated it appears. In particular, the stars belonging to the newly identified  $\sim 3.8$  Gyr old component (marked in green) are the most centrally

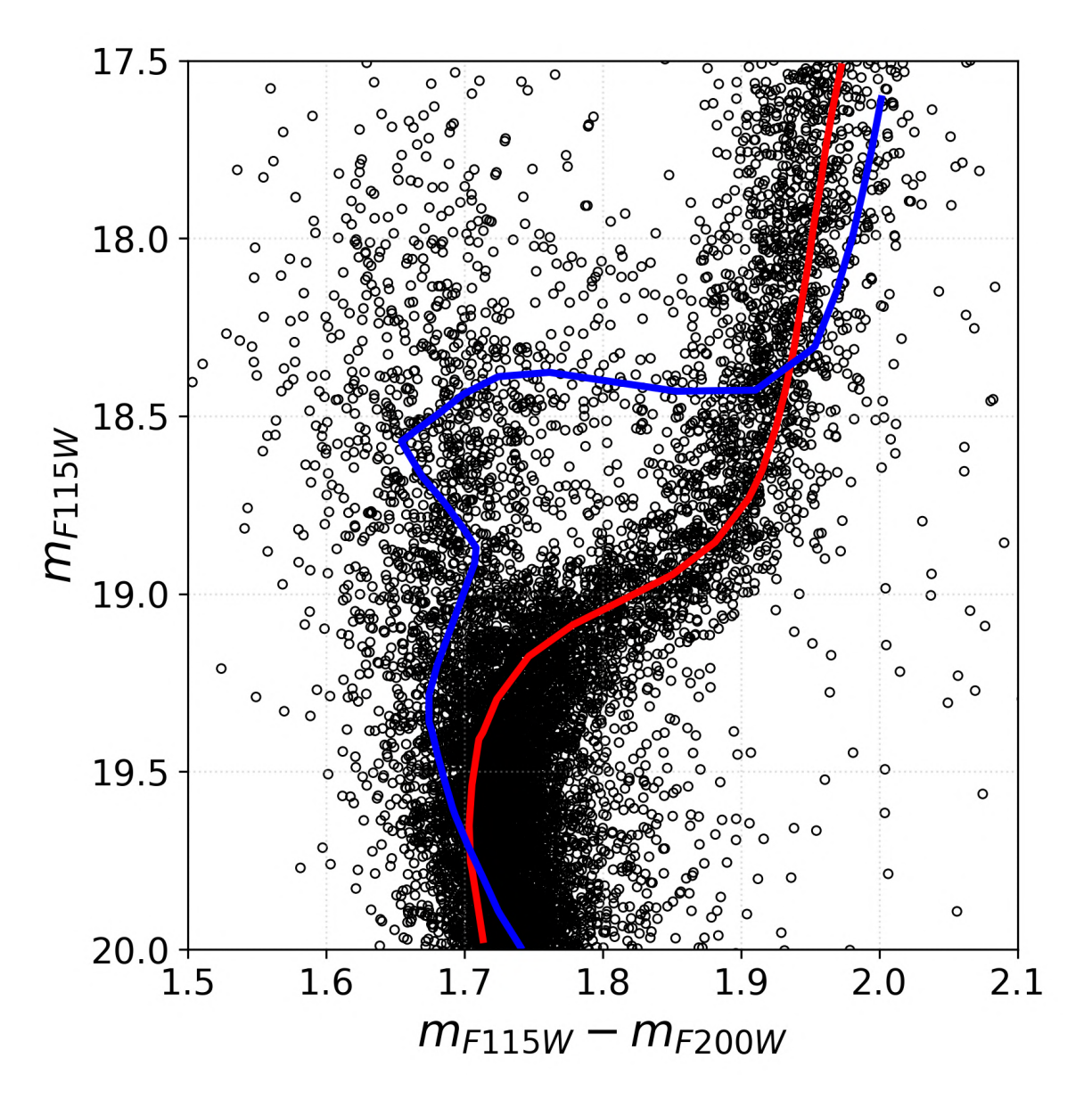


Figure 5.5:  $(m_{F115W} - m_{F200W}, m_{F115W})$  CMD derived from the *DAOPHOT* catalogue, proper-motion selected, differential reddening corrected, restricted to an annular region between 10" and 50", with quality cuts adopted to select only reliable stars, and zoomed in the MS-TO region. The best-fit isochrone of the older population, with an age of 12.7 Gyr, is represented by the red solid line. That of the younger population, with an age of 4.6 Gyr, is marked with the blue line.

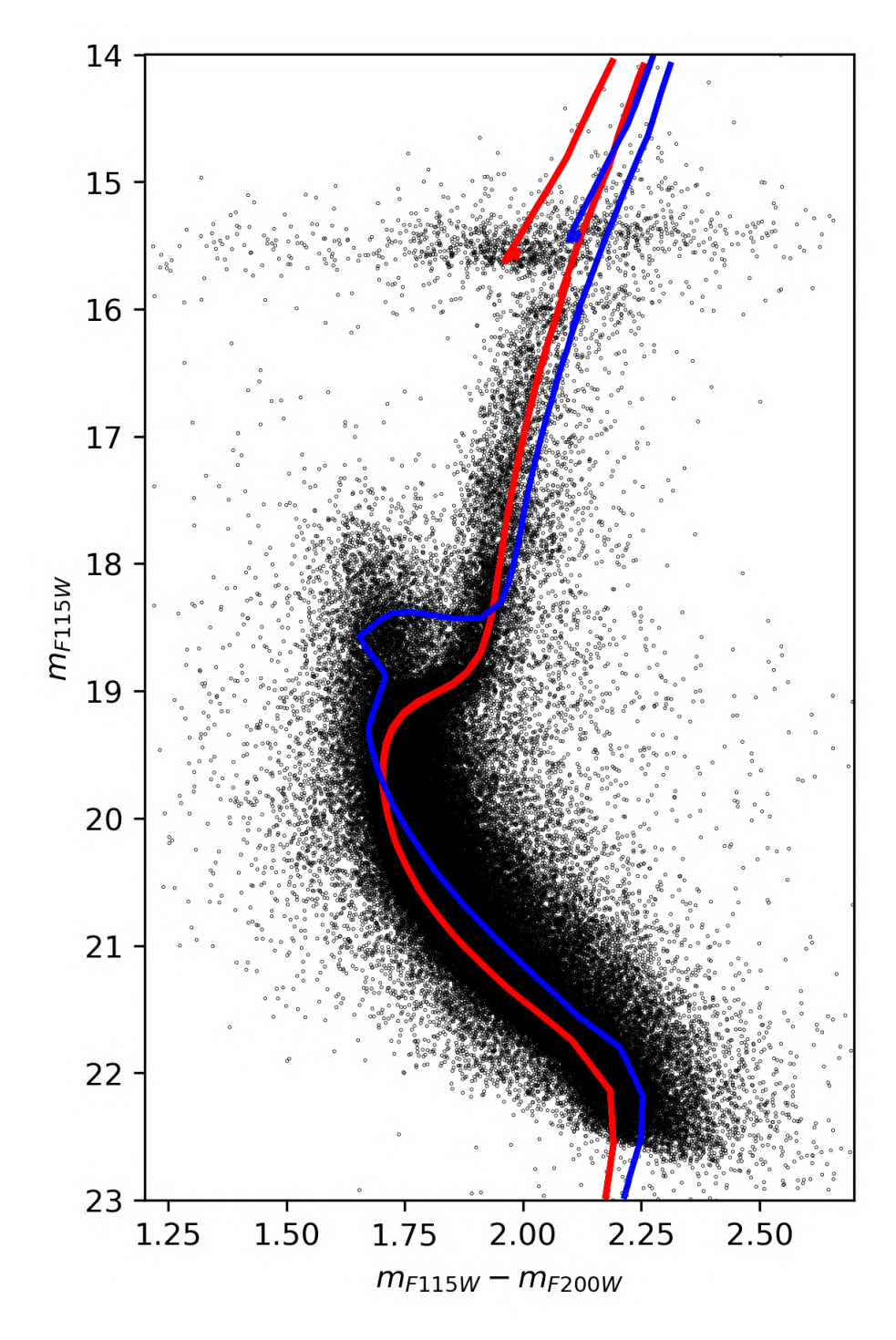


Figure 5.6: Differential-reddening corrected and proper motion selected CMD of Terzan 5. The black circles mark the selected stellar sample, combining bright (jwst1pass) and faint (DAOPHOT) photometry, over the entire  $\approx 3.5 \times 10^4 \, \rm arcsec^2$  FOV of the NIRCam B module. The PARSEC isochrones with ages of 12.7 Gyr (red line) and 4.6 Gyr (blue line) best-fitting the MS-TO region show a good agreement also with the observed sequences along the HB, RGB, and lower MS.

segregated, followed by those belonging to the  $\sim 4.6$  Gyr population (in blue), and then by the oldest,  $\sim 12.7$  Gyr old, population (in red). In turn, all the three components are more segregated toward the center of Terzan 5 than Galactic field stars (marked in black), as expected for populations that do belong to the system. This behavior is fully consistent with a self-enrichment scenario, where subsequent generations of stars form in the system's central regions from gas retained and processed by previous generations.

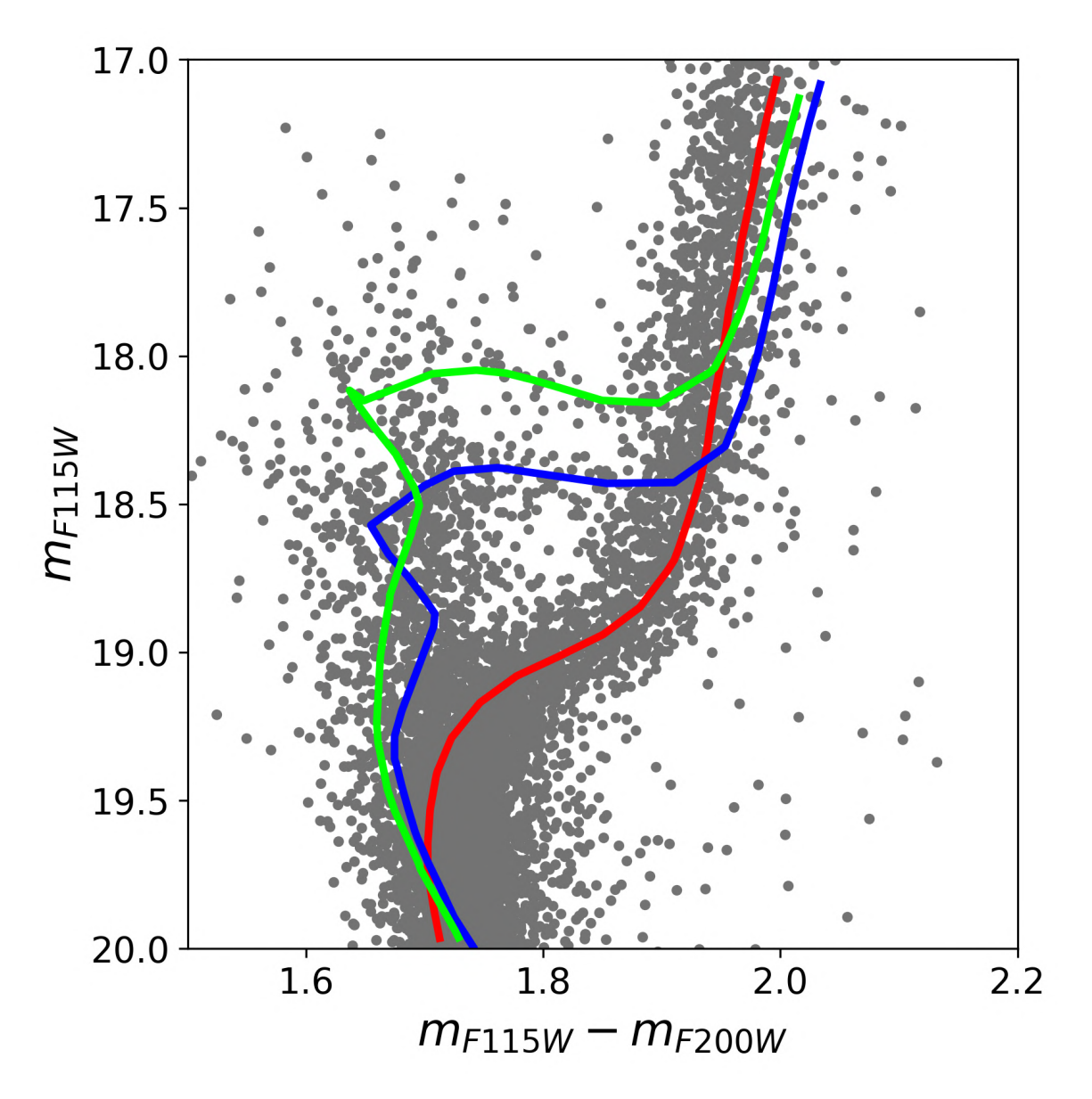


Figure 5.7: Same as in Fig. 5.5 but with an additional isochrone of 3.8 Gyr (green line) best- fitting the stars located above the 4.6 Gyr old MS-TO (blue line), possibly identifying an even younger population.

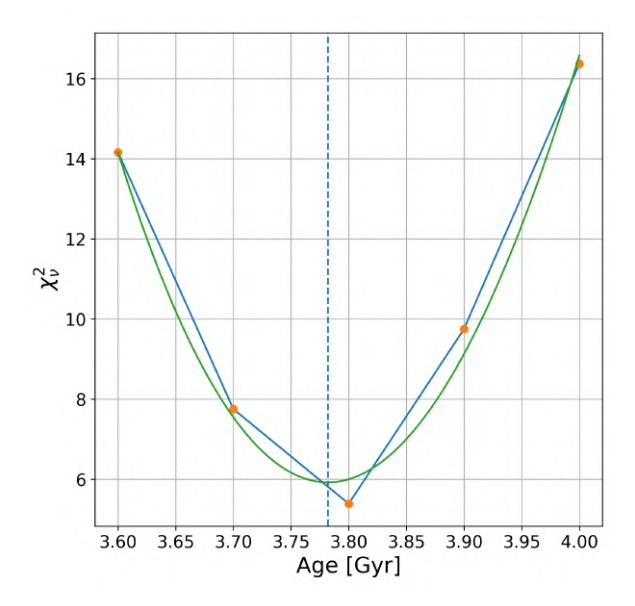


Figure 5.8:  $\chi^2_{\nu}$  as a function of age for the youngest isochrones (orange dots connected by blue lines) with the superimposed the parabolic fit (green line).

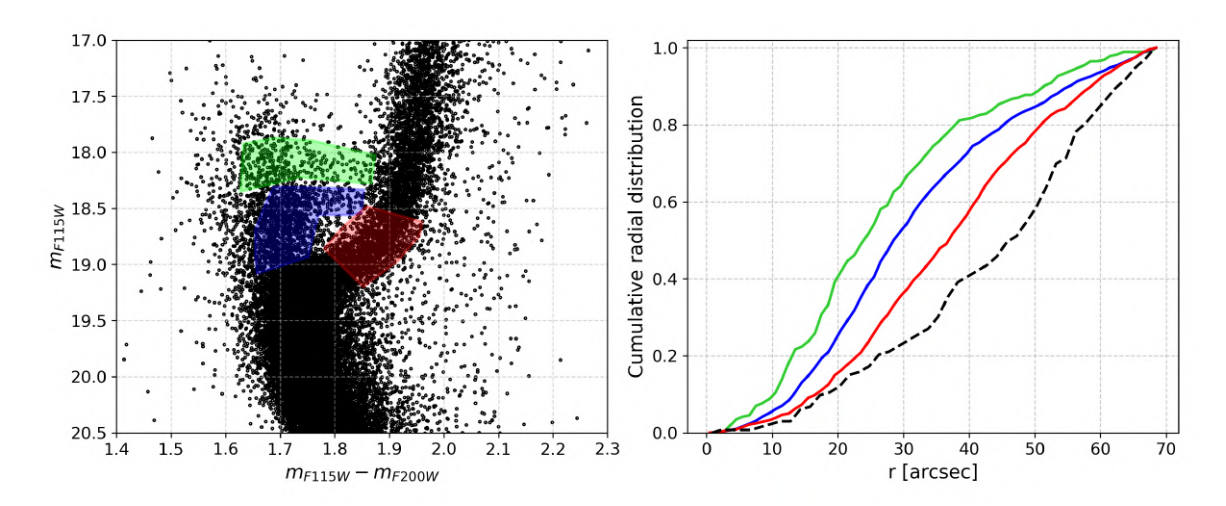


Figure 5.9: Left panel: JWST CMD zoomed in the MS-TO region with the selection boxes adopted to extract the three population sub-samples highlighted in colors: red, blue, and green colors for the components with and age of 12.7, 4.6 and 3.8 Gyr, respectively. Right panel: cumulative radial distributions of the three selected components (solid lines with the same color-code as in the left panel), and of a sample of Galactic field stars (black dashed line).

# Chapter 6

### Conclusions

This thesis is part of a broader effort devoted to the study of stellar systems in the Galactic bulge, with the aim of constraining the formation and early evolutionary history of the central region of our galaxy. Among these systems, Terzan 5 plays a crucial role because its photometric, chemical and kinematic properties (Ferraro et al., 2009; Ferraro et al., 2016; Massari et al., 2014; Origlia et al., 2011, 2025) make it a prime candidate to be the surviving relic of a primordial bulge building block. In this framework, accurately determining the ages of its populations is crucial to constrain its evolutionary history and and clarify its connection with the formation mechanisms of the Milky Way bulge.

This thesis has presented a detailed photometric investigation of Terzan 5, with the main goal of accurately determining the ages of its stellar sub-populations. The novelty of this work relies in the use of new proprietary JWST NIRCam observations of Terzan 5 in the F115W and F200W filters that, combined with archival optical HST ACS datasets in F606W and F814W, provided the deepest CMD ever obtained for the system.

A customized version of the JWST calibration pipeline was used to optimize the treatment of very bright and crowded images, improving the quality and statistics of the final catalogue. The photometric reduction combined DAOPHOT and jwst1pass PSF fitting to exploit the complementary strengths of the two approaches: while DAOPHOT excels in recovering faint stars in the most crowded regions, jwst1pass enabled the treatment of bright sources, even those with saturated cores. This strategy allowed us to construct a CMD that is  $\sim 4$  magnitudes deeper than any previously available one, without loss of information on the bright HB and RGB stars.

A crucial step was the selection of high-confidence member stars to clean the CMD from field contamination. This was achieved through proper motion measurements made available by the 20-year temporal baseline granted by the combination of JWST and HST observations. To reveal the intrinsic shape of the evolutionary sequences

it was crucial to also correct for differential reddening effects. To this scope, high resolution reddening maps were built, showing variations in E(B-V) up to  $\sim 0.8$  magnitudes.

Once the intrinsic CMD morphology was recovered using this finely selected catalogue, the isochrone fitting procedure was performed. By applying a simultaneous fitting of the optical, near-infrared and hybrid CMDs, we constrained the distance modulus and average color excess, finding  $\mu_0 = 14.15$  (which corresponds to a distance of 6.8 kpc, in full agreement with the estimate of Baumgardt and Vasiliev 2021), and E(B-V) = 2.92. These values have been obtained under the assumption of an extinction law with  $R_V = 2.5$ , which proved to be the most appropriate choice to simultaneously fit the CMDs in all the available color-magnitude combinations. This reinforced previous findings (Pallanca et al., 2021) suggesting the need of a non-standard description of extinction in the direction of the Galactic bulge.

Isochrone fitting of high-quality member stars in the MS-TO region revealed the presence of two main populations:

- A dominant, sub-solar metallicity component aged  $12.7 \pm 0.5$  Gyr
- A younger, super-solar metallicity component aged  $4.6 \pm 0.5$  Gyr.

Moreover, we find hints of an even younger population (of  $\sim 3.8$  Gyr) traced by stars drawing a blue plume brighter than the 4.6 Gyr old MS-TO, and suggesting an extended period of star formation. Very interestingly, the radial distribution of the three sub-populations is fully consistent with a self-enrichment scenario, with higher central concentrations for the more recent generations of stars (see Fig 5.9). These findings are in good agreement with the reconstruction of the SFH of Terzan5 independently obtained by Crociati et al. (2024), which suggests prolonged multiple SF bursts over time (see Fig. 1.10)

The results obtained in this thesis thus consolidate the view of Terzan 5 as a Bulge Fossil Fragment. In fact, the coexistence of different populations with distinct ages, added to the observed metallicity spread and abundance patterns, rule out the possibility that it is a genuine globular cluster, but are consistent with the scenario where Terzan 5 was a massive clump capable of retaining SN iron ejecta. In this self-enrichment scenario, the younger 4.6 Gyr population is likely a product of a later star formation episode possibly triggered by the interaction with other bulge sub-structures.

Looking forward, more detailed studies are required to accurately characterize the properties of the discovered sub-populations. The first step is to improve the analysis of their radial distribution by carefully evaluating the photometric completeness of the selected samples and the possible contamination from blends in these crowded regions. Moreover, future high-resolution surveys of Terzan 5 stars are needed to obtain

additional information on its chemical enrichment history. In particular, it is now urged to investigate the chemical composition of the stars belonging to the candidate 3.8 Gyr old population, to solidly confirm its existence. This requires the spectroscopic screening of a large number of giant stars, aimed at intercepting this population among the objects belonging to the other two (more numerous) components. Alternatively, the advent of high angular resolution spectrographs with high-enough spectral resolution installed at the incoming 40m-class telescopes (for instance, HARMONI at the ESO-ELT) will finally enable the measurement of chemical abundances directly in the MS-TO region of this highly-extincted system.

In addition, the unprecedented depth of the new JWST catalogue produced in this work will allow, for the first time, investigations of the stellar mass function down to  $\sim 0.2 M_{\odot}$ . Such a photometric quality for faint sources opens to the possibility of determining the mass function and tracing the radial distribution of stars down to unprecedentedly small limits, for each sub-population.

A key complementary line of research involves Liller 1, another massive system found in the bulge sharing several features with Terzan 5 and identifying it as another example of Bulge Fossil Fragment (Ferraro et al., 2021). Future JWST NIRCam observations of Liller 1, and possibly other bulge systems, will provide CMDs of comparable depth and quality to those obtained in this work, allowing for unprecedented explorations of their stellar population content and direct comparisons among the obtained results. The combined study of these two Bulge Fossil Fragments and any newly discovered candidate will be crucial to assess common properties and differences among these relics. In addition, recent JWST observations of high-redshift (up to  $z \sim 10$ ) gravitationally-lensed galaxies are revealing that the high-z Universe is substantially clumpy (e.g., Messa et al. (2024); Adamo et al. (2024)). The comparison between the observed properties of high-z clumps and local Bulge Fossil Fragments promises to open a completely new perspective on galaxy formation, finally clarifying the assembly processes of galactic bulges and, maybe, of their central super-massive black holes, as well.

# **Bibliography**

- ACS Instrument Handbook. HST User Documentation. https://hst-docs.stsci.edu/acsdhb/chapter-4-acs-data-processing-considerations/4-1-read-noise-and-a-to-d-conversion, 2024. Accessed: 2025-05-12.
- Angela Adamo, Larry D. Bradley, Eros Vanzella, Adélaïde Claeyssens, Brian Welch, Jose M. Diego, Guillaume Mahler, Masamune Oguri, Keren Sharon, Abdurro'uf, Tiger Yu-Yang Hsiao, Xinfeng Xu, Matteo Messa, Augusto E. Lassen, Erik Zackrisson, Gabriel Brammer, Dan Coe, Vasily Kokorev, Massimo Ricotti, Adi Zitrin, Seiji Fujimoto, Akio K. Inoue, Tom Resseguier, Jane R. Rigby, Yolanda Jiménez-Teja, Rogier A. Windhorst, Takuya Hashimoto, and Yoichi Tamura. Bound star clusters observed in a lensed galaxy 460 Myr after the Big Bang., 632(8025):513–516, August 2024. doi: 10.1038/s41586-024-07703-7.
- Peter Bankhead, Robert Haase, and Kota Miura. Spatial formation of the image, 2023. URL https://bioimagebook.github.io/chapters/3-fluorescence/2-formation\_spatial/formation\_spatial.html. Accessed: 2025-08-03.
- H. Baumgardt and E. Vasiliev. Accurate distances to Galactic globular clusters through a combination of Gaia EDR3, HST, and literature data., 505(4):5957–5977, August 2021. doi: 10.1093/mnras/stab1474.
- H. Baumgardt, P. Kroupa, and G. Parmentier. The influence of residual gas expulsion on the evolution of the Galactic globular cluster system and the origin of the Population II halo., 384(3):1231–1241, March 2008. doi: 10.1111/j.1365-2966.2007.12811.x.
- H. Baumgardt, M. Hilker, A. Sollima, and A. Bellini. Mean proper motions, space orbits, and velocity dispersion profiles of Galactic globular clusters derived from Gaia DR2 data., 482(4):5138–5155, February 2019. doi: 10.1093/mnras/sty2997.
- Edouard J Bernard, Mathias Schultheis, Paola Di Matteo, Vanessa Hill, Misha Haywood, and Annalisa Calamida. Star formation history of the galactic bulge from deep hst imaging of low reddening windows. *Monthly Notices of the Royal Astronomical Society*, 477(3):3507–3519, April 2018. ISSN 1365-2966. doi: 10.1093/mnras/sty902. URL http://dx.doi.org/10.1093/mnras/sty902.

- R. C. Bohlin. Encircled energy fractions for hot stars at wfc1-1k. https://www.stsci.edu/files/live/sites/www/files/home/hst/instrumentation/acs/data-analysis/aperture-corrections/\_documents/bohlin2016\_wfc\_ee-1.txt, 2016. Accessed: 2025-05-25.
- Frédéric Bournaud. Bulge Growth Through Disc Instabilities in High-Redshift Galaxies. In Eija Laurikainen, Reynier Peletier, and Dimitri Gadotti, editors, *Galactic Bulges*, volume 418 of *Astrophysics and Space Science Library*, page 355, January 2016. doi: 10.1007/978-3-319-19378-6 13.
- Frédéric Bournaud and Bruce G. Elmegreen. Unstable Disks at High Redshift: Evidence for Smooth Accretion in Galaxy Formation., 694(2):L158–L161, April 2009. doi: 10.1088/0004-637X/694/2/L158.
- Alessandro Bressan, Paola Marigo, Léo Girardi, Bernardo Salasnich, Claudia Dal Cero, Stefano Rubele, and Ambra Nanni. PARSEC: stellar tracks and isochrones with the PAdova and TRieste Stellar Evolution Code. *Monthly Notices of the Royal Astronomical Society*, 427(1):127–145, November 2012. doi: 10.1111/j.1365-2966. 2012.21948.x.
- Howard Bushouse, Jonathan Eisenhamer, Nadia Dencheva, James Davies, Perry Greenfield, Jane Morrison, Phil Hodge, Bernie Simon, David Grumm, Michael Droettboom, Edward Slavich, Megan Sosey, Tyler Pauly, Todd Miller, Robert Jedrzejewski, Warren Hack, David Davis, Steven Crawford, David Law, Karl Gordon, Michael Regan, Mihai Cara, Ken MacDonald, Larry Bradley, Clare Shanahan, William Jamieson, Mairan Teodoro, Thomas Williams, Maria Pena-Guerrero, Brett Graham, Edward Molter, Timothy Brandt, Christian Hayes, Rachel Cooper, Melanie Clarke, and Joseph Filippazzo. Jwst calibration pipeline, June 2025. URL https://doi.org/10.5281/zenodo.15632984.
- Jason A. Cardelli, Geoffrey C. Clayton, and John S. Mathis. The Relationship between Infrared, Optical, and Ultraviolet Extinction., 345:245, October 1989. doi: 10.1086/ 167900.
- Daniel Ceverino, Avishai Dekel, and Frederic Bournaud. High-redshift clumpy discs and bulges in cosmological simulations. , 404(4):2151–2169, June 2010. doi: 10. 1111/j.1365-2966.2010.16433.x.
- W. I. Clarkson, Kailash C. Sahu, Jay Anderson, R. Michael Rich, T. Ed. Smith, Thomas M. Brown, Howard E. Bond, Mario Livio, Dante Minniti, Alvio Renzini, and Manuela Zoccali. The first detection of blue straggler stars in the milky way bulge.

- The Astrophysical Journal, 735(1):37, June 2011. ISSN 1538-4357. doi: 10.1088/0004-637x/735/1/37. URL http://dx.doi.org/10.1088/0004-637X/735/1/37.
- Will Clarkson, Kailash Sahu, Jay Anderson, T. Ed Smith, Thomas M. Brown, R. Michael Rich, Stefano Casertano, Howard E. Bond, Mario Livio, Dante Minniti, Nino Panagia, Alvio Renzini, Jeff Valenti, and Manuela Zoccali. Stellar Proper Motions in the Galactic Bulge from Deep Hubble Space Telescope ACS WFC Photometry., 684(2):1110–1142, September 2008. doi: 10.1086/590378.
- C. Crociati, M. Cignoni, E. Dalessandro, C. Pallanca, D. Massari, F. R. Ferraro, B. Lanzoni, L. Origlia, and E. Valenti. The star formation history of the first bulge fossil fragment candidate Terzan 5. , 691:A311, November 2024. doi: 10.1051/0004-6361/202451174.
- Emanuele Dalessandro, Chiara Crociati, Michele Cignoni, Francesco R. Ferraro, Barbara Lanzoni, Livia Origlia, Cristina Pallanca, R. Michael Rich, Sara Saracino, and Elena Valenti. Clues to the Formation of Liller 1 from Modeling Its Complex Star Formation History., 940(2):170, December 2022. doi: 10.3847/1538-4357/ac9907.
- O. J. Eggen, D. Lynden-Bell, and A. R. Sandage. Evidence from the motions of old stars that the Galaxy collapsed., 136:748, November 1962. doi: 10.1086/147433.
- Bruce G. Elmegreen, Frédéric Bournaud, and Debra Meloy Elmegreen. Bulge Formation by the Coalescence of Giant Clumps in Primordial Disk Galaxies. , 688(1): 67–77, November 2008. doi: 10.1086/592190.
- Debra Meloy Elmegreen, Bruce G. Elmegreen, Max T. Marcus, Karlen Shahinyan, Andrew Yau, and Michael Petersen. Clumpy galaxies in goods and gems: Massive analogs of local dwarf irregulars. *The Astrophysical Journal*, 701(1):306–329, July 2009. ISSN 1538-4357. doi: 10.1088/0004-637x/701/1/306. URL http://dx.doi.org/10.1088/0004-637X/701/1/306.
- C. Fanelli, L. Origlia, R. M. Rich, F. R. Ferraro, D. A. Alvarez Garay, L. Chiappino, B. Lanzoni, C. Pallanca, C. Crociati, and E. Dalessandro. Multi-iron subpopulations in Liller 1 from high-resolution H-band spectroscopy., 690:A139, October 2024. doi: 10.1051/0004-6361/202451030.
- F. R. Ferraro, E. Dalessandro, A. Mucciarelli, G. Beccari, R. M. Rich, L. Origlia, B. Lanzoni, R. T. Rood, E. Valenti, M. Bellazzini, S. M. Ransom, and G. Cocozza. The cluster Terzan 5 as a remnant of a primordial building block of the Galactic bulge. , 462(7272):483–486, November 2009. doi: 10.1038/nature08581.

- F. R. Ferraro, D. Massari, E. Dalessandro, B. Lanzoni, L. Origlia, R. M. Rich, and A. Mucciarelli. The age of the young bulge-like population in the stellar system terzan 5: Linking the galactic bulge to the high-z universe\*. The Astrophysical Journal, 828 (2):75, September 2016. ISSN 1538-4357. doi: 10.3847/0004-637x/828/2/75. URL http://dx.doi.org/10.3847/0004-637X/828/2/75.
- F. R. Ferraro, C. Pallanca, B. Lanzoni, C. Crociati, E. Dalessandro, L. Origlia, R. M. Rich, S. Saracino, A. Mucciarelli, E. Valenti, D. Geisler, F. Mauro, S. Villanova, C. Moni Bidin, and G. Beccari. A new class of fossil fragments from the hierarchical assembly of the Galactic bulge. *Nature Astronomy*, 5:311–318, January 2021. doi: 10.1038/s41550-020-01267-y.
- Gaia Collaboration, T. Prusti, J. H. J. de Bruijne, et al. The Gaia mission. *Astronomy & Astrophysics*, 595:A1, 2016. doi: 10.1051/0004-6361/201629272.
- Gaia Collaboration, A. Vallenari, A. G. A. Brown, et al. Gaia Data Release 3: Summary of the content and survey properties. *Astronomy & Astrophysics*, 674:A1, 2023. doi: 10.1051/0004-6361/202244848.
- R. Genzel, S. Newman, T. Jones, N. M. Förster Schreiber, K. Shapiro, S. Genel, S. J. Lilly, A. Renzini, L. J. Tacconi, N. Bouché, A. Burkert, G. Cresci, P. Buschkamp, C. M. Carollo, D. Ceverino, R. Davies, A. Dekel, F. Eisenhauer, E. Hicks, J. Kurk, D. Lutz, C. Mancini, T. Naab, Y. Peng, A. Sternberg, D. Vergani, and G. Zamorani. The Sins Survey of z ~2 Galaxy Kinematics: Properties of the Giant Star-forming Clumps., 733(2):101, June 2011. doi: 10.1088/0004-637X/733/2/101.
- Raffaele Gratton, Christopher Sneden, and Eugenio Carretta. Abundance Variations Within Globular Clusters., 42(1):385–440, September 2004. doi: 10.1146/annurev. astro.42.053102.133945.
- Massimo Griggio, Daniele Nardiello, and Luigi R. Bedin. Photometry and astrometry with jwst ii. nircam distortion correction. *Astronomische Nachrichten*, 344(1-2): e202300006, 2023. doi: 10.1002/asna.20230006.
- A. Immeli, M. Samland, O. Gerhard, and P. Westera. Gas physics, disk fragmentation, and bulge formation in young galaxies., 413:547–561, January 2004. doi: 10.1051/0004-6361:20034282.
- JWST Science Calibration Pipeline Team. Encircled energy table for nircam sw (etc v2). https://jwst-docs.stsci.edu/files/154689003/154689005/1/1716395573461/Encircled\_Energy\_SW\_ETCv2.txt, 2024. Accessed: 2025-05-25.

- JWST User Documentation. https://jwst-docs.stsci.edu/#gsc.tab=0. Accessed: 2025-05-12.
- John Kormendy and Robert C. Kennicutt, Jr. Secular Evolution and the Formation of Pseudobulges in Disk Galaxies., 42(1):603–683, September 2004. doi: 10.1146/annurev.astro.42.053102.134024.
- B. Lanzoni, F. R. Ferraro, E. Dalessandro, A. Mucciarelli, G. Beccari, P. Miocchi, M. Bellazzini, R. M. Rich, L. Origlia, E. Valenti, R. T. Rood, and S. M. Ransom. New density profile and structural parameters of the complex stellar system terzan 5. The Astrophysical Journal, 717(2):653–657, June 2010. ISSN 1538-4357. doi: 10.1088/0004-637x/717/2/653. URL http://dx.doi.org/10.1088/0004-637X/717/2/653.
- Cheng Li, Shude Mao, and Simon D. M. White. Galaxy formation. In William H. Waller, editor, *NED Level 5 Knowledgebase*. NASA/IPAC Extragalactic Database, 2007. URL https://ned.ipac.caltech.edu/level5/Sept07/Li2/Li2.html. Accessed: 2025-08-01.
- Massimo Libralato, Antonino Bellini, Roeland P. van der Marel, Jay Anderson, S. T. Sohn, Lindsay L. Watkins, Michael Alderson, Nicola Allen, Mark Clampin, Andrew Glidden, Jayesh Goyal, Kyle Hoch, Jian Huang, Jelte Kammerer, Nolan K. Lewis, Zhen Lin, Deidre Long, Dustin Louie, Ryan J. MacDonald, Max Mountain, Miguel Ángel Peña-Guerrero, Marshall D. Perrin, Laurent Pueyo, Ignacio Rebollido, Estée Rickman, Sara Seager, Kevin B. Stevenson, John A. Valenti, Deborah Valentine, and Hannah R. Wakeford. Jwst-tst proper motions: I. high-precision niriss calibration and large magellanic cloud kinematics. *The Astrophysical Journal*, 2023. doi: 10.3847/XXXXX. Based on the online PDF hosted at STScI effective PSFs and geometric-distortion correction for JWST NIRISS.
- D. Massari, A. Mucciarelli, F. R. Ferraro, L. Origlia, R. M. Rich, B. Lanzoni, E. Dalessandro, E. Valenti, R. Ibata, L. Lovisi, M. Bellazzini, and D. Reitzel. Ceci n'est pas a globular cluster: The metallicity distribution of the stellar system terzan 5. The Astrophysical Journal, 795(1):22, October 2014. ISSN 1538-4357. doi: 10.1088/0004-637x/795/1/22. URL http://dx.doi.org/10.1088/0004-637X/795/1/22.
- Andrew McWilliam. The chemical composition of the galactic bulge and implications for its evolution. *Publications of the Astronomical Society of Australia*, 33:e040, 2016. doi: 10.1017/pasa.2016.32.
- Matteo Messa, Miroslava Dessauges-Zavadsky, Angela Adamo, Johan Richard, and Adélaïde Claeyssens. Properties of the brightest young stellar clumps in extremely

- lensed galaxies at redshifts 4 to 5. , 529(3):2162–2179, April 2024. doi: 10.1093/ mnras/stae565.
- P. Montegriffo, F. R. Ferraro, L. Origlia, and F. Fusi Pecci. Astrometry and photometry with the bologna observatory software cataxcorr. *Monthly Notices of the Royal Astronomical Society*, 276:739–748, 1995. doi: 10.1093/mnras/276.3.739.
- NASA. Hubble Space Telescope. https://science.nasa.gov/mission/hubble/, a. Accessed: 2025-05-12.
- NASA. Hubble vs Webb Hubble Space Telescope. https://science.nasa.gov/mission/hubble/observatory/hubble-vs-webb/, b. Accessed: 2025-05-12.
- NASA. James Webb Space Telescope. https://science.nasa.gov/mission/webb/, c. Accessed: 2025-05-12.
- NASA, JWST Near Infrared Camera . https://jwst-docs.stsci.edu/jwst-near-infrared-camera#gsc.tab=0. Accessed: 2025-05-12.
- NASA, NIRCam Detector Readout Patterns. https://jwst-docs.stsci.edu/jwst-near-infrared-camera/nircam-instrumentation/nircam-detector-overview/nircam-detector-readout-patterns#gsc.tab=0.
  Accessed: 2025-05-12.
- NASA/ESA. Hubble admires a youthful globular star cluster. https://science.nasa.gov/missions/hubble/hubble-admires-a-youthful-globular-star-cluster/, 2016. Accessed: 2025-08-04.
- David M. Nataf, Andrew Gould, Pierre Fouqué, Oscar A. Gonzalez, and Jennifer A. Johnson. Interstellar extinction curve variations toward the inner milky way: Anomalous reddening, extinction, and implications for the galactic bulge. *The Astrophysical Journal*, 769(2):88, 2013. doi: 10.1088/0004-637X/769/2/88. URL https://iopscience.iop.org/article/10.1088/0004-637X/769/2/88.
- James E. O'Donnell. R v-dependent Optical and Near-Ultraviolet Extinction. , 422: 158, February 1994. doi: 10.1086/173713.
- L. Origlia, R. M. Rich, F. R. Ferraro, B. Lanzoni, M. Bellazzini, E. Dalessandro, A. Mucciarelli, E. Valenti, and G. Beccari. Spectroscopy Unveils the Complex Nature of Terzan 5., 726(2):L20, January 2011. doi: 10.1088/2041-8205/726/2/L20.

- L. Origlia, D. Massari, R. M. Rich, A. Mucciarelli, F. R. Ferraro, E. Dalessandro, and B. Lanzoni. The Terzan 5 Puzzle: Discovery of a Third, Metal-poor Component., 779(1):L5, December 2013. doi: 10.1088/2041-8205/779/1/L5.
- L. Origlia, A. Mucciarelli, G. Fiorentino, F. R. Ferraro, E. Dalessandro, B. Lanzoni, R. M. Rich, D. Massari, R. Contreras Ramos, and N. Matsunaga. Variable Stars in Terzan 5: Additional Evidence of Multi-age and Multi-iron Stellar Populations., 871(1):114, January 2019. doi: 10.3847/1538-4357/aaf730.
- L. Origlia, F. R. Ferraro, C. Fanelli, B. Lanzoni, D. Massari, E. Dalessandro, and C. Pallanca. The manifest link between Terzan 5 and the Galactic bulge., 697:A19, May 2025. doi: 10.1051/0004-6361/202452110.
- P. V. Padmanabh, S. M. Ransom, P. C. C. Freire, A. Ridolfi, J. D. Taylor, C. Choza, C. J. Clark, F. Abbate, M. Bailes, E. D. Barr, S. Buchner, M. Burgay, M. E. DeCesar, W. Chen, A. Corongiu, D. J. Champion, A. Dutta, M. Geyer, J. W. T. Hessels, M. Kramer, A. Possenti, I. H. Stairs, B. W. Stappers, V. Venkatraman Krishnan, L. Vleeschower, and L. Zhang. Discovery and timing of ten new millisecond pulsars in the globular cluster terzan 5. Astronomy amp; Astrophysics, 686:A166, June 2024. ISSN 1432-0746. doi: 10.1051/0004-6361/202449303. URL http://dx.doi.org/10.1051/0004-6361/202449303.
- Cristina Pallanca, Francesco R. Ferraro, Barbara Lanzoni, Chiara Crociati, Sara Saracino, Emanuele Dalessandro, Livia Origlia, Michael R. Rich, Elena Valenti, Douglas Geisler, Francesco Mauro, Sandro Villanova, Christian Moni Bidin, and Giacomo Beccari. High-resolution Extinction Map in the Direction of the Strongly Obscured Bulge Fossil Fragment Liller 1., 917(2):92, August 2021. doi: 10.3847/1538-4357/ac0889.
- Scott M. Ransom, Jason W. T. Hessels, Ingrid H. Stairs, Paulo C. C. Freire, Fernando Camilo, Victoria M. Kaspi, and David L. Kaplan. Twenty-One Millisecond Pulsars in Terzan 5 Using the Green Bank Telescope. *Science*, 307(5711):892–896, February 2005. doi: 10.1126/science.1108632.
- Michael Regan. JWST Technical Report: Detection and flagging of showers and snow-balls in JWST. https://www.stsci.edu/files/live/sites/www/files/home/jwst/documentation/technical-documents/\_documents/JWST-STScI-008545.pdf, 2024.p. 8, Accessed: 2025-05-12.
- Maurizio Salaris and Santi Cassisi. Evolution of Stars and Stellar Populations. John Wiley & Sons, Chichester, UK, 2005. ISBN 978-0-470-09220-9.

- S. Saracino, E. Dalessandro, F. R. Ferraro, B. Lanzoni, D. Geisler, F. Mauro, S. Villanova, C. Moni Bidin, P. Miocchi, and D. Massari. GEMINI/GeMS Observations Unveil the Structure of the Heavily Obscured Globular Cluster Liller 1., 806(2):152, June 2015. doi: 10.1088/0004-637X/806/2/152.
- P. B. Stetson. DAOPHOT A Computer Program for Crowded-Field Stellar Photometry. *Publications of the Astronomical Society of the Pacific*, 99:191, 1987.
- Peter B. Stetson. DAOPHOT: Crowded-field Stellar Photometry Package. Astrophysics Source Code Library, record ascl:1104.011, April 2011.
- STScI. Acs zeropoints calculator. https://acszeropoints.stsci.edu/, 2024a. Accessed: 2025-05-25.
- STScI. Jwst/nircam zeropoints file (nrc\_zps\_1126pmap.txt). https://jwst-docs.stsci.edu/files/154689209/154689212/1/1716319320811/NRC\_ZPs\_1126pmap.txt, 2024b. Accessed: 2025-05-25.
- Eline Tolstoy, Vanessa Hill, and Monica Tosi. Star-Formation Histories, Abundances, and Kinematics of Dwarf Galaxies in the Local Group. , 47(1):371–425, September 2009. doi: 10.1146/annurev-astro-082708-101650.
- E. Valenti, F. R. Ferraro, and L. Origlia. Near-infrared properties of 12 globular clusters towards the inner bulge of the Galaxy., 402(3):1729–1739, March 2010. doi: 10.1111/j.1365-2966.2009.15991.x.
- E. Valenti, M. Zoccali, O. A. Gonzalez, D. Minniti, J. Alonso-García, E. Marchetti, M. Hempel, A. Renzini, and M. Rejkuba. Stellar density profile and mass of the Milky Way bulge from VVV data., 587:L6, March 2016. doi: 10.1051/0004-6361/201527500.